

IN-09  
190890  
75P

**NASA**  
**Technical**  
**Paper**  
**3334**

September 1993

# Wall Interference and Boundary Simulation in a Transonic Wind Tunnel With a Discretely Slotted Test Section

Jassim A. Al-Saadi

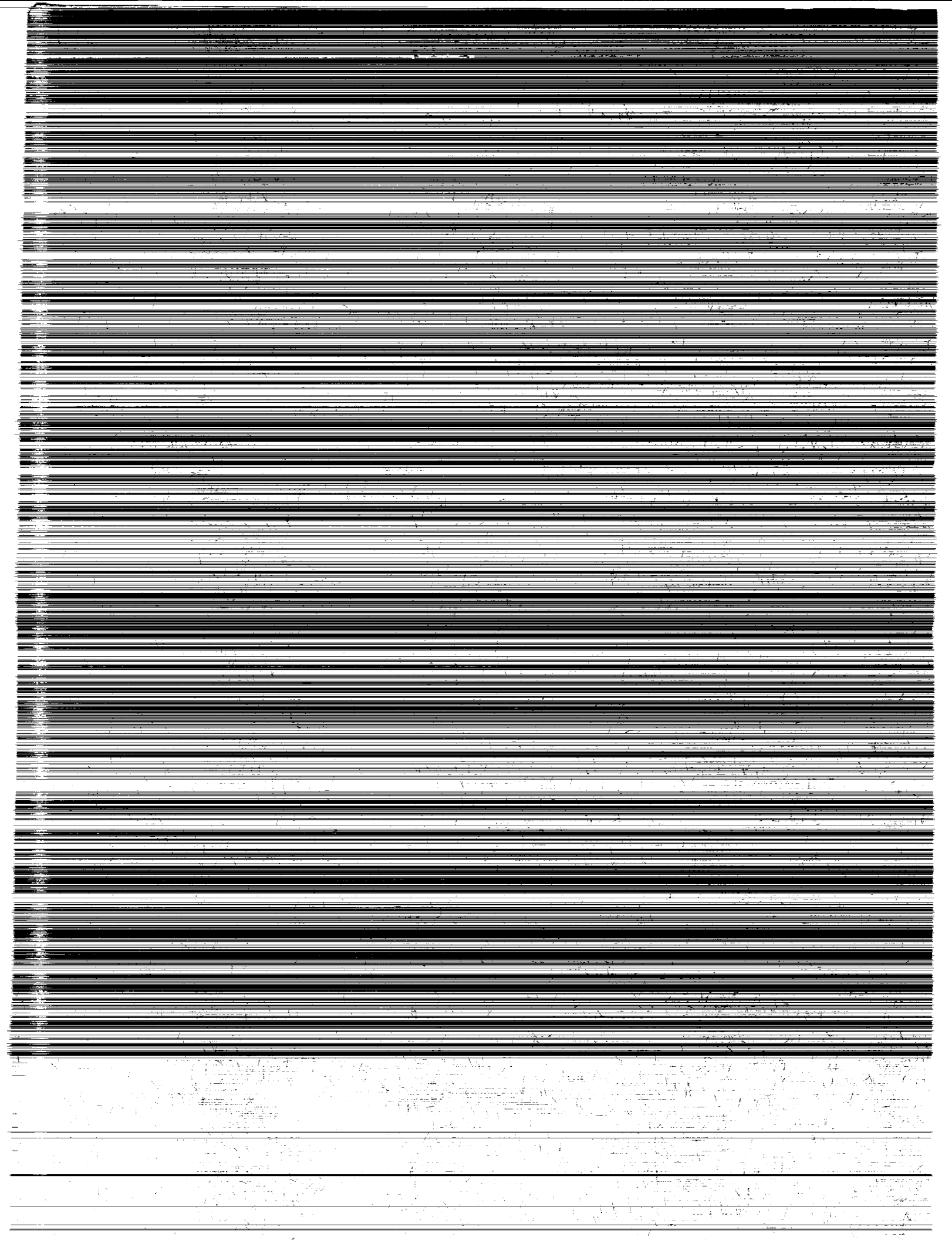
(NASA-TP-3334) WALL INTERFERENCE  
AND BOUNDARY SIMULATION IN A  
TRANSONIC WIND TUNNEL WITH A  
DISCRETELY SLOTTED TEST SECTION  
(NASA) 75 p

N94-15794

Unclass

H1/09 0190890

**NASA**



**NASA**  
**Technical**  
**Paper**  
**3334**

1993

Wall Interference and  
Boundary Simulation in  
a Transonic Wind Tunnel  
With a Discretely Slotted  
Test Section

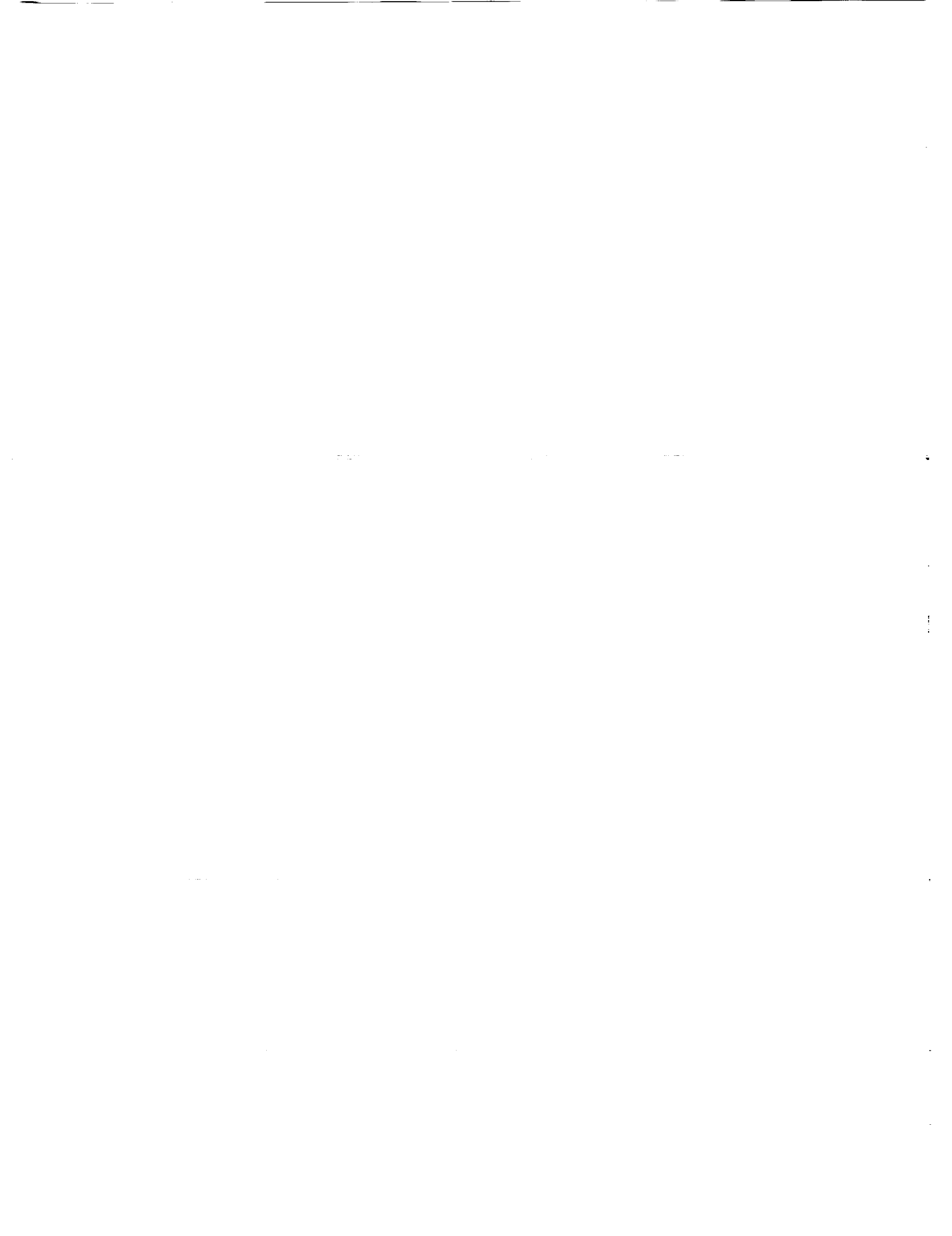
Jassim A. Al-Saadi  
*Langley Research Center*  
*Hampton, Virginia*

**NASA**

National Aeronautics and  
Space Administration

Office of Management

Scientific and Technical  
Information Program



## Abstract

*A computational simulation of a transonic wind tunnel test section with longitudinally slotted walls is developed and described herein. The nonlinear slot model includes dynamic pressure effects and a plenum pressure constraint, and each slot is treated individually. The solution is performed using a finite-difference method that solves an extended transonic small disturbance equation. The walls serve as the outer boundary conditions in the relaxation technique, and an interaction procedure is used at the slotted walls. Measured boundary pressures are not required to establish the wall conditions but are currently used to assess the accuracy of the simulation. This method can also calculate a free-air solution as well as solutions that employ the classical homogeneous wall conditions. The simulation is used to examine two commercial transport aircraft models at a supercritical Mach number for zero-lift and cruise conditions. Good agreement between measured and calculated wall pressures is obtained for the model geometries and flow conditions examined herein. Some localized disagreement is noted, which is attributed to improper simulation of viscous effects in the slots.*

## Introduction

The National Transonic Facility (NTF) at the Langley Research Center is designed to allow transonic wind tunnel testing of model configurations at full-scale Reynolds numbers (ref. 1). Because full-scale Reynolds numbers can now be matched in testing, new data correction techniques have been developed to further improve data quality. One correction addresses the interference that is induced by the test section walls. The ventilated test section has evolved in response to the requirements of transonic testing (ref. 2). A ventilated test section has walls that are either slotted or porous, and the entire test section is contained in a large, closed plenum chamber so that the tunnel can be pressurized. The NTF test section has six longitudinal slots in both the floor and ceiling that extend the full length of the test section and provide an open-area ratio of 6 percent of the wall area. The ventilated walls reduce but do not completely eliminate wall interference in a test section. At transonic speeds, the wall interference problem is complicated by the possible nonlinear interaction of the model flow field with the near-wall flow field.

Calculation of the flow over a slotted wall has traditionally involved simplifications such as a homogeneous wall treatment in which the flux through the open areas is distributed over the entire wall. Empirical correlations involving some features of the wall geometry such as openness ratio and slot width may be incorporated. A more complex treatment of slotted walls arises from a nonhomogeneous approach in

which the flow through the slots is modeled in some fashion and the rest of the wall is treated as solid. With either approach, the boundary specification may rely on experimental data such as the pressure distribution on the walls. Because many accurate measurements are required for sufficient resolution of the three-dimensional flow field, demanding experimental requirements are imposed. Wall interference approaches may be broadly classified as either predictive or assessment methods. Predictive methods are considered to be pretest examinations because measured data from the current test are not required for the simulation. Assessment methods may be viewed as posttest examinations because current experimental data are used in the expression of the wall boundary conditions. Several computational techniques have been used to examine wall interference effects in the NTF (refs. 3-5). Reference 3 describes an assessment approach that uses measured wall pressure data and a homogeneous slotted-wall assumption within a transonic small disturbance (TSD) flow solution. The method of reference 4 is a predictive technique that also combines a homogeneous outer boundary with a TSD solution. Reference 5 describes an assessment method in which a simulation of discrete slotted-walls is combined with a panel method formulation.

Wall interference calculations may be performed by obtaining two computational solutions of the same aircraft configuration: one solution for an aircraft bounded by walls and the other for an aircraft in

“free air.” Assuming that the pertinent flow physics are accurately modeled, the differences between the two solutions give an indication of the disturbances that the walls induce on the model flow field and provide insight for possible wall interference corrections to wind tunnel data. In the current work a predictive technique is developed in which a discrete slotted-wall model is incorporated within a TSD flow solution method. This approach features the ability to analyze aircraft flow fields with a nonlinear governing equation that includes possible discrete-slot interactions and at the same time allows independence from experimentally measured wall data. A free-air outer boundary condition is included to enable tunnel versus free-air comparisons to be made. The slotted walls may also be treated as homogeneous. The components of this method are described herein, and the effects of the parameters are demonstrated. Ultimately, the method is intended as a pretest indicator, showing whether wall interference effects are significant for a given model under specified flow conditions. Present data are insufficient for determining whether the method can accurately predict interference effects on the aircraft model. In this work, the suitability of the wall boundary conditions for simulation of the test section flow field is assessed by comparison of calculated results with available wall pressure data.

## Nomenclature

$a$	slot width (see fig. 3)
$b$	slot strip width (see fig. 3)
$C_D$	drag coefficient
$C_L$	lift coefficient
$C_M$	pitching-moment coefficient
$C_p$	pressure coefficient
$d$	distance between slot centerlines
$E$	unit step function (see discussion of eq. (4))
$h$	NTF test section half-width and half-height
$L$	homogeneous slot parameter (see eq. (3))
$l$	slot depth (see fig. 3)
$M$	Mach number
NTF	National Transonic Facility
$n$	direction normal to wall

$Q$	normalized velocity potential of two-dimensional sink
$q$	slot volume flux
$R$	Reynolds number
$s$	transformed slot variable
$s_{p,o}$	value of $s$ corresponding to $y_{p,o}$
TSD	transonic small disturbance
$U$	streamwise velocity
$V$	normalized velocity of two-dimensional sink
$x$	streamwise direction
$y$	spanwise direction
$y_l$	vertical direction in slot local coordinate system
$y_p$	plenum pressure surface location
$y_{p,o}$	limiting value of $y_p$
$z$	vertical direction
$z_l$	spanwise direction in slot local coordinate system
$\alpha$	angle of attack
$\gamma$	ratio of specific heats
$\delta$	normalized plenum pressure (see eq. (7))
$\zeta$	vertical direction in computational domain
$\eta$	spanwise direction in computational domain
$\eta_a$	viscous reduction factor for slot width
$\eta_u$	viscous reduction factor for longitudinal velocity
$\xi$	streamwise direction in computational domain
$\rho$	density
$\sigma$	location of slot lip in transformed plane
$\phi$	velocity potential
$\phi_{z,o}$	spanwise velocity component at slot centerline
$\varphi$	velocity potential along slot centerline
Subscripts:	
$i$	inviscid value at slot entrance
$l$	local slot coordinate system

$n$	derivative with respect to normal direction
$o$	value at slot origin
$P$	value in plenum
$s$	representative slot value, including viscous effects
$W$	value at wall
$w$	value at wing
$x$	derivative with respect to $x$ direction
$y$	derivative with respect to $y$ direction
$z$	derivative with respect to $z$ direction
$\infty$	value at free-air or reference condition

## Procedure

The code developed herein consists of a transonic small disturbance (TSD) aerodynamic analysis method that allows different outer boundary treatments to simulate both free-air and test section flow over an aircraft configuration. A discrete-slot flow model is incorporated to allow prediction of the behavior of the flow near the slotted walls of the NTF test section (fig. 1). In a test section simulation, the TSD and slot flow solutions are performed simultaneously using an interaction technique. The TSD code is used to solve the aircraft flow field and supply the slot flow calculation with normal volume flux values at the wall. The slot geometry and normal flux are used by the slot flow model to determine the potential along each slot. These values of potential are then used by the analysis code as an updated outer boundary condition along the slots. On the solid portions of the top and bottom walls and on the side wall, the standard tangential-flow boundary condition is imposed. Thus, in a test section simulation, the outer boundary condition for the aerodynamic analysis is of mixed (nonhomogeneous) character, with potential specified in the slot regions and the normal gradient of potential specified on the solid portions.

In this section, descriptions of the different elements of the wall interference prediction code are given. The section briefly reviews the classical homogeneous wall boundary conditions included in the code, then proceeds with a development of the discrete-slot flow model. Next, the focus shifts to the aerodynamic analysis code that is used. A brief outline of the formulation is given, followed by the modifications and additions necessary for simulating the test section flow. Finally, the interaction procedure between the wall solution and the flow field solution is discussed.

## Wall Boundary Conditions

### *Homogeneous wall boundary conditions.*

Several forms of the classical linear homogeneous wall boundary conditions are commonly used. In the present work, as in reference 4, the integrated, generalized linear homogeneous formulations given by Keller in reference 6 are used. At a solid boundary, the condition to be satisfied is that no normal flow passes through the boundary. Thus, the normal velocity component vanishes at the wall, which is mathematically stated as

$$\frac{\partial \phi}{\partial n} = 0 \quad (1)$$

At an open-jet boundary, no pressure gradient is allowed to exist across the boundary. In the linear approximation, the pressure coefficient is proportional to the streamwise gradient of the velocity potential ( $C_p \approx -2\phi_x$ ). Because the external flow is quiescent ( $C_p = 0$ ), the approximation to this condition is given by

$$\frac{\partial \phi}{\partial x} = 0 \quad (2)$$

At a wall with several longitudinal slots, the linearized homogeneous condition states that the pressure gradient is balanced by the streamline curvature. The expression of this condition is

$$\phi_x + L \frac{\partial^2 \phi}{\partial n \partial x} = 0$$

where  $L$  is a geometry-dependent slot parameter given by

$$L = \frac{d}{\pi} \ln \left[ \csc \left( \frac{\pi a}{2d} \right) \right]$$

The integrated form of this condition as applied in the present work is written as

$$\phi + L \frac{\partial \phi}{\partial n} = 0 \quad (3)$$

*Discrete-slot boundary condition.* The discrete-slot model was developed over a period of years by several researchers, and the earliest presentation was a 1975 paper by Berndt and Sörensen (ref. 7). The effort evolved from what was initially an attempt to develop an improved homogeneous wall condition using a theoretical approach that was consistent with certain observations of experimental slot flow. Berndt developed an inviscid, three-dimensional theoretical representation of the flow through longitudinal slots in which the flow leaving the test section through each slot is treated as a thin

jet while the return flow admits quiescent plenum air as shown in figure 2 (ref. 8). The model incorporates a quadratic crossflow velocity term (normal to the slotted wall) that is neglected in the linearized theories. Karlsson and Sedin (ref. 9) presented an implementation of the Berndt theory for an axisymmetric test section in which the steps in the solution process were detailed, although the research was directed toward the inverse problem of designing interference-free slot shapes. A formulation that includes a simple accounting for viscous effects in the axisymmetric model is presented in reference 10. In a separate effort, the basic ideas of the Berndt inviscid slot flow model are extended to a formulation that does not require an axisymmetric test section geometry (ref. 11). For the axisymmetric case, Berndt performed a matched asymptotic expansion of the test section and slot flow fields that resulted in an improved homogeneous outer boundary condition. In the extension to nonaxisymmetric test sections, a homogeneous outer condition no longer results. The asymptotic matching is performed in a more localized sense; each slot is treated separately and has its own local matching. The effect is that each slot is "smeared" somewhat in the lateral direction. In distinct slot regions that are wider than the slots, flow normal to the wall is permitted. The slot regions are separated by solid regions in which there is no flow normal to the wall. The result is a mixed outer boundary condition for the test section flow calculation in which  $\phi$  is specified on the slot strips and  $\phi_n$  is specified in the solid-wall regions (fig. 3). The viscous parameters of reference 10 are incorporated in the nonaxisymmetric slotted-wall model in reference 12. The slot model of references 11 and 12 is used in the current work.

In formulating the slot boundary condition, the intent is to create a velocity profile across the slot strip that simulates the flow through a slot in a far-field sense (as seen from the model location in the test section). This approximation is carried out by defining a slot strip that is slightly wider than the actual slot (fig. 3). A solution for the flow through a slot involves a solution of two first-order ordinary differential equations along the slot centerplane. One equation gives the location of a surface along which the plenum pressure applies. This surface, denoted  $y_p$ , may be considered as the boundary between the test section flow and the plenum (fig. 2). The plenum is assumed to be quiescent; no modeling of the flow is done inside the plenum, and the value of the plenum pressure is an input constant that is imposed on the plenum side of  $y_p$ . The limiting depth that  $y_p$  is allowed to extend into the plenum is denoted by

a similar surface  $y_{p,o}$ , which is a function of the slot geometry only. When  $y_p$  reaches  $y_{p,o}$ , the slot flow is assumed to separate into the plenum as a thin jet (fig. 2). The second differential equation is a normal momentum equation that expresses the pressure difference maintained by the slot. The momentum equation is applied through the slot from the outer region of the test section to the plenum pressure surface. With a known plenum pressure and the momentum equation, which gives the pressure gradient maintained by the slot, the pressure at the boundary of the test section (that is, at the slot entrance) is determined. Because the pressure coefficient is cast in terms of the gradient of potential, the integrated solution actually yields the potential along the slot centerline  $\varphi$ . After this centerline potential is known, the potential across the entire slot strip is given by the asymptotic matching.

The details of the slot model are now presented. Each slot is treated separately and has its own local coordinate system in which  $x$  corresponds to the free-stream flow direction,  $y_l$  to the normal or crossflow direction (positive outward into the plenum), and  $z_l$  to the spanwise direction (fig. 3). For a given slot, the wall surface is located at  $y_l = 0$ , the slot centerplane is given by  $z_l = 0$ , and  $z_l$  ranges between  $+b/2$  and  $-b/2$ , where  $b$  is the width of the slot strip. The slot flow formulation in the slot centerplane is based on a conformal transformation to a potential flow source/sink in the far-field limit (infinitely deep in the slot). (See ref. 8.) Let  $Q$  denote the normalized velocity potential of an isolated source/sink of unit width and flux, and  $V$  denote the corresponding velocity. The equation that describes the location of the plenum pressure surface is (ref. 11)

$$\frac{dy_p}{dx} = \frac{q_s V}{a_s} - E \frac{y_p}{a_s} \frac{da_s}{dx} \quad (4)$$

where  $a$  is the slot width and  $q$  is the normal volume flux per unit length through the slot. The subscript  $s$  denotes a representative slot value in which viscous effects have been included. The viscous model will be discussed below. Equation (4) states that the slope of the plenum pressure surface is proportional to the local flow angle. The second term on the right side is a one-dimensional correction for varying slot width, where  $E = 1$  inside the slot and  $E = 0$  outside the slot. The expression defining  $y_{p,o}$  (ref. 9) is

$$\frac{y_{p,o}}{a_s} = \frac{l}{a_s} + \frac{\ln(2)}{\pi} \left\{ 1 + 2 \exp \left[ -2 \left( 1 + \frac{\pi l}{a_s} \right) \right] \right\} \quad (5)$$

where  $l$  is the depth of the slot. When the value of  $y_p$  given by equation (4) exceeds  $y_{p,o}$ , then  $y_p$  is replaced

by  $y_{p,o}$ . Thus, an integration of equation (4) along the slot, subject to the constraint of equation (5), yields the location of the plenum pressure surface.

The crossflow momentum equation in the slot centerplane is developed by considering a two-dimensional crossflow plane at a given  $x$  location. The equation (ref. 11) is

$$\begin{aligned} \frac{d(\varphi - \varphi_o)}{dx} + \frac{\rho_s}{\rho_\infty} \frac{U_s}{U_\infty} \frac{d}{dx} \left( \frac{U_s}{U_\infty} \left\{ q_s Q \right. \right. \\ \left. \left. - \frac{q_s}{\pi} \left[ \frac{1}{2} + \ln \left( 4 \frac{a_s}{b} \right) \right] - \frac{y_p^2}{a_s} \frac{da_s}{dx} \frac{E}{2} \right\} \right) \\ = -\frac{1}{2} \frac{\rho_s}{\rho_\infty} \left( \frac{U_s}{U_\infty} \right)^2 \left( \frac{q_s V}{a_s} - E \frac{y_p}{a_s} \frac{da_s}{dx} \right)^2 - \delta \end{aligned} \quad (6)$$

where  $\varphi_o$  is the value of  $\varphi$  at the slot origin. The normalized plenum pressure parameter  $\delta$  is defined as

$$\delta = \frac{p_P - p_\infty}{\rho_\infty U_\infty^2} \quad (7)$$

and is equal to one half of the pressure coefficient as typically defined. Also, note the presence of the quadratic crossflow velocity term on the right side of equation (6). Equation (6) is integrated along the slot to give the distribution of the slot centerline potential  $\varphi$ . The asymptotic matching defines the relationship between  $\varphi$  and the potential across the entire slot strip. This expression is written in the local slot coordinate system as (ref. 11)

$$\phi(x, 0, z_l) = -\frac{4q_s}{\pi} \left( \frac{z_l}{b} \right)^2 + \varphi + \phi_{z,o} z_l \quad (8)$$

where  $\phi_{z,o}$  is the sidewash (spanwise) velocity. The sidewash velocity is calculated along the centerline of each slot using the potential from the TSD solution. The values of potential given by equation (8) are ultimately imposed along the slot strips as a boundary condition for the TSD solution.

Several physical phenomena are considered in extending the slot flow model to include viscous effects (ref. 10). The streamwise velocity at the slot entrance is assumed to behave as in a shear flow, with a corresponding loss of longitudinal momentum. Similarly, the crossflow velocity through the slot is assumed to have a profile similar to that of a boundary layer flow, with an associated increase in core velocity. These behaviors are simulated by viscous reduction factors for the longitudinal velocity  $\eta_u$  and slot width  $\eta_a$ , defined as

$$U_s = \eta_u U_i \quad (9)$$

$$a_s = \eta_a a \quad (10)$$

where  $U$  is the local longitudinal velocity component at the slot entrance,  $a$  is the slot width, and the subscript  $i$  denotes the inviscid value at the slot entrance. To keep the slot model as simple as possible, the viscous reduction factors are assumed to have constant values along the slots.

Small perturbation approximations are used to derive expressions for the necessary velocity and density ratios along the centerline of each slot. Using small perturbation approximations, the local density and streamwise velocity are

$$\frac{\rho_i}{\rho_\infty} = 1 - M_\infty^2 \phi_x \quad (11)$$

$$\frac{U_i}{U_\infty} = 1 + \phi_x \quad (12)$$

Using equation (9) and assuming constant total enthalpy and pressure, the characteristic slot flow density can be written as (ref. 10)

$$\frac{\rho_s}{\rho_i} = \left[ 1 + \frac{\gamma - 1}{2} M_i^2 (1 - \eta_u^2) \right]^{-1} \quad (13)$$

where

$$M_i = M_\infty [1 + (\gamma - 1) \phi_x]^{1/2} \quad (14)$$

Combination of equations (11) and (13) yields the required expression for the slot density ratio, and the streamwise component of the local slot flow velocity is written using equations (9) and (12). These expressions are

$$\frac{\rho_s}{\rho_\infty} = \frac{1 - M_\infty^2 \phi_x}{1 + \left[ \frac{\gamma - 1}{2} M_i^2 (1 - \eta_u^2) \right]} \quad (15)$$

$$\frac{U_s}{U_\infty} = (1 + \phi_x) \eta_u \quad (16)$$

The normal volume flux  $q$  is required in the solution of the slot flow equations. Estimates for  $q$  are provided through spanwise integration, across the slot strip, of the normal velocity component at the wall, or

$$q_s = \frac{\rho_i}{\rho_s} \frac{U_\infty}{U_s} \int_{-b/2}^{+b/2} \phi_n dz_l \quad (17)$$

The normal velocities over each slot strip are obtained from the TSD solution of the test section flow field. In reference 11 researchers found that using numerically integrated values for  $q$  in this manner gave results that were insensitive to the value chosen for  $b$ .

The slot flow formulation is completed with the addition of the relations describing the source/sink potential and velocity functions  $Q$  and  $V$ . As mentioned above, these functions are derived through use

of a conformal transformation. An outline of the formulation is given in the appendix of reference 8, and the results are summarized here for convenience. In terms of the transform variable  $s$ , the source/sink functions (ref. 8) are given by

$$Q = -\sigma \ln s \quad (18)$$

$$V = \frac{\sigma}{\sqrt{s^2 + \sigma^2}} \quad (19)$$

The parameter  $\sigma$  denotes the location of the corner of the slot lip in the transformed plane, where  $\sigma = 1/\pi$ . Finally, the relationship between the physical and transform variables (ref. 9) is expressed by

$$\frac{y_p}{a_s} = - \left[ \sqrt{s^2 + \sigma^2} + \sigma \ln \left( \frac{\sqrt{s^2 + \sigma^2} - \sigma}{s} \right) \right] \quad (20)$$

To summarize, a simultaneous solution of equations (4) and (6) yields the distribution of  $\varphi$  along the centerline of a slot. Equations (18) and (19) and the auxiliary expression given by equation (20) define the functions that appear in these differential equations. After  $\varphi$  is determined, the potential over the entire slot strip is specified by equation (8). A discussion of the integration technique used in the current work is presented in appendix A.

### Aerodynamic Analysis

The aerodynamic analysis calculation is performed with a three-dimensional TSD method developed by Rosen (ref. 13) as an extension of the work of Boppe (ref. 14). The method is based on a formulation of the TSD equation that has been extended by the retention of some higher order terms usually neglected in TSD formulations. This method allows the treatment of complex configurations that include a wing, fuselage, pylons, and underwing stores. A global coarse grid extends over the entire flow domain, and much finer embedded grids are used to give good resolution in the wing, pylon, and store regions. In the coordinate system used,  $x$  denotes the direction of the free stream,  $y$  is the spanwise direction, and  $z$  is the vertical direction. The governing equation is written as

$$T\phi_{xx} + U\phi_{xy} + V\phi_{yy} + \phi_{zz} = 0 \quad (21)$$

where

$$T = 1 - M_\infty^2 - (\gamma + 1) M_\infty^2 \phi_x - \frac{\gamma + 1}{2} M_\infty^2 \phi_x^2$$

$$U = -2M_\infty^2 \phi_y$$

$$V = 1 - (\gamma - 1) M_\infty^2 \phi_x$$

The terms containing  $\phi_x^2\phi_{xx}$ ,  $\phi_y\phi_{xy}$ , and  $\phi_x\phi_{yy}$  are the higher order terms that are typically neglected in TSD formulations. The  $\phi_x^2\phi_{xx}$  term improves the transition between subsonic and supersonic zones, and the  $\phi_y\phi_{xy}$  and  $\phi_x\phi_{yy}$  terms are retained to aid in the resolution of swept shock waves. An upwind, rotated-differencing scheme is used in the numerical relaxation procedure to ensure that the proper domain of dependence is maintained in supersonic flow regions. Rosen developed a scheme specifically for this modified TSD formulation in which the rotation is determined using the coefficients  $T$ ,  $U$ , and  $V$ . As a result of the extended TSD formulation and the rotated-differencing scheme, the method can accurately treat highly swept and tapered wings at high transonic Mach numbers with good numerical stability and accuracy (ref. 13).

### Wall Interference Code

The code created in the course of the present work is constructed by making additions and modifications to the Rosen code. These alterations include a new grid generation scheme for the global coarse grid, the calculation and imposition of the different outer boundary conditions, the simulation of the model support sting, and the ability to simulate a finite-length test section. Each of these features is discussed here.

**Grid generation.** Several factors must be considered in developing the grid generation scheme for the global coarse grid. To examine wall interference effects, solutions obtained from the test section simulation are compared with free-air solutions. To eliminate grid-biasing differences from these comparisons, the test section grid is wholly contained within a larger free-air grid with outer boundaries that tend toward infinity (ref. 4). Grid planes are located at each boundary of the test section, including the test section walls as well as appropriate inflow and outflow locations. At the boundary of the test section grid, a smooth transition to the free-air grid is required. The total number of grid points should be kept to a reasonable number, while maintaining adequate grid resolution at the walls without sacrificing grid resolution at the model location. The spacing in the original Rosen code was used as a guide to determine the grid spacing near the model in each of the coordinate directions. In both the Rosen code and the present code, a vertical symmetry plane is assumed to exist at the centerline of the aircraft. As a result, only half the flow domain is modeled. A brief discussion of the grid scheme will now be given,

and details of the grid generation are contained in appendix B.

The grid in the streamwise ( $x$ ) direction is divided into five regions and is symmetric about the midpoint of the central region. (See fig. B1.) The central region, which contains the wing, consists of uniform spacing that results in the finest resolution of the streamwise grid. The two regions that bound the central region extend from the respective edges of the central region to the test section inflow and outflow planes. A mild stretching function is used in these regions so that the spacing is still reasonably fine near the test section boundaries. In the regions outside the test section, a strong stretching function is used to rapidly extend the grid toward upstream and downstream infinity. For the aircraft geometries currently being examined, a total of 111 grid points are used in the streamwise direction for a free-air calculation. Of these grid points, 17 are clustered within the wing region. For a test section calculation, a total of 84 streamwise grid points are used with the current geometries.

A discussion of the spanwise grid generation requires a brief explanation. In the original Rosen scheme, the spanwise spacing is determined by the wing span, with the geometric wingtip midway between two grid planes. No attempt is made to predict the actual flow at the tip since the region is dominated by rotational and viscous effects that cannot be modeled with a TSD approach. In the context of potential flow, the intent is to avoid performing a calculation too near the tip while presuming that the lift goes to 0 at the tip. Thus, location of the wingtip midway between two grid planes gives the best treatment of the tip region. In the current scheme convenience dictates that the spanwise grid spacing is determined by the test section geometry rather than by the wing geometry. The geometry of the NTF test section is such that slots are located at one-sixth, one-half, and five-sixths of the test section half-width (fig. 1). Thus, a uniform grid spacing with an increment equal to some fraction of one sixth of the test section half-width ensures that a grid plane is aligned with each slot as well as with the test section sidewall. A consequence of the present technique is that the wingtip has an arbitrary location between two grid planes. Care must be taken to treat the tip region adequately, as discussed above. To generate the spanwise grid, the spacing in the test section region is varied by altering the total number of grid planes in increments of six until enough planes fall on the wing (typically 15–20). To avoid performing an inviscid calculation too near the wingtip, the outermost of these wing grid planes may be ignored if too

close to the geometric wingtip (that is, within 2 percent of the semispan). The lift is assumed to go to 0 at the tip, as in the original method. This procedure was found to give spanwise lift results similar to those of the original method. Outside the wall, a strong stretching function is used again to extend the grid toward infinity. For the free-air calculation, a total of 45 grid points is used in the spanwise direction. Of these points, 20 fall on the model (18 on the wing) for the geometries currently examined. When a test section simulation is performed, the total number of spanwise grid points decreases to 37.

Spacing grid points uniformly in the vertical direction while maintaining adequate resolution near the wing would require an excessive number of grid points (that is, double the number used in the spanwise direction for the same spacing). Ideally, the grid would have the finest spacing near the model, fine spacing near the wall, and coarser spacing between these regions. In the grid generation scheme that was developed, three zones are used inside the test section to give the desired spacing (fig. B1). The central zone is symmetric about the wing plane and extends over half the test section height. A mild stretching is used in this region, which gives the finest spacing at the wing. Between the edges of the central zone and the walls, a similar stretching is used to slightly decrease the spacing as the walls are approached. The stretching functions in the two regions (near the upper and lower walls) may differ slightly because the wing plane may not be in the exact center of the test section. Outside the walls a strong stretching function is used to give the required extension toward infinity. The free-air grid currently used has 63 points in the vertical direction. With the test section grid the number of points decreases to 51.

The above discussion refers to the work that was done on the global coarse grid. Note that an embedded fine grid is used to resolve the details of the wing flow field (ref. 13). The wing fine grid is automatically generated, based on the wing geometry and the global coarse grid. Fine grid planes coincide with the spanwise coarse grid planes that lie on the wing; thus, for the current geometries there are 18 spanwise fine grid planes. Each fine grid plane has 130 points in the streamwise direction. Of these, 100 of the points are located along the chord at equally spaced increments. The extent of the fine grid in the streamwise and vertical directions is a set percentage of the local wing chord length. The fine grid extends from 20 percent chord upstream of the leading edge to 10 percent chord downstream of the trailing edge. In the vertical direction, the fine

grid extends from 10 percent chord below the wing to 30 percent chord above the wing.

**Test section features.** Two features added to the code to approximate the flow in a test section more accurately are simulations of a model support sting and a finite-length test section. The cross-sectional area of the sting is generally of the same order of magnitude as that of the model fuselage. Thus, in the test section environment the sting induces a significant blockage downstream of the model and influences the wall pressure coefficients. A simulation of the sting is included here because the results of the code are compared with measured wall pressures. In the code, the sting is treated like an axisymmetric body that is an extension of the fuselage, which is an adequate model because the fuselage itself is treated as an axisymmetric body. Note that this representation is realistic for configurations such as the Pathfinder I model with its rear-mounted axisymmetric sting (fig. 4(a)). With blade sting arrangements such as the Boeing 767 model and its high-mounted sting (fig. 4(b)), the flow in the sting region will not be accurately simulated. At a minimum the present simple sting representation is expected to approximate the gross blockage effects.

In the test section simulation, the test section inflow plane coincides with the beginning of the slots and the outflow plane with the end of the slots. From a numerical standpoint, these choices are found to give the best behavior in the inflow and outflow regions. To justify these choices in a physical context, the geometry of the NTF test section must be considered. In the NTF test section, the slots begin 6 in. downstream of the test section entrance and gradually open from an initial width of 0 (table 1). Because the slots begin so close to the test section entrance, the slot beginning is a suitable location for the computational inflow plane. The slots terminate in a reentry region in which a step discontinuity in wall height is coupled with reentry flaps to guide inflow from the plenum (fig. 1). The reentry region is dominated by viscous mixing near the wall, especially downstream of the step. Because accurate modeling of the viscous mixing region is difficult in an inviscid calculation, this region is excluded from the calculation for convenience. The calculated model forces and moments were insensitive to the movement of the computational outflow plane location over the extent of the reentry region, and the calculated wall pressure coefficients showed only a localized sensitivity to the outflow location. Thus, the outflow plane may be located at the end of the slots, just upstream of the test section reentry region. A corresponding outflow boundary condition is discussed below.

**Imposition of boundary conditions.** For a free-air calculation, the outer boundary conditions are the same as those in the original code (ref. 13). At all outer boundaries other than downstream infinity, the boundary condition is no perturbation potential, or  $\phi = 0$ . At downstream infinity, the condition is  $\phi_x = \phi_{xx} = \phi_{xy} = 0$ . The imposition of this condition means that a Laplace equation is solved in the outflow plane (that is,  $\phi_{yy} + \phi_{zz} = 0$ ) to allow for the wing wake and circulation. At the centerline symmetry plane ( $y = 0$ ), the condition is that the spanwise flow component vanishes, or  $\phi_y = \phi_{xy} = 0$ . The test section simulation requires modifications in the formulation and imposition of the outer boundary conditions. At the inflow plane, the condition is still  $\phi = 0$ , and the symmetry plane condition is also unchanged. A wall boundary condition is imposed at each of the walls. The capability exists in the code to treat each wall using the homogeneous solid, open, or slotted boundary conditions and additionally, to treat the floor and ceiling using the discrete-slot model. The homogeneous conditions are applied in the same manner as in reference 4. When the discrete-slot model is used, the outer boundary condition becomes mixed in character. In the solid-walled portions, the homogeneous solid-wall condition ( $\phi_n = 0$ ) is applied. In the slot regions, the value of potential obtained from the slot solution is imposed.

The treatment of the outflow boundary in the context of a finite-length test section is more difficult. In terminating the solution ahead of the reentry region, the flow is not uniform at the outflow boundary. Examination of wall pressure data from the NTF shows that the wall pressure coefficient in the region of the outflow plane is still changing; that is, in general  $\phi_{xx}$  is nonzero. In the current work, the condition imposed is that  $\phi_{xx}$  is equal to some constant in the outflow plane. The value of the constant is determined by comparison with experimental wall pressure data. The value of the constant affects only the flow near the outflow plane and not the model forces and moments. Note that  $\phi_{xx}$  represents a longitudinal flow acceleration, approximating the derivative of the pressure coefficient with respect to  $x$ . Conceivably, the proper specification of this slope in the outflow plane is a realistic alternative to modeling the viscous reentry region because it mimics the overall effect of the reentry region on the flow. Although  $\phi_{xx}$  is unlikely to be constant over the entire outflow plane, such a simple condition may be sufficient to characterize the local flow behavior.

**Consideration of plenum pressure.** The value of the plenum pressure must be specified in

the slot flow model. The plenum pressure governs the relative amounts of outflow and inflow through the slots as well as the total amount of flux through the slots. In reality the plenum pressure evolves passively to a value that corresponds to an equilibrium in the slot and reentry flow. The plenum pressure depends on several factors such as the free-stream test conditions, the model geometry, the settings of the test section walls and reentry flaps, and the viscous mixing in the plenum and the reentry region. Thus, theoretical calculation of the plenum pressure would be difficult. In the inviscid method of reference 5, a unique value of plenum pressure resulted in the proper numerical behavior of the slot fluxes for a given flow configuration. Because the solution was sensitive to the value of the plenum pressure, an inverse approach was used in reference 5 in which the slot flux and the reentry-region streamline slope were specified, and the plenum pressure was determined in the course of solution. In the present method, the intent is to simulate the effect of the reentry region by specifying the outflow value of  $\phi_{xx}$ , as discussed above, and to allow the slot fluxes to evolve, based on the specified plenum pressure. Because the plenum pressure is used to artificially force the proper slot flow behavior, including the effects of viscosity, the specified value of the plenum  $C_p$  is generally not the same as the experimental value.

The specified plenum pressure is felt throughout the test section. This effect is illustrated by consideration of the linearized expression for the pressure coefficient,  $C_p = -2\phi_x$ . In the linearized sense a nonzero plenum  $C_p$  induces a longitudinal velocity perturbation  $\phi_x$  through the test section. This perturbation results in an increment to the Mach number such that  $M$  is no longer equal to  $M_\infty$  at the inflow plane. The free-stream Mach number must be adjusted to ensure that the Mach number at the test section entrance (that is, the test Mach number  $M$ ) remains the same when the plenum  $C_p$  is changed. These Mach number adjustments can be determined using an expression derived from the isentropic pressure relation (ref. 15). The appropriate equation is

$$M^2 = \left[ \left( 1 + \frac{\gamma-1}{2} M_\infty^2 \right) (\gamma M_\infty^2 \delta + 1)^{(1-\gamma)/\gamma} - 1 \right] \frac{2}{\gamma-1} \quad (22)$$

**Interaction and solution.** The solution procedure for a test section simulation requires an interaction technique: the aerodynamic solution and the slot flow solutions are coupled to obtain an overall solution. The aerodynamic solution is an iterative procedure, while the slot flow solution involves

a marching procedure from known conditions at the slot beginning. The slot flow and the test section flow are coupled through the wall values of the potential and the normal gradient of potential. A slot flow solution requires specification of the normal gradient of potential along the slot. The slot solution then provides the value of potential along the slot, which is imposed as an updated outer boundary condition on the aerodynamic solution. This iterative interaction procedure continues with an exchange of updated values of potential and the gradient of potential until the aerodynamic solution converges. The wall pressure coefficients are calculated as the final step of the solution. (With a free-air calculation, the pressure coefficients are calculated at locations equivalent to the wall positions.) The typical expression for the small perturbation pressure coefficient is used. The appropriate expression is

$$C_p = - \left[ 2\phi_x + (1 - M_\infty^2) \phi_x^2 + \phi_y^2 + \phi_z^2 \right] \quad (23)$$

An interaction step begins with a calculation of the normal potential gradient  $\phi_n$  over each slotted wall. At each longitudinal ( $x$ ) grid station of the global grid, a spanwise cubic spline integration of the  $\phi_n$  values is performed across each slot strip to obtain the local values of the slot volume flux  $q$ . This curve-fit integration is used because the edges of the slot strips do not necessarily coincide with spanwise grid-plane locations. The result is the distribution of  $q$  along the centerline of each slot with  $q$  values at the global coarse grid  $x$  locations. The slot flow equations are integrated using a fourth-order Runge-Kutta procedure that requires the functional values to be given at uniform increments. Thus, a cubic spline interpolation of the  $q$  values is performed along each slot to give values of  $q$  at the proper intervals. The slot equations are then integrated with the Runge-Kutta method to yield values of  $\varphi$  along each slot. A cubic spline interpolation is performed to yield values of  $\varphi$  at the global coarse grid  $x$  locations. Equation (8) is then applied with these values to give the potential over each slot strip. The imposition of the potential values along the slot strips as a boundary condition in the TSD code requires a numerical underrelaxation to achieve a stable procedure. The value of the relaxation factor depends on the frequency with which the slot solution is updated. An updated slot solution is currently performed with every other iteration of the TSD code to reduce the time required for the slot calculation by half. Any further reduction in the update frequency adversely affects the solution convergence. With an update frequency of every second iteration, a slot strip relaxation factor of 0.20 is currently used.

Because the slots begin at the inflow plane, the initial conditions for each slot integration are that the plenum pressure surface is level with the wall ( $y_p = 0$ ) and that the potential has a value of 0 ( $\phi = \phi_o = 0$ ). Care must be taken in beginning the slot integration. The NTF slot geometry is such that the slots gradually open from an initial width of 0. Because the slot width is used as a normalization factor in the slot flow equations, a singularity exists at the slot origin. In the present method, the slot solution actually begins slightly downstream of the geometric slot origin so that the solution is initiated with a nonzero slot width. This approach is analogous to allowing no flux through the slot when the slot width is 0. The step size chosen for the Runge-Kutta integration is such that 228 intervals are used along the slot. This number is judged to be sufficient because doubling the number of intervals results in no changes in the solution.

The code has core memory requirements of approximately 2.1 megawords and is presently implemented on a Cray Y-MP computer at Langley Research Center. The code is allowed to run until the prescribed number of iterations are completed. For the results shown here 100 crude and 700 crude/fine iterations are used. This number of iterations is sufficient to allow the maximum change in potential to decrease by at least three orders of magnitude. The solution time varies, depending on the type of solution, with typical solution times on the Cray Y-MP as follows. An inviscid solution with discrete slotted walls requires 490 CPU sec. An inviscid calculation with homogeneous wall boundary conditions takes 440 CPU sec, which indicates that the discrete-slot calculations increase the solution time by about 11 percent. An inviscid free-air calculation requires 690 CPU sec. This 57-percent increase over the other homogeneous conditions is due to the additional number of grid points required by the free-air solution.

## Analysis

An analysis of the test section simulation is conducted in this section. Elements of both the test section and the aircraft model representations are considered, with the goal of comparing the simulation results with measured data. Test section wall pressure coefficients are the primary data used for comparison. Note that a limited amount of suitable NTF wall pressure data currently exists because only simple transport aircraft configurations (fuselage and wing) are considered for calculation in this study and because acceptable tare pressure data must also exist (as discussed below). The data from single tests

of the Pathfinder I and Boeing 767 models are used here (fig. 4). To compare measured and calculated wall pressures, the angle of attack in the simulation is adjusted to obtain a calculated  $C_L$  that matches the measured  $C_L$ . Early work verified that the calculated wall pressures are largely a function of the lift generated by the model. Although the code includes the provision to calculate the wing boundary layer, the boundary layer affects the wall  $C_p$  values only indirectly through a slight change in the wing lift. Because the lift is easily adjusted by changing the angle of attack, the code is executed with no boundary layer calculation for the purpose of these studies. Additionally, note that the model configuration in the Pathfinder I test includes a horizontal stabilizer. Because this method is capable of treating only a single lifting surface, the effect of the horizontal stabilizer cannot be modeled.

This section begins with a brief comparison of the results of using different homogeneous wall boundary conditions, then presents a discussion of the measured wall pressures that are used herein for validation. The behavior of the test section simulation is then examined in detail with a demonstration of the effects of varying simulation parameters on the solution. Among these parameters are components of the discrete-slot flow model and elements of the test section representation. Next, the calculated and experimental pressure coefficients are used to select the combination of model parameters that gives the best simulation of the test section flow field. Finally, test section and free-air calculations are compared to illustrate the influence of the test section on the aircraft flow field.

## Homogeneous Boundary Calculations

The results of using various homogeneous wall boundary conditions are shown to illustrate the general influence of the outer boundary on the solution and to check in a simple way the behavior of the simulation method. The calculations are performed with the Pathfinder I model at a Mach number of 0.80 and an angle of attack of  $2.70^\circ$  to approximate cruise conditions for this aircraft. In figure 5, the wall pressure coefficients with the open-jet, solid, and slotted boundary conditions are compared with those calculated at locations equivalent to the walls using the free-air boundary condition. The sidewall is treated as solid in each of the test section calculations. The fuselage of the Pathfinder I model is approximately between stations 11 and 15, and the wing is centered near station 13. The figure shows that solid boundaries result in the greatest flow acceleration through the model region and, therefore, the largest

blockage effect. No model-induced pressure variation is present on the upper and lower open-jet boundaries, as expected. The  $C_p$  values with the slotted-wall calculation fall between those of the open-jet and solid-wall calculations, which illustrates the partially open behavior of the slotted wall. The slotted-wall and free-air results are similar, illustrating the reduction of wall interference with slotted walls. Each test section calculation shows a larger disturbance than the free-air calculation on the solid sidewall, although the trends among the three types of wall boundaries are still as expected. The calculated force coefficients for these cases are listed in table 2. Again, the trends are as expected: solid walls cause an increase in the  $C_L$ , open boundaries result in a decrease in  $C_L$ , and, slotted walls give the closest agreement to the free-air  $C_L$ .

### Examination of Experimental Data

Typical wall pressure measurements from the NTF are shown to illustrate features of the data. Considerable scatter has been found to exist in NTF wall pressure data (refs. 16 and 17). Likely, the majority of this scatter is due to imperfections in either the pressure orifices or the local wall surface. Because scatter due to such systemic sources is generally repeatable, the data quality can be greatly improved by subtraction of tare, or tunnel-empty, pressure values. As noted in reference 17, the use of a tare in test section simulations depends on the modeling philosophy because the subtraction of a tare also eliminates disturbances due to other test section flow phenomena. Tared wall pressures are used in the method of reference 3, while the method of references 5 and 16 uses smoothed, untared pressure data because the intent is to model the complete test section flow field. In the current work, the use of a tare is consistent with the problem formulation. Subtraction of a tare removes not only the scatter in the pressure data but also perturbations that result from tunnel-empty wall boundary layers and flow angularity, non-parallel walls, and other test section asymmetries that are not modeled.

The NTF has nine longitudinal rows of pressure orifices: three in the ceiling, three in the floor, and three in one of the sidewalls (fig. 1). A row of orifices is located along the centerline of each of these walls. Both the ceiling and the floor contain two additional rows at spanwise locations of one third and two thirds of the test section half-width (toward the instrumented sidewall). Each ceiling and floor row is located in the middle of a solid slat that separates two slots. The two additional rows in the instrumented sidewall are located halfway between the floor and

centerline and halfway between the centerline and ceiling. Typical tared and untared wall pressure measurements are shown in figure 6. The data were obtained with the Pathfinder I model at  $M = 0.80$ ,  $R = 4.0 \times 10^6$  per foot, and  $C_L = 0.514$ . The data used as a tare were obtained from a tunnel calibration test in which the test section contained only a slender centerline probe that extended the length of the test section. The tare data were obtained at conditions of  $M = 0.80$  and  $R = 6.1 \times 10^6$  per foot, the closest available to the Pathfinder I conditions. The data from the ceiling orifice rows are shown in figure 6(a). Data from each floor and sidewall row are shown in figures 6(b) and 6(c), respectively. The data show that the application of a tare greatly reduces the data scatter in all the pressure signatures. Use of the tare also allows identification of plugged or leaking orifices, and the data from such orifices are removed from the tared distributions.

Note that the wall  $C_p$  values shown in figure 6 do not diminish to 0 at the test section entrance for either the tared or untared data. This behavior is a reflection of the reference values originally used to formulate the coefficients. Figure 6 also shows that the longitudinal pressure gradient on each wall is changed in taring the data, which indicates the existence of tunnel-empty gradients that are subtracted with the tare. These gradients presumably arise from tunnel phenomena other than wall interference, as discussed above, and cannot be predicted by the current method. A final comment concerns the  $C_p$  values near the outflow plane. The centerline probe begins to increase in diameter at station 18 to fit the NTF model support system. This change in diameter induces a flow gradient over the aft portion of the test section, which means that the wall pressures in this region are not true tunnel-empty values. Thus, in subtracting the centerline probe wall pressure data as a tare, the tared values downstream of station 18 are likely to be incorrect.

### Characteristics of Test Section Solution

Calculated and measured wall  $C_p$  values are compared in the following figures. Recall from the discussion preceding equation (22) that the calculated value of  $C_p$  at the test section entrance should be  $2\delta$  (because  $\delta$  is defined as  $C_p/2$ ). In each figure, the measured wall  $C_p$  values have been uniformly shifted by a constant value so that the calculated and experimental  $C_p$  values are in agreement at the test section entrance. The same offset is applied to each of the nine rows of pressure measurements, and the value of the constant depends on the value of  $\delta$ . This approach is analogous to recalculating the

measured wall pressure coefficients using the same reference conditions assumed in the simulation.

The general behavior of the test section solution and the effect of varying certain simulation parameters is now examined. For these illustrations, the geometry of the Pathfinder I model is used (fig. 4(a)). The model is located between tunnel stations 10.7 and 14.9. Because the code is capable of treating only a single lifting surface, the modeled configuration consists of the wing and fuselage with no horizontal stabilizer.

**Effect of slot model parameters.** The test section solution will be illustrated with the Pathfinder I model at a free-stream Mach number of 0.8 and an angle of attack of  $2.70^\circ$ . Other solution parameters include a slot depth of 0.75 in., a slot strip width of 5 in., and an outflow-plane  $\phi_{xx}$  of 0. The sting representation is not included. Calculated wall pressure distributions with two different values of plenum pressure are compared with measured coefficients along the centerline of each wall in figure 7. As seen in figure 7(a), large discrepancies exist between the calculated and measured values with  $\delta = 0$ . In particular, the gradients upstream of the model are not predicted, and the model-induced acceleration on the ceiling is underpredicted. A negative value of  $\delta$  greatly improves the agreement in these two regions (fig. 7(b)), although some disagreement still exists between the calculated and measured  $C_p$  values for the floor and ceiling in the region of station 10. The sidewall signature also shows that the location of the recompression aft of the wing is incorrect. In these figures, the decrease in pressure above the wing and the increase in pressure below the wing are indicative of the lift generation. Note that on the floor and ceiling,  $C_p$  at the inflow plane is exactly equal to the plenum  $C_p$  (that is,  $2\delta$ ), which must be true because the slots begin at the inflow plane. In each case, the Mach number at the inflow plane is 0.80, which means that  $M_\infty = 0.80$  with  $\delta = 0$  and  $M_\infty = 0.7964$  with  $\delta = -0.004$ . These values are determined using equation (22). The slot volume flux  $q$  through each slot for these two values of  $\delta$  is shown in figure 8. Positive  $q$  values represent outflow from the test section to the plenum, and negative values represent inflow to the test section. In general, outflow exists along the entire length of the floor slots, and the magnitude of the flux decreases as the distance from the tunnel centerline increases. The ceiling slots show similar outflow up to the model location, followed by strong inflow through the rest of the test section. Upstream of the model, the flow expands outward through all the slots, while the differences downstream of the model are due to generation of

lift. The slots reflect the downwash aft of the wing by showing a general downturn of the flow in this region. Comparison of figure 8(a) with 8(b) shows that lowering the plenum pressure increases the slot outflow and decreases the inflow, as expected. An alternate way of viewing the effect of plenum pressure is to note that varying  $\delta$  changes the overall slot flux gradient along the slots; decreasing plenum pressure tends to increase the slope of  $q$  with respect to  $x$ . Varying the plenum pressure also affects the calculated model lift. As  $\delta$  is changed from 0 to  $-0.004$ ,  $C_L$  decreases from 0.5655 to 0.5601. This behavior makes sense qualitatively because a decrease in the plenum pressure aids the relieving action of the slots by increasing slot outflow.

Because the cross-sectional shape of the slot edge is not rectangular (fig. 9), the proper slot depth specification in the slot model is unclear. The slot lip initially has a depth of 0.354 in., and the beveled slot wall continues to a depth of 1.75 in. Downstream of station 5 the lip is rounded, and there is a smooth transition to the beveled wall. A comparison of the wall centerline  $C_p$  values obtained from solutions with various slot depths and the Pathfinder I model at  $M = 0.80$  and  $\alpha = 2.70^\circ$  is shown in figure 10. Slot depths of 0.354 and 1.75 in. are used as well as an intermediate depth of 0.75 in. The other solution parameters are the same as in the previous case, with  $\delta = -0.004$ . An increase in the slot depth from 0.354 to 1.75 in. increases the model  $C_L$  by 0.002. Figure 10 shows that increasing the slot depth increases the flow deceleration upstream of the model and increases the acceleration above the model. Deeper slots are able to maintain a larger pressure gradient between the test section and plenum so that the test section appears more closed (that is, more like a solid-walled test section). The effective slot depth should be between 0.354 and 1.75 in. because the flow entering the slot will probably not remain attached along the entire depth of the beveled wall. The effective slot depth may vary locally, depending on the existence (and magnitudes) of slot inflow or outflow. Given the shape of the slot edges, a shallow effective slot depth is currently felt to be realistic. A slot depth of 0.75 in. is used in the current study.

In the slot flow model, the effect of each slot is spread laterally over a slot strip of width  $b$ . The intent is to ensure a sufficient number of spanwise grid planes within each slot strip to adequately resolve the slot flow. The effect of varying  $b$  is shown in figures 11 and 12. The solutions are obtained with the Pathfinder I model at  $M = 0.80$  and  $\alpha = 2.70^\circ$ , and the other parameters include  $\delta = -0.004$  and  $l = 0.75$  in. Figure 11(a) shows the effect of using

$b$  values from 3 to 7 in. on the wall centerline pressure coefficients. With the current grid,  $b = 7$  results in five spanwise grid planes within each slot strip and seven grid planes on the solid slats between two slot strips. For  $b = 5$  or 3, three spanwise grid planes fall within each slot strip. Increasing the strip width generally yields more positive values of  $C_p$ , and increasing  $b$  from 3 to 5 in. causes a larger change than increasing  $b$  from 5 to 7 in. To gain further insight into the behavior of the slot model, figure 11(b) shows a comparison of the pressure coefficients that result when  $b = 5$  and 5.5 in. Each slot strip contains five spanwise grid planes with  $b = 5.5$  and three spanwise planes with  $b = 5$ . As shown in the figure, this change in strip width causes no change in the wall pressure coefficients. These results indicate that the solution is influenced more by the specified width of the slot strips than by the relative number of grid planes within the slot strips. The slot fluxes with  $b = 3$  and 7 are shown in figure 12. Increasing the strip width causes  $q$  to become more positive (or increases the gradient of the outflow). This effect is similar to that caused by lowering the plenum pressure. Since negative values of  $\delta$  are used in the current solutions, increasing the strip width causes the slotted wall to behave in a more open fashion, thus making the flux more sensitive to the influence of plenum pressure. As the strip width is increased from 3 to 5 to 7 in. at this angle of attack, the calculated model  $C_L$  changes from 0.5579 to 0.5601 to 0.5609. Because an increase of  $b$  has a diminishing effect, as shown in figure 11(a), a slot strip width of 7 in. is typically used in this study.

**Effect of test section parameters.** The effects of the model support sting and of changing the value of  $\phi_{xx}$  in the outflow plane are illustrated next. The change in the solution induced by including the sting representation is shown in figure 13. The calculated wall centerline pressures are shown for the Pathfinder I model at  $M = 0.80$  and  $\alpha = 2.70^\circ$ . The sting has a greater influence on the sidewall and floor distributions than on the ceiling distribution for this lifting case. In a lifting configuration, inflow exists from the plenum through the ceiling slots in the region aft of the wing, which may account for the small effect of the sting on the ceiling. The presence of the sting diminishes the flow velocity over the aft portion of the model region, as indicated by the more positive values of  $C_p$  on the sidewall and floor. This increase in  $C_p$  improves the agreement with measured values on both the sidewall and the floor. As the sting diameter increases downstream of the model, a corresponding acceleration of the flow is predicted on each wall. This negative  $C_p$  gradient also appears

to improve the agreement with experiment, although the measured values near station 18 and beyond may be erroneous due to the tare, as discussed above. The calculated  $C_L$  is 0.5601 without the sting and 0.5608 with the sting included, which shows that the sting has little influence on model lift.

The effect of varying the outflow-plane value of  $\phi_{xx}$  on the wall centerline  $C_p$  values is shown in figure 14. The solution parameters are the same as in the previous case with the sting included. Variation of  $\phi_{xx}$  has no influence upstream of tunnel station 15. For this lifting case,  $\phi_{xx}$  has the largest effect on the solid sidewall and the least effect on the ceiling pressures. The small positive value of  $\phi_{xx}$ , which corresponds to a uniform acceleration of the flow at the outflow plane, tends to improve the agreement with experiment (given the expected exceptions near the outflow plane). This variation in  $\phi_{xx}$  causes no change in the calculated model force and moment coefficients.

**Effect of slot viscous modeling parameters.** The effects of the viscous modeling parameters in the slot flow model, as implemented in reference 12, are now illustrated. The viscous parameters  $\eta_u$  and  $\eta_a$  (eqs. (9) and (10)) had values of 1 in the previous solutions presented here, which corresponds to a condition of no viscous losses through the slots. The result of independently varying the two parameters is shown by considering the wall centerline pressures in figure 15. The solutions are again calculated for the Pathfinder I model at  $M = 0.80$  and  $\alpha = 2.70^\circ$ , with  $\delta = -0.004$  and the sting representation included. Following reference 12, 30-percent reductions in the viscous parameters are used. Reducing the slot width has a larger effect than reducing the longitudinal velocity at the slot entrance. Reducing  $\eta_a$  increases the flow deceleration ahead of the model, as indicated on each of the walls. The increase in  $C_p$  continues over the entire length of the floor, and increased values also result aft of the wing (tunnel station 13) on the sidewall. The conclusion is that reducing the slot width makes the test section appear more closed, primarily in regions of slot outflow. Conversely, reducing  $\eta_u$  results in a decreased flow acceleration upstream of the model and a decrease in the suction peak above the wing. Reducing  $\eta_u$  has almost no effect on the flow at the sidewall. On the ceiling, the result is a leveling of the pressure distribution (bringing the peak values closer to the reference value), as expected from consideration of the small disturbance expression for pressure coefficient.

The effect of a simultaneous 30-percent reduction in the two viscous parameters is shown in figure 16.

All other solution parameters are the same as in the previous case. Figure 16(a) shows a comparison of the calculated and measured wall  $C_p$  values for all three rows of ceiling pressure orifices. In general, the simulation of slot viscous effects improves the comparison with experiment by increasing the flow deceleration upstream of the model and by moving the location of the model-induced flow acceleration slightly farther downstream. However, including the viscous effects also decreases the magnitude of the suction peak in the wing region, which worsens the comparison with experiment. In figure 16(b), the results for the three rows of floor orifices are shown. The overall increase in  $C_p$  due to the slot viscous parameters results in worse agreement with the measured pressures. Without viscous effects, very good agreement exists except in the vicinity of stations 9-11, which is the region just ahead of the model. The results for the three rows of sidewall orifices are shown in figure 16(c). The increase in  $C_p$  due to viscous losses results in good agreement with the measured pressures along each of the orifice rows. The largest discrepancies are in the aft portion of the sting region, where the tared pressures are most likely to have incorrect values.

### Modifications to Slot Model

On examination of the wall pressure coefficients presented so far, discrepancies between calculated and measured values are consistently observed in two regions. One area is on the ceiling aft of the wing-induced suction peak (tunnel station 13), and the other region is immediately upstream of the model location on both the floor and ceiling (near tunnel station 10). As a result of these observations, attempts were made to improve the simulation in these locations.

The ceiling region downstream of a lifting wing is the only region where strong inflow from the plenum through the slots occurs. Because the actual plenum is essentially quiescent, this inflow from the plenum has a low momentum in comparison with the flow that enters the slots from the test section. In light of these considerations, the slot crossflow momentum equation was modified. When there is inflow from the plenum the quadratic term that appears in the momentum equation is neglected. The effect of excluding the quadratic term under slot inflow conditions is shown by examining the ceiling  $C_p$  values in figure 17. Only a slight improvement is seen in the inflow region, and the effect diminishes with increasing distance from the centerline. Several additional tentative explanations exist for the discrepancies seen in this region. One possibility is that the slot flow

model does not accurately simulate the physics of slot inflow regions due to either the entrance of a significant mass of low-energy plenum air into the test section or additional viscous effects within the slots. Another possibility is the behavior of the wind tunnel wall boundary layer in this region, where the adverse pressure gradient may cause the local wall boundary layer to thicken or even separate. Other causes may be the inability of the code to treat the blockage resulting from the model wake or flow separation from the aircraft and sting at angle of attack.

Slot viscous effects may also contribute to the discrepancies seen in the region just upstream of the model location. An inflection that is not present in the measured pressures appears in the calculated floor and ceiling pressures between tunnel stations 9 and 11; for example, refer to figures 16(a) and 16(b). Examination of figure 10 shows that the effect becomes more pronounced as the slot depth is increased. As shown in table 1, the slots narrow to a minimum width at station 8.8, then gradually reopen to reach a constant width by station 10.6. Although the viscous factor  $\eta_a$  allows for a constant reduction in slot width as implemented, viscous effects are likely to be more complicated in this slot-width inflection region. The boundary layer on the slot walls may thicken or separate as the slot reopens, or a vortex may develop in the slot as it reopens. One result of these postulated models would be an effectively delayed reopening of the slot. As a simple means of examining such effects, two modified slot shapes were used in the test section simulation. The half-widths of the NTF slots as designed and of the two modified slots are shown in figure 18 (with greatly magnified half-widths). In the first modification the reopening is delayed, then occurs more gradually. The second modification is similar, but the minimum width is narrowed further. The effect of these slot shape modifications on the wall centerline  $C_p$  values is illustrated in figure 19. For these calculations,  $\eta_a$  and  $\eta_u$  both have values of 1. Modification 1 succeeds in removing the inflection between stations 9 and 11 on the floor and ceiling, and good agreement with the measured pressures exists at all other locations. Additionally, modification 2 improves prediction of the deceleration near station 10. Although the results of these modifications are encouraging, they offer little insight into the actual flow physics in such regions. The effects of these slot modifications are examined further in the next section.

### Simulation Performance

In this section, the parameters of the simulation are adjusted to give the best possible agreement

with the experiment. The Pathfinder I and Boeing 767 models are considered at both zero lift and cruise lift, and the comparisons are carried out at a Mach number of 0.80 to approximate the cruise conditions of the aircraft. At the higher lift coefficients ( $C_L > 0.5$ ), significant regions of supersonic flow exist at this Mach number. The experimental data with the Pathfinder I model were obtained at  $R = 4.0 \times 10^6$  per foot, and the Boeing 767 data were obtained at  $R = 7.5 \times 10^6$  per foot. Although almost a factor-of-2 difference exists, both values are low with respect to full-scale flight values and to the NTF operating envelope. The same tare data, obtained at  $M = 0.80$  and  $R = 6.1 \times 10^6$  per foot, are applied to each set of measured wall pressure data.

**Pathfinder I.** The case that has been used for illustration so far, the Pathfinder I model at cruise lift, is considered first. These calculations are performed with  $M = 0.80$ , outflow  $\phi_{xx} = 0.0001$ , and the sting representation included. The slot parameters are  $\delta = -0.004$ , Slot depth = 0.75 in., and Slot strip width = 7 in. Slot shape modification 1 is used unless otherwise noted. With an angle of attack of  $2.70^\circ$ , as used in the previous cases, the calculated model  $C_L$  is 0.562. To match the experimental value of 0.514, an angle of attack of  $2.30^\circ$  is used here. The wall centerline pressure coefficients resulting from these two angles of attack are compared in figure 20. Slight differences are seen through the model region, and the most significant effect is a change in the  $C_p$  level on the floor. An angle of attack of  $2.30^\circ$  is used for all other calculations shown for this case. Figure 21 shows the result of including slot viscous losses with 15-percent reductions for both  $\eta_a$  and  $\eta_u$ . Very good agreement with experiment is seen. The inclusion of viscous effects improves the prediction of the suction peak in the model region on both the sidewall and ceiling. However, the pressures on the floor are in better agreement with no viscous losses. This observation raises the possibility that the effects of viscosity on the slot flow vary, depending on the local condition of inflow or outflow—above or below a lifting wing, for example. Including the viscous losses causes the calculated  $C_L$  to increase from 0.5145 to 0.5152,  $C_M$  to change from  $-0.1515$  to  $-0.1511$ , and  $C_D$  to increase by 0.0002. These increments are quite small. The solution illustrated in figure 21, where  $\eta_a = \eta_u = 0.85$ , is considered the best overall prediction for the current case.

A more detailed examination of the effects of the slot width modifications is informative. In figure 22, the wall pressures from all nine rows of pressure orifices are shown. Results are shown for the actual slot geometry as well as for both modified slot shapes, and

each calculation is performed with  $\eta_a = \eta_u = 0.85$ . The case with slot modification 1 is the same as that presented in figure 21. Examination of the ceiling pressures (fig. 22(a)) shows that on the wall centerline the modified slot shapes give better agreement with experiment between stations 7 and 11, and modification 2 results in the best agreement. On the other two rows, the actual slot shape and modification 1 tend to give better agreement in this region. Although part of the uncertainty is due to the scarcity of data in the region, the values on the centerline may differ for another reason. In this region, the flow is decelerating due to the blockage imposed by the aircraft model, and the blockage induced by the fuselage should influence the pressure along the wall centerline more than at the outer locations. Since the fuselage begins at station 10.7, it is probable that the blockage induced by the fuselage is not properly captured by the small disturbance numerical formulation. The three floor pressure rows are shown in figure 22(b), and the solutions with slot modifications 1 and 2 are both adequate. Along the three sidewall pressure rows (fig. 22(c)), good agreement with experiment is seen when modification 1 is used. Overall, consideration of data from all the orifice rows instead of just the wall centerline rows is clearly helpful when making comparisons between measured and computed values. This approach allows spanwise and vertical variations to be considered and allows scarcity of data in some regions to be overcome. Finally, note that the slot modifications have no effect on the previously discussed discrepancies on the ceiling aft of the suction peak (fig. 22(a)).

The Pathfinder I model at zero lift is considered next. All the slot model parameters have the same values that resulted in the best agreement with experiment in the cruise-lift case. The calculated wall  $C_p$  values at an angle of attack of  $-2.0^\circ$  are compared with measured values in figure 23. Calculations are shown with both the design slot shape and slot modification 1. The slot width modification has a pronounced effect on the calculated pressures throughout the model region, which results in an improved agreement with measured values that is similar to the agreement shown in the lifting case. The calculated lift coefficients are 0.0001 with the design slot and 0.0021 with the modified slot, while the  $C_L$  corresponding to the measured pressures is 0.011. Comparison of figure 23(a) with 23(b) shows that the calculated ceiling and floor distributions are almost identical, as expected from a zero-lift calculation. The measured floor pressures, however, exhibit a slightly higher suction through the model region than the ceiling pressures exhibit. Such behavior

would be expected if the model were generating a slight negative lift, but the measured  $C_L$  is positive. This discrepancy is a result of the taring of the pressure data because empty-tunnel gradients are subtracted as part of the tare. Also, the asymmetry in the measured pressures may be partially due to the influence of the horizontal stabilizer, which is not modeled in the calculation. Excellent agreement between measured and calculated values exists along the ceiling pressure rows with the modified slot shape (fig. 23(a)), but on the floor the low pressure through the model region is underpredicted (fig. 23(b)). Figure 23(c) shows excellent agreement in the sidewall pressures with the modified slot shape, with the expected exception of those pressures near the outflow plane. The proper prediction of the  $C_p$  on the solid sidewall is an indication that the openness ratio of the slotted walls that exists experimentally is properly simulated in the calculation.

**Boeing 767.** The Boeing 767 model at zero lift is considered next. The 767 model is slightly larger than the Pathfinder I model and has a fuselage extending from tunnel station 10.8 to station 15.4. The values of the slot model parameters used here are the same as those that give the best predictions with the Pathfinder I model. A higher value of  $\phi_{xx}$  in the outflow plane is necessary for the Boeing 767 model due to the different sting arrangement. A value of 0.0003 was found to give the best behavior and is used for the results shown here. Figure 24 shows the wall pressures that result from calculations performed both with and without slot-width modification 1. Calculated  $C_L$  values are 0.0045 with the design slot and 0.0071 with the modified slot, while the measured  $C_L$  is 0.028 for this case. On the ceiling, figure 24(a) shows that the solution with the unmodified slot shape gives good agreement with the measured pressures. Again, the largest discrepancy is on the centerline at stations 8 and 9. Both solutions tend to overpredict the negative pressures existing through the model region. Ahead of the model, the comparison on the floor is similar to that on the ceiling (fig. 24(b)). Through the model region the solutions with the two different slot shapes bracket the measured values, while in the sting region the  $C_p$  values are underpredicted though the trends are correct. Comparison of figure 24(a) with 24(b) shows that the calculated pressures again are similar on the floor and ceiling, while the measured pressures show a slight asymmetry through the model region and a significant asymmetry through the sting region. In the sting region, these observations are consistent because the Boeing 767 sting is located above the fuselage (fig. 4(b)), whereas in the code the fuselage

and sting are located on the same axis. The sidewall pressures (fig. 24(c)) support the observations made on the ceiling and floor, which include the overprediction of the pressures in the model region in the upper half of the test section, the underprediction in the lower half, and the asymmetry in the sting region. As in the case of the Pathfinder I model near zero lift, the measured pressures in the model region have a characteristic that would result from the model generating a slight negative lift: higher acceleration is found on the floor than on the ceiling. Because the measured lift is actually a positive value, the discrepancy between measured floor and ceiling pressures is again attributed to the tare subtraction. The current solution with the design slot shape gives good overall agreement with the measured pressures, but these comments indicate that improved agreement with the measured pressures might be achieved by decreasing the angle of attack in the calculation. Such a change is analogous to correction for tunnel-empty flow angularity. Figure 25 shows the effect of lowering the angle of attack by  $0.3^\circ$ . The calculated  $C_L$  is  $-0.0328$  at this angle of attack. Improved agreement with the measured pressures through the model region appears along all the orifice rows.

Finally, consider the Boeing 767 model at cruise conditions. The wall centerline  $C_p$  values resulting from a solution at an angle of attack of  $2.15^\circ$  with the design slot shape and the same values of the slot model parameters used in the previous cases are compared with measured values in figure 26. The calculation predicts an incorrect location for the beginning of the suction peak above the model and for the recompression aft of the model on the sidewall. The  $C_p$  level on the floor in the model region is underpredicted. These types of behavior are improved by lowering the plenum pressure coefficient. The effect of decreasing  $\delta$  to  $-0.005$  while all other slot parameters remain unchanged is shown in figure 27. Figure 27 also shows the effect of including slot modification 1. The calculated  $C_L = 0.5464$  with the design slot and  $0.5479$  with slot modification 1, and the measured  $C_L = 0.548$ . On the ceiling (fig. 27(a)), the solution with the unmodified slot shape gives good agreement with measured values up to the suction peak over the wing. The disagreement downstream of the suction peak is largest on the centerline and diminishes toward the sidewall. Given this spanwise variation, much of the discrepancy is attributable to improper simulation of the high-mounted sting (including sting/fuselage interference and wake/separation effects). The behavior near tunnel station 10 is similar to that observed in the previous cases. The design slot shape also gives

good results on the floor pressure rows, as shown in figure 27(b). Again, the largest disagreement is found near station 10. Very good agreement between measured and calculated  $C_p$  values exists on the sidewall when the unmodified slot shape is used (fig. 27(c)).

**Discussion of results.** The goal of the current work is to derive a treatment of the slotted-wall flow field that allows consistent prediction of the test section flow. Because of the many parameters in the current slotted-wall model, a proper combination is difficult to select. A combination of parameter values is developed here that gives reasonably good predictions for two models at lifting and nonlifting conditions (although in the final case the simulation is improved by further lowering the plenum pressure). These results are encouraging, but some additional issues are identified.

The results of the slot width modification shown here indicate that a delayed reopening of the slots downstream of their minimum in width, such as might result from the effects of viscosity, improves the agreement with measured wall  $C_p$  values. With the Pathfinder I data, the slot modification tends to properly compensate the calculation in this region. With the Boeing 767 data, the discrepancy is smaller, and the same slot modification appears to over-compensate in this region. Although no mechanisms for the width reduction have been identified, the simple approach taken here shows that the effect is independent of lift. The behavior is tentatively attributed to the test section wall boundary layers and/or to viscous effects in the slots. Because the Reynolds number is lower in the Pathfinder I data than in the Boeing 767 data, larger viscous effects in the slots can be expected with the Pathfinder I data. The effects of viscosity on the walls and in the slots are further clouded by the subtraction of tunnel-empty wall  $C_p$  values as a tare.

The subtraction of tares from the measured wall pressures exposes concerns that pertain to wall interference corrections. As evident from the zero-lift comparisons, an offset between the measured and calculated  $C_L$  values results when the calculated wall  $C_p$  values are brought into agreement with the tared, measured values. This tare-induced offset is indicative of global flow angularity and Mach number offsets that are discarded with the tare. Such offsets would have to be considered, perhaps through analysis of the actual tunnel-empty wall pressure data, before attempting to use the code results to calculate any actual corrections to wind tunnel data.

The outflow-plane  $\phi_{xx}$  specification in the current method is intended to mimic the gross  $C_p$  trends near the reentry region. It is apparent from the wall  $C_p$  results that this approach gives reasonable results with the Pathfinder I sting arrangement but less accurate results with the high-mounted sting of the Boeing 767. Although the calculated model coefficients seem insensitive to the outflow specification, they may be affected by proper sting representation because the sting can appreciably influence the flow gradients in the aft part of the model region.

Finally, the current results must be viewed in the proper context. The simulation method is capable of reproducing the wall pressure signature that exists in the NTF test section. An implicit assumption is that the effect of the walls on the model flow field is similarly predicted. Although a relationship between the wall effects and the model flow field certainly exists, this assumption remains unproven due to the lack of appropriate experimental data from the model surface. In the following section, the calculated effect of the test section on the model flow field is shown.

### Wall Interference Illustration

The effect of the test section on the aircraft flow field is shown by comparing the results of free-air and test section calculations with the Pathfinder I model at  $M = 0.80$  and an angle of attack of  $2.70^\circ$ . Test section simulations are performed with the sting included and slot shape modification 1 used for both discrete and homogeneous slotted-wall boundaries. The discrete slotted-wall parameters have the optimum values that were developed in the previous section. Table 3 lists the calculated force and moment coefficients and shows that the homogeneous calculation gives results that are almost identical to the free-air values. The discrete slotted-wall calculation shows an underprediction of the lift by 0.7 percent, of the pitching moment by 1.5 percent, and of the drag by 7.7 percent in comparison with the free-air calculation.

Local variations induced by the test section are examined by considering the wing pressure distribution. For the free-air and discrete slotted-wall calculations, pressure distributions at wing semispan locations of 21 percent, 52 percent, and 82 percent are shown in figure 28. These comparisons show that the shock locations predicted by the two calculations differ by less than 1 percent of the chord at each spanwise location. The test section calculation shows a greater upper surface expansion at the inboard and midspan locations (figs. 28(a) and 28(b)), which indicates the existence of slightly stronger shock waves. The outboard station shows the only

substantial difference between the lower surface pressures (fig. 28(c)), which probably illustrates a flow angularity effect. Although small, the differences shown here are likely to increase with models larger than the Pathfinder I. The calculated wing pressure coefficients with free-air and homogeneous slotted boundaries are identical; the 52-percent semispan location shown in figure 29 is an example.

As shown in the preceding sections, good agreement with measured wall pressures is obtained by using negative plenum pressure coefficients in the discrete-slot model. Reference 15 shows that the discrete-slot model with  $\delta = 0$  gives results very similar to those obtained using the homogeneous slotted boundary. (Also, compare figs. 5 and 7(a).) Thus, a more accurate portrayal of wall interference effects is probably given by the current discrete slotted-wall calculation.

### Concluding Remarks

A computational method was developed that is capable of simulating the flow in a transonic test section with longitudinally slotted walls. The slotted walls may be modeled either with discrete slots or in the classical homogeneous manner. The simulation results were compared with measured wall pressure data to judge the performance of the method at the walls. For the aircraft model geometries and limited available data shown here, the discrete-slot method was found to give consistently good results with minimal variation of the parameters that appeared in the slot flow model. The value of the plenum pressure coefficient was one of these parameters, and negative values (on the order of  $-0.01$ ) were required to yield proper behavior. Because the classical homogeneous formulation does not have a means to vary plenum pressure, this technique was incapable of properly predicting the measured wall pressures.

The simulation method may be used to predict the influence of the test section environment on the aircraft flow field. These predictions are made by performing both free-air and test section calculations,

then examining the incremental differences between the two solutions. Such increments may then be considered in conjunction with data measured during a wind tunnel test. These increments cannot be used as wall interference corrections at present due to the flow angularity uncertainties that arise from the subtraction of tunnel-empty wall pressures as a tare. However, the simulation can give indications of the variations expected in force and moment coefficients as well as in measured model pressure distributions.

Additional wall pressure data are needed to evaluate the simulation method more thoroughly. Data obtained with simple wing/fuselage model configurations at high Reynolds numbers would be particularly useful. The Reynolds numbers of the data sets used here are on the low end of the NTF operating envelope, and how the simulation will perform or how the slot model parameters might need to be changed when confronted with high Reynolds number data (up to an order of magnitude larger than considered here) is not known. Some localized disagreement between the measured and calculated wall pressure coefficients is currently noted that may result from improper modeling of slot and/or wall viscous effects. Because these viscous issues are complicated by the subtraction of tunnel-empty tare pressures, a clearer determination requires examination of data at higher Reynolds numbers.

The ultimate intent is to use the current method as a pretest indicator, showing whether wall interference is a concern for a given model and flow condition. The ability of the method to simulate the flow at the test section walls has been shown here. Due to the model sizes, very little wall interference exists with the models considered here. Thus, the usefulness of the method to predict wall interference effects on the model requires validation with data that do not currently exist.

NASA Langley Research Center  
Hampton, VA 23681-0001  
June 10, 1993

## Appendix A

### Solution of Centerplane Slot Flow Equations

The integration of the two slot flow equations is not a straightforward procedure due to the complexity of the expressions. In the auxiliary equations, the variables of interest cannot be isolated in a closed form. For convenience, the centerplane slot equations (eqs. (4), (6), (18), (19), and (20)) are summarized and repeated as follows:

$$\frac{dy_p}{dx} = \frac{q_s V}{a_s} - E \frac{y_p}{a_s} \frac{da_s}{dx} \quad (\text{A1})$$

$$\begin{aligned} \frac{d(\varphi - \varphi_o)}{dx} + \frac{\rho_s}{\rho_\infty} \frac{U_s}{U_\infty} \frac{d}{dx} \left( \frac{U_s}{U_\infty} \left\{ q_s Q \right. \right. \\ \left. \left. - \frac{q_s}{\pi} \left[ \frac{1}{2} + \ln \left( 4 \frac{a_s}{b} \right) \right] - \frac{y_p^2}{a_s} \frac{da_s}{dx} \frac{E}{2} \right\} \right) \\ = -\frac{1}{2} \frac{\rho_s}{\rho_\infty} \left( \frac{U_s}{U_\infty} \right)^2 \left( \frac{q_s V}{a_s} - E \frac{y_p}{a_s} \frac{da_s}{dx} \right)^2 - \delta \quad (\text{A2}) \end{aligned}$$

$$Q = -\sigma \ln s \quad (\text{A3})$$

$$V = \frac{\sigma}{\sqrt{s^2 + \sigma^2}} \quad (\text{A4})$$

$$\frac{y_p}{a_s} = - \left[ \sqrt{s^2 + \sigma^2} + \sigma \ln \left( \frac{\sqrt{s^2 + \sigma^2} - \sigma}{s} \right) \right] \quad (\text{A5})$$

The goal is to simultaneously integrate equations (A1) and (A2) along the slot, given an estimate of  $q_s$ . However, the auxiliary relations given by equations (A3) and (A4) are necessary to define the terms  $Q$  and  $V$ . These relations are expressed in terms of the transform variable  $s$ , while the differential equations are in terms of the variable  $y_p$ . Equation (A5) gives the relationship between  $y_p$  and  $s$ , but  $s$  cannot be isolated in this expression. An iterative process is necessary to calculate  $s$ , given  $y_p$ . An alternate approach is to rewrite equations (A1) and (A2) in terms of  $s$ . This approach is simple

for equation (A2) and requires only direct substitution of equations (A3), (A4), and (A5). To rewrite equation (A1), however,  $dy_p/dx$  must be replaced by  $ds/dx$ . A derivation of this relation is now presented.

Noting that equation (A5) expresses  $y_p/a_s$  as a function of  $s$ , it is convenient to write the simple expression

$$\frac{d}{dx} (y_p) = \frac{d}{dx} \left( \frac{y_p}{a_s} a_s \right) = a_s \frac{d}{dx} \left( \frac{y_p}{a_s} \right) + \frac{y_p}{a_s} \frac{da_s}{dx} \quad (\text{A6})$$

Using equation (A5) it can be shown that

$$\frac{d}{dx} \left( \frac{y_p}{a_s} \right) = -\frac{\sqrt{s^2 + \sigma^2}}{s} \frac{ds}{dx} \quad (\text{A7})$$

and substitution of equation (A7) into equation (A6) yields the relation

$$\frac{dy_p}{dx} = -\frac{a_s}{s} \sqrt{s^2 + \sigma^2} \frac{ds}{dx} + \frac{y_p}{a_s} \frac{da_s}{dx} \quad (\text{A8})$$

Equation (A8) is the desired relation between  $dy_p/dx$  and  $ds/dx$ . Substituting equation (A8) into equation (A1) and rearranging yields

$$\frac{ds}{dx} = -\frac{s}{a_s} \frac{1}{\sqrt{s^2 + \sigma^2}} \left( \frac{q_s V}{a_s} - (1 + E) \frac{y_p}{a_s} \frac{da_s}{dx} \right) \quad (\text{A9})$$

All terms in equation (A9) are either known functions of the independent variable  $x$  or explicit functions of the dependent variable  $s$ . Finally, recall that equation (5) defines the location of the limiting value for  $y_p$ , denoted by  $y_{p,o}$ . Because the variable of integration is now  $s$  instead of  $y_p$ , equation (A7) is used to obtain the value of  $s$  that corresponds to  $y_{p,o}$ . Let this limiting value of  $s$  be denoted by  $s_{p,o}$ . During the integration of equations (A9) and (A2),  $s$  must be reset to the value  $s_{p,o}$  whenever the projected value of  $s$  would exceed that allowed by  $s_{p,o}$ .

To summarize, the differential equation for  $dy_p/dx$  has been replaced by an equivalent differential equation for  $ds/dx$ . The result is a system of two differential equations, equations (A9) and (A2), that contain the two unknown functions  $s$  and  $\varphi$ . A simultaneous integration of the two equations along each slot yields  $s$  and  $\varphi$ .

## Appendix B

### Global Coarse Grid Generation

This section details the generation of the global finite difference grid. The physical domain described by the Cartesian coordinates  $(x, y, z)$  is related to the computational domain given by  $(\xi, \eta, \zeta)$ . The longitudinal direction is given by  $x$  and  $\xi$ , the spanwise direction by  $y$  and  $\eta$ , and the vertical direction by  $z$  and  $\zeta$ . The grid spacing in each coordinate direction is constant in the computational domain, which greatly simplifies the finite-difference formulation. The transformations relating the two domains are simple algebraic expressions. To avoid singularities in the transformation, the transformation derivatives (metrics) to second order are smooth and continuous.

In the NTF test section, station 13 (13 ft from the beginning of the test section) is the center of sting rotation. The model wing is typically near this position. The grid in the  $x$  direction is symmetric and is centered around NTF station 13. For convenience,  $\xi$  extends from  $-1$  to  $1$ , and the corresponding  $x$  values cover negative to positive infinity. In the  $x$  direction, the physical domain is divided into five regions, with the middle region centered on station 13 (fig. B1). Because the grid is symmetric, the two zones ahead of the wing region are treated the same as the two zones downstream of the wing. The central region (zone 1) contains the wing and may be thought of as extending from the leading edge of the root to the trailing edge of the tip (for a typical swept wing). This region is slightly expanded as necessary to locate the midpoint of the region at station 13. Sixteen

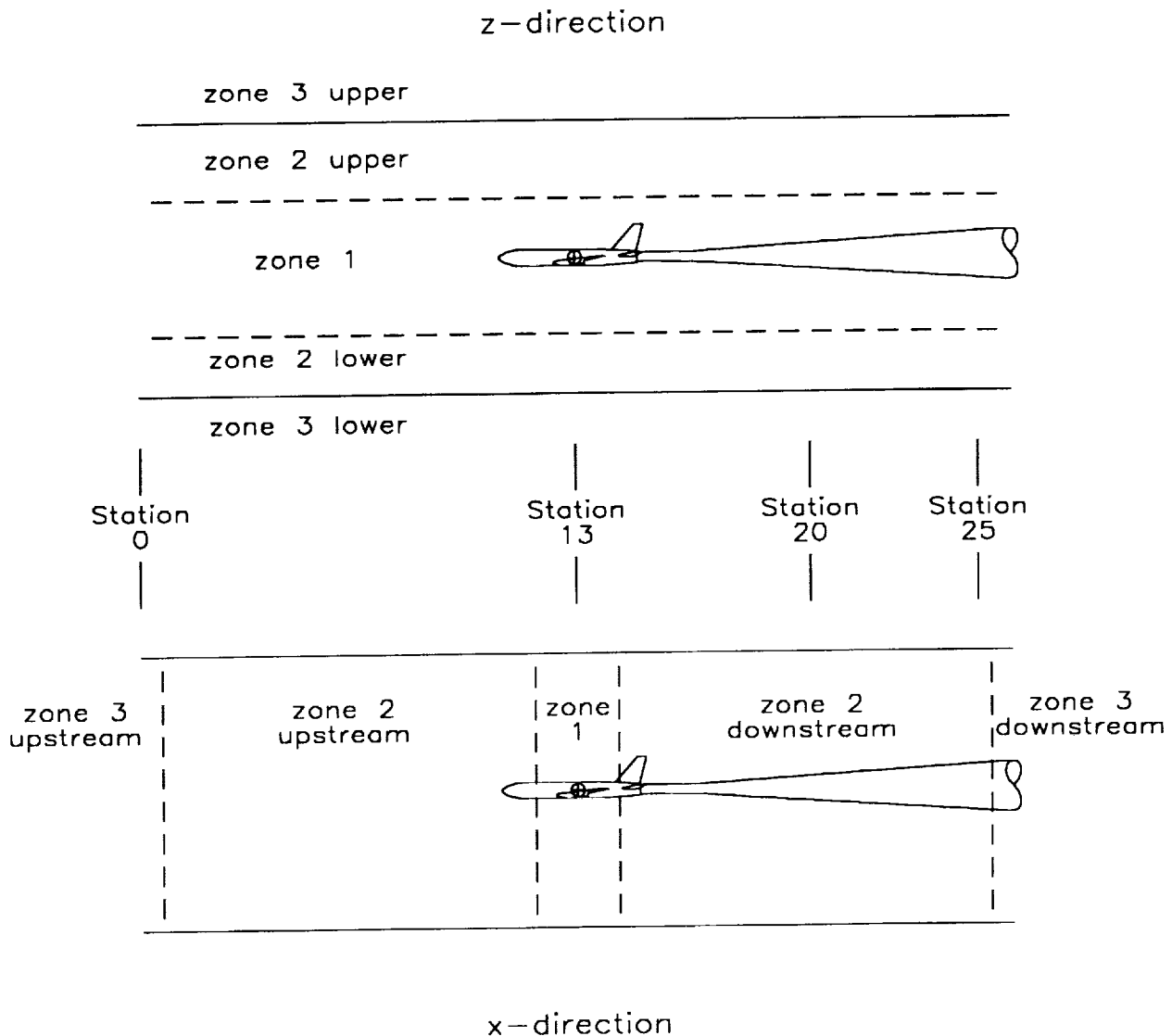


Figure B1. Zones used in grid generation in vertical ( $z$ ) and streamwise ( $x$ ) directions.

cells are uniformly distributed in zone 1. The transform is written as

$$x = A_0 + A_1\xi \quad (\text{B1})$$

Because  $\xi = 0$  at station 13 and the values of  $x$  and  $\xi$  at the edge of the wing region are known, the constants  $A_0$  and  $A_1$  are easily evaluated. The next zones cover the regions that extend from the edges of the wing zone to the test section inflow (zone 2 upstream) and outflow (zone 2 downstream) planes. (See fig. B1.) In these regions, a cubic function is used to give a mild stretching yet still maintain a reasonable spacing at the test section boundaries. The transform is given by

$$x = A_0 + A_1\xi + A_2 \left( \frac{\xi - \xi_1}{\xi_2 - \xi_1} \right)^3 \quad (\text{B2})$$

where  $\xi_1$  is the value of  $\xi$  at the edge of the wing region and  $\xi_2$  is equal to the value of  $\xi$  at infinity (that is,  $\xi_2 = -1$  upstream and  $+1$  downstream). The constant  $A_2$  is determined by the locations of the inflow and outflow planes. Note that as the edges of zone 1 are approached from these regions,  $\xi \rightarrow \xi_1$ , and equation (B2) reduces to equation (B1). Using superposition in this way ensures that the metrics are smooth and continuous at the boundaries between the regions. The grid-generation functions in both the  $x$  and  $y$  directions are built up in this manner. The final longitudinal regions, defined by zone 3, extend from the inflow plane to upstream infinity and from the outflow plane to downstream infinity. The grid-generation function in these regions is written as

$$x = A_0 + A_1\xi + A_2 \left( \frac{\xi - \xi_1}{\xi_2 - \xi_1} \right)^3 + A_3 \tan \left[ \frac{\pi}{2} \left( \frac{\xi - \xi_3}{\xi_2 - \xi_3} \right)^3 \right] \quad (\text{B3})$$

where  $\xi_3$  is the value of  $\xi$  at the test section boundary. The constant  $A_3$  is evaluated by requiring the next-to-last grid point to be located a distance  $A_0$  from the boundary (that is, one half the test section length). Note that as  $\xi$  approaches its maximum value  $\xi_2$ , the argument of the tangent function approaches  $\pi/2$ , which means that the function itself tends toward infinity.

In the spanwise direction,  $\eta$  ranges from a value of 0 at the tunnel centerline to a value of 1 at positive infinity. Constant spacing is used between the centerline and the test section wall. The spacing is chosen to align a grid plane with the slot closest to the tunnel centerline. Due to the geometry of the NTF test section, this technique ensures that grid planes are also aligned with the other two slots as well

as with the test section sidewall. The transformation equation is written as

$$y = B_1\eta \quad (\text{B4})$$

where  $B_1$  is determined by specifying the number of grid planes that lie between the centerline and the first slot. Outside the test section, the tangent function is again used to stretch the grid toward infinity. The expression is

$$y = B_1\eta + B_2 \tan \left[ \frac{\pi}{2} \left( \frac{\eta - \eta_1}{\eta_2 - \eta_1} \right)^3 \right] \quad (\text{B5})$$

where  $\eta_1$  is the value of  $\eta$  at the wall, and  $\eta_2$  is the maximum value of  $\eta$ . The constant  $B_2$  is evaluated by requiring that the next-to-last grid point is located a distance from the centerline that is equal to twice the  $y$  location of the wall.

The grid generation in the  $z$  direction is complicated by two factors. One constraint is the desire to have a grid symmetric about the wing plane. However, the wing plane may not be equidistant from the floor and ceiling. The other factor is the need to minimize the total number of grid points while maintaining adequate grid resolution near both the wing and the walls. These demands are accommodated by dividing the region inside the test section into three regions (fig. B1): a central symmetric region (zone 1), a region below the ceiling (zone 2 upper), and a region above the floor (zone 2 lower). The same transformation is used near the floor and the ceiling, but the constants in the transform equation differ if the wing plane is not centered between the floor and ceiling. The test section centerline is located at  $z = 0$ , and the wing plane is at  $\zeta = 0$ . Thus, if the wing plane is located at  $z = 0$ , then the entire vertical grid is symmetric about  $z = 0$ . The ceiling and floor are at  $\zeta$  locations of  $\pm 1$ . Zone 1 encompasses half the test section height and is centered about the wing plane. The transformation in this region is written as

$$z = z_w + C_1 \tan \left( \frac{\pi}{2} \zeta \right) \quad (\text{B6})$$

where  $z_w$  denotes the position of the wing plane. The constant  $C_1$  is evaluated by specifying the number of grid points that lie in this region. The regions defined by zone 2 extend from the edges of the central region to the floor and ceiling. The transformation is given by

$$z = z_w + C_2 \tan \left[ \frac{\pi}{2} (\zeta - \zeta_w) \right] (1 + D_1\zeta) \quad (\text{B7})$$

where the subscript  $W$  denotes the value at the wall. This transform serves to slightly refine the spacing in the vicinity of the wall. Equation (B7) has the same form as equation (B6); both are simple tangent functions, but equation (B6) is centered on the wing plane while the tangent function in equation (B7) is shifted so that the function is centered on the wall. The term containing the constant  $D_1$  is a scaling factor that can be thought of as expanding or compressing the grid in these regions. To illustrate, recall that equation (B7) applies to both the floor and ceiling regions, where the constants  $C_2$  and  $D_1$  have the same values for these regions only if the wing plane is centered between the floor and ceiling. Let the resulting grid be thought of as uncompressed. If the wing plane is located at some negative  $z$  value, then the  $(1 + D_1\zeta)$  term will serve to compress the

grid near the floor and expand the grid near the ceiling, and  $C_2$  and  $D_1$  will have different values in the two regions. Solving for the two constants requires two constraints. The constraints are that equations (B6) and (B7) have the same value and the same first derivative at the edge of zone 1. Outside the test section walls (zone 3), a tangent function is used to stretch the grid toward infinity. The transformation is written as

$$z = z_W + C_3 \tan \left[ \frac{\pi}{2} \left( \frac{\zeta - \zeta_W}{\zeta_2 - \zeta_W} \right) \right] \quad (\text{B8})$$

where  $\zeta_2$  is the value of  $\zeta$  corresponding to  $z = \infty$ . The constant  $C_3$  is evaluated by requiring the first derivatives of equations (B7) and (B8) to match at the wall.

## References

1. Igoe, William B.: Characteristics and Status of the U.S. National Transonic Facility. *Cryogenic Wind Tunnels*, AGARD-LS-111, July 1980, pp. 17-1-17-11.
2. Mokry, M.; Chan, Y. Y.; and Jones, D. J.: *Two-Dimensional Wind Tunnel Wall Interference*. AGARD-AG-281, Nov. 1983.
3. Rizk, M. H.; and Murman, E. M.: Wind Tunnel Wall Interference Corrections for Aircraft Models in the Transonic Regime. *J. Aircr.*, vol. 21, no. 1, Jan. 1984, pp. 54-61.
4. Phillips, Pamela S.; and Waggoner, Edgar G.: A Transonic Wind Tunnel Wall Interference Prediction Code. AIAA Paper 88-2538, 1988.
5. Kemp, William B., Jr.: *Computer Simulation of a Wind Tunnel Test Section With Discrete Finite-Length Wall Slots*. NASA CR-3948, 1986.
6. Keller, James D.: *Numerical Calculation of Boundary-Induced Interference in Slotted or Perforated Wind Tunnels Including Viscous Effects in Slots*. NASA TN D-6871, 1972.
7. Berndt, S. B.; and Sörensen, H.: Flow Properties of Slotted Walls for Transonic Test Sections. *Wind Tunnel Design and Testing Techniques*, AGARD-CP-174, Mar. 1976, pp. 17-1-17-11.
8. Berndt, Sune B.: Inviscid Theory of Wall Interference in Slotted Test Sections. *AIAA J.*, vol. 15, no. 9, Sept. 1977, pp. 1278-1287.
9. Karlsson, K. R.; and Sedin, Y. C.-J.: Numerical Design and Analysis of Optimal Slot Shapes for Transonic Test Sections—Axisymmetric Flows. *J. Aircr.*, vol. 18, no. 3, Mar. 1981, pp. 168-175.
10. Sedin, Y. C.-J.; and Sörensen, H.: Computed and Measured Wall Interference in a Slotted Transonic Test Section. *AIAA J.*, vol. 24, no. 3, Mar. 1986, pp. 444-450.
11. Sedin, Y. C.-J.; Agrell, N.; and Zhang, N.: Computation of Transonic Wall-Interference in Slotted-Wall Test Sections of Wind Tunnels. Paper presented at the International Symposium on Computational Fluid Dynamics (Tokyo, Japan), Sept. 9-12, 1985.
12. Agrell, N.; Pettersson, B.; and Sedin, Y. C.-J.: Numerical Design Parameter Study for Slotted Walls in Transonic Wind Tunnels. *Proceedings of the 15th ICAS Congress*, Volume 2, P. Santini and R. Staufenbiel, eds., American Inst. of Aeronautics and Astronautics, Inc., Sept. 1986, pp. 770-778. (Available as ICAS-86-1.6.2.)
13. Rosen, Bruce S.: *Method To Predict External Store Carriage Characteristics at Transonic Speeds*. NASA CR-4170, 1988.
14. Boppe, Charles W.: *Transonic Flow Field Analysis for Wing-Fuselage Configurations*. NASA CR-3243, 1980.
15. Al-Saadi, Jassim A.: Wall Interference Calculation in a Transonic Wind Tunnel With Discrete Slots. Ph.D. Dissertation, North Carolina State Univ., 1991.
16. Kemp, William B., Jr.: *Description and Evaluation of an Interference Assessment Method for a Slotted-Wall Wind Tunnel*. NASA CR-4352, 1991.
17. Newman, P. A.; Kemp, W. B., Jr.; and Garriz, J. A.: Emerging Technology for Transonic Wind-Tunnel-Wall Interference Assessment and Corrections. SAE Tech. Paper Ser. 881454, Oct. 1988.

Table 1. Ordinates Defining NTF Slot Shape

[ Ordinates given as slot half-widths ]  
 [ measured from slot centerline ]

Tunnel station, ft	Slot half-width, in.	Tunnel station, ft	Slot half-width, in.
0.604	0.000	6.776	0.518
.686	.010	7.149	.470
.754	.032	7.529	.417
.912	.100	7.923	.367
1.090	.176	8.150	.341
1.281	.257	8.314	.324
1.481	.338	8.478	.309
1.689	.413	8.642	.298
1.907	.487	8.806	.293
2.138	.552	8.970	.294
2.384	.611	9.134	.301
2.651	.663	9.298	.316
2.944	.705	9.463	.336
3.072	.720	9.627	.361
3.484	.751	9.791	.389
4.144	.757	9.954	.417
4.695	.729	10.118	.444
5.176	.691	10.282	.467
5.612	.652	10.446	.484
6.015	.612	10.611	.492
6.401	.567	19.667	.492

Table 2. Effect of Homogeneous Outer Boundary Conditions  
on Calculated Pathfinder I Force and Moment Coefficients

[ $M = 0.80$  and  $\alpha = 2.70^\circ$ ]

Boundary	$C_L$	$C_M$	$C_D$
Free air	0.5669	-0.1573	0.0183
Open jet	.5618	-.1579	.0182
Solid	.5772	-.1570	.0187
Slotted	.5659	-.1578	.0183

Table 3. Comparison of Calculated Force and Moment Coefficients  
With Outer Boundary Conditions

[ Pathfinder I at  $M = 0.80$  and  $\alpha = 2.70^\circ$ ; sting ]  
included in test section calculations

Boundary	$C_L$	$C_M$	$C_D$
Free air	0.5669	-0.1573	0.0183
Homogeneous slotted-wall	.5667	-.1566	.0184
Discrete slotted-wall	.5632	-.1549	.0169

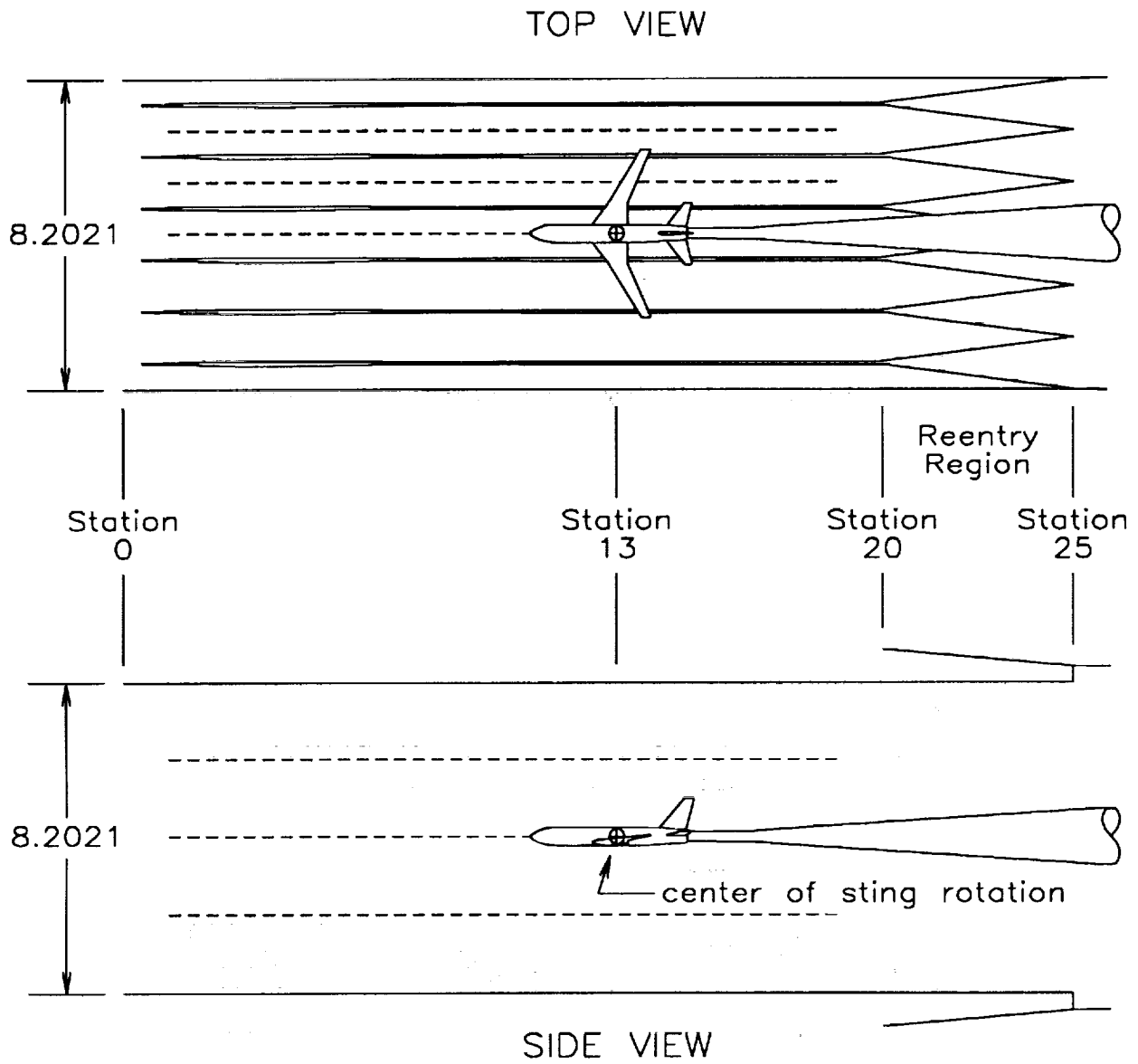


Figure 1. NTF test section. Dashed lines indicate locations of wall pressure orifice rows. All dimensions are in feet.

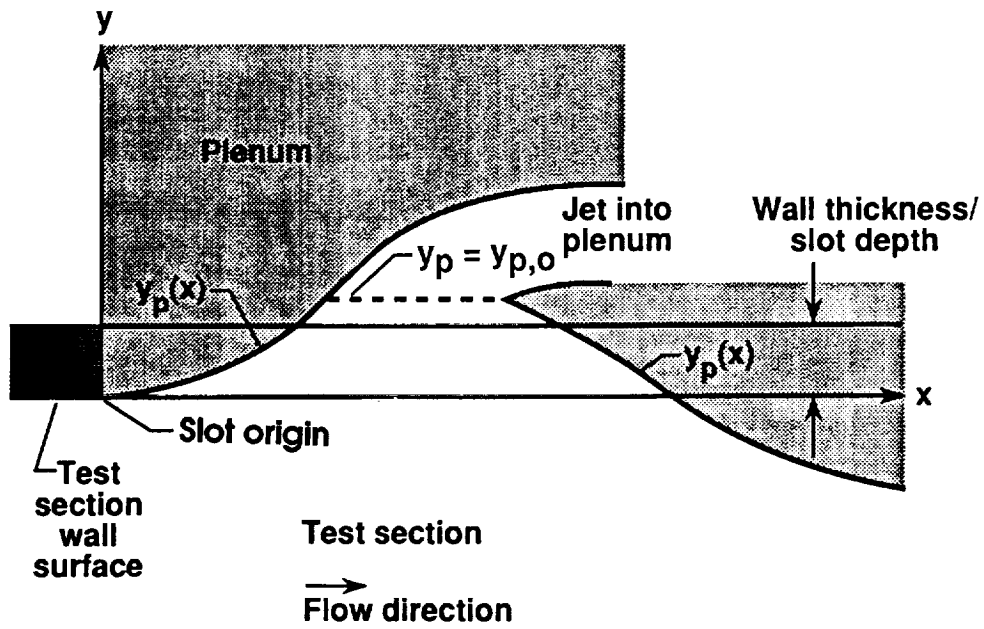


Figure 2. Slot flow model in slot centerplane.

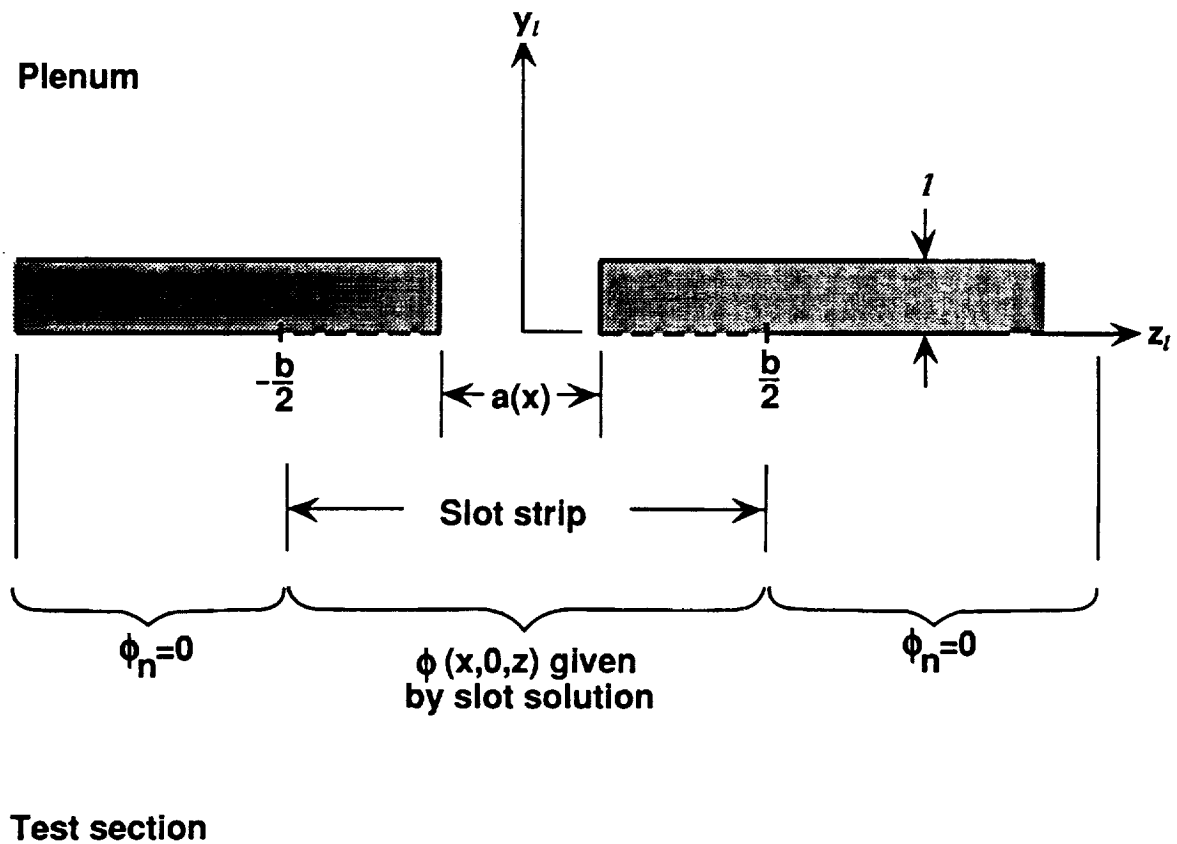
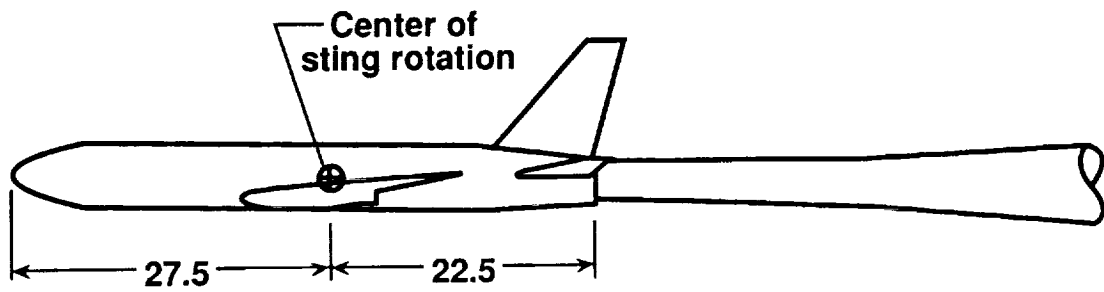
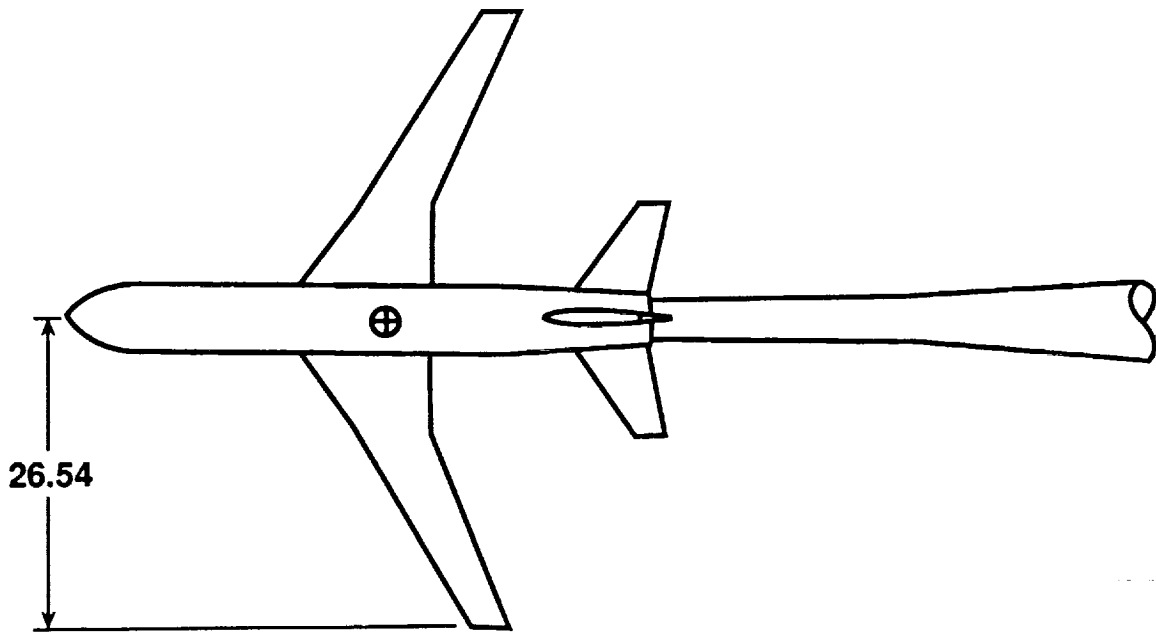
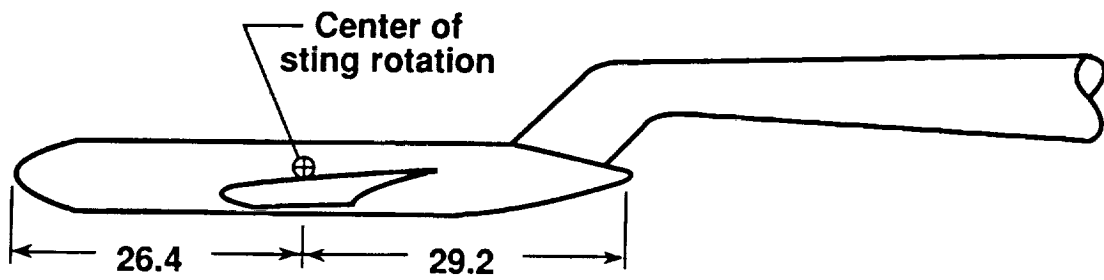
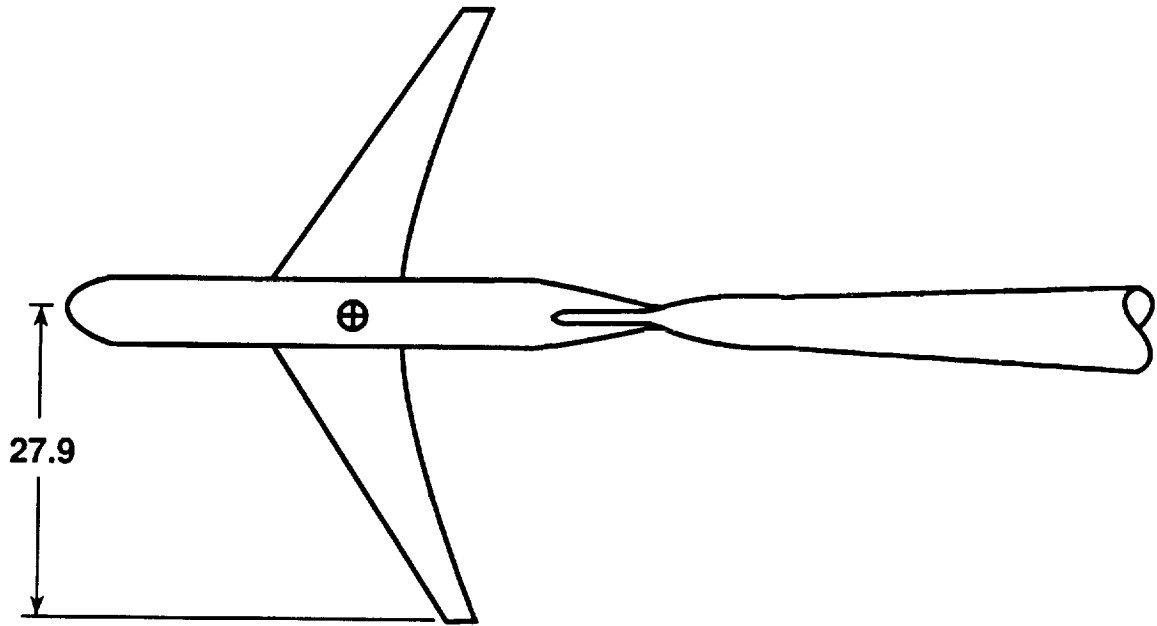


Figure 3. Cross section of slot model geometry for isolated slot showing specification of boundary conditions.



(a) Pathfinder I.

Figure 4. NTF transport models including model support stings. All dimensions are in inches.



(b) Boeing 767.

Figure 4. Concluded.

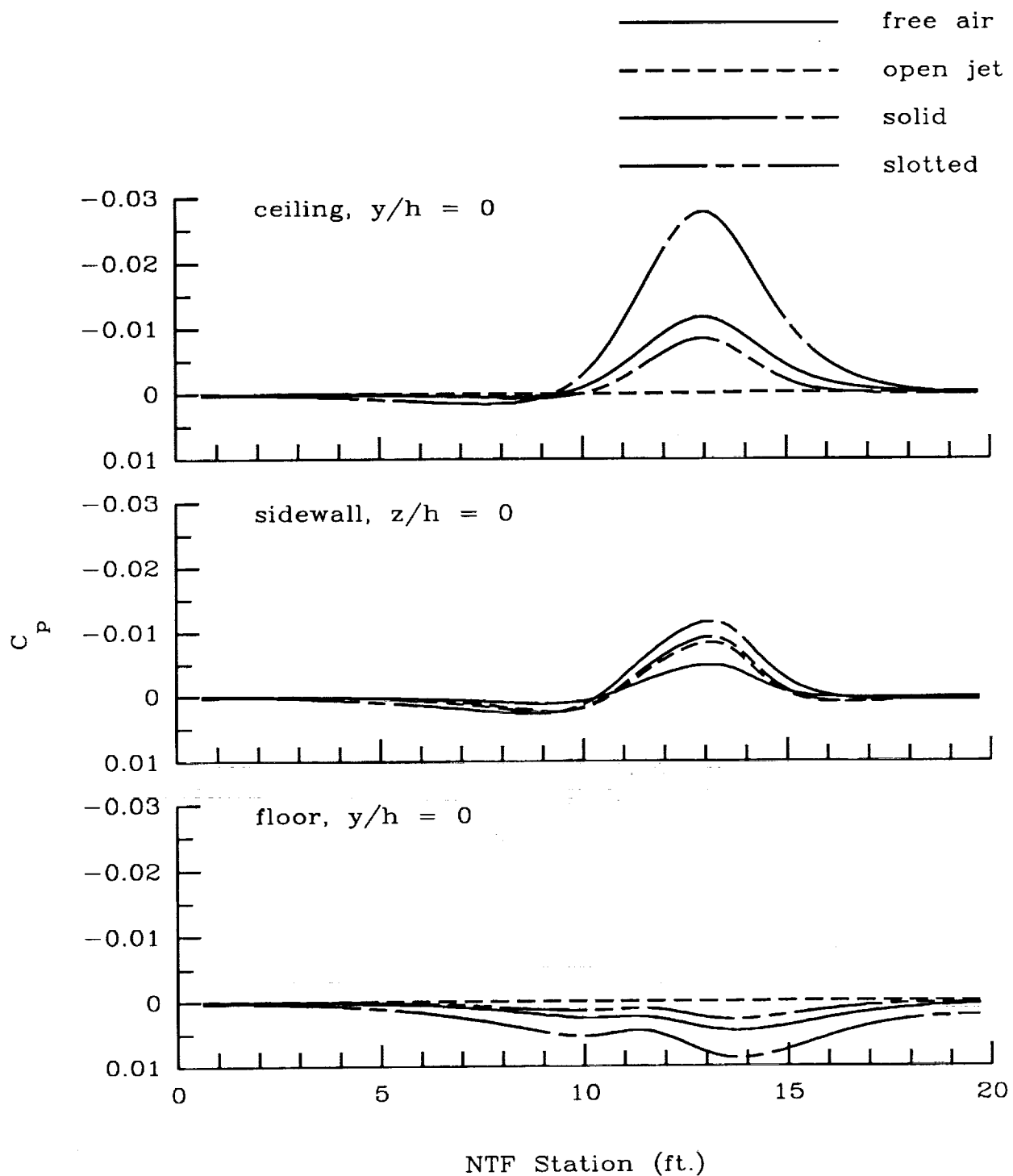
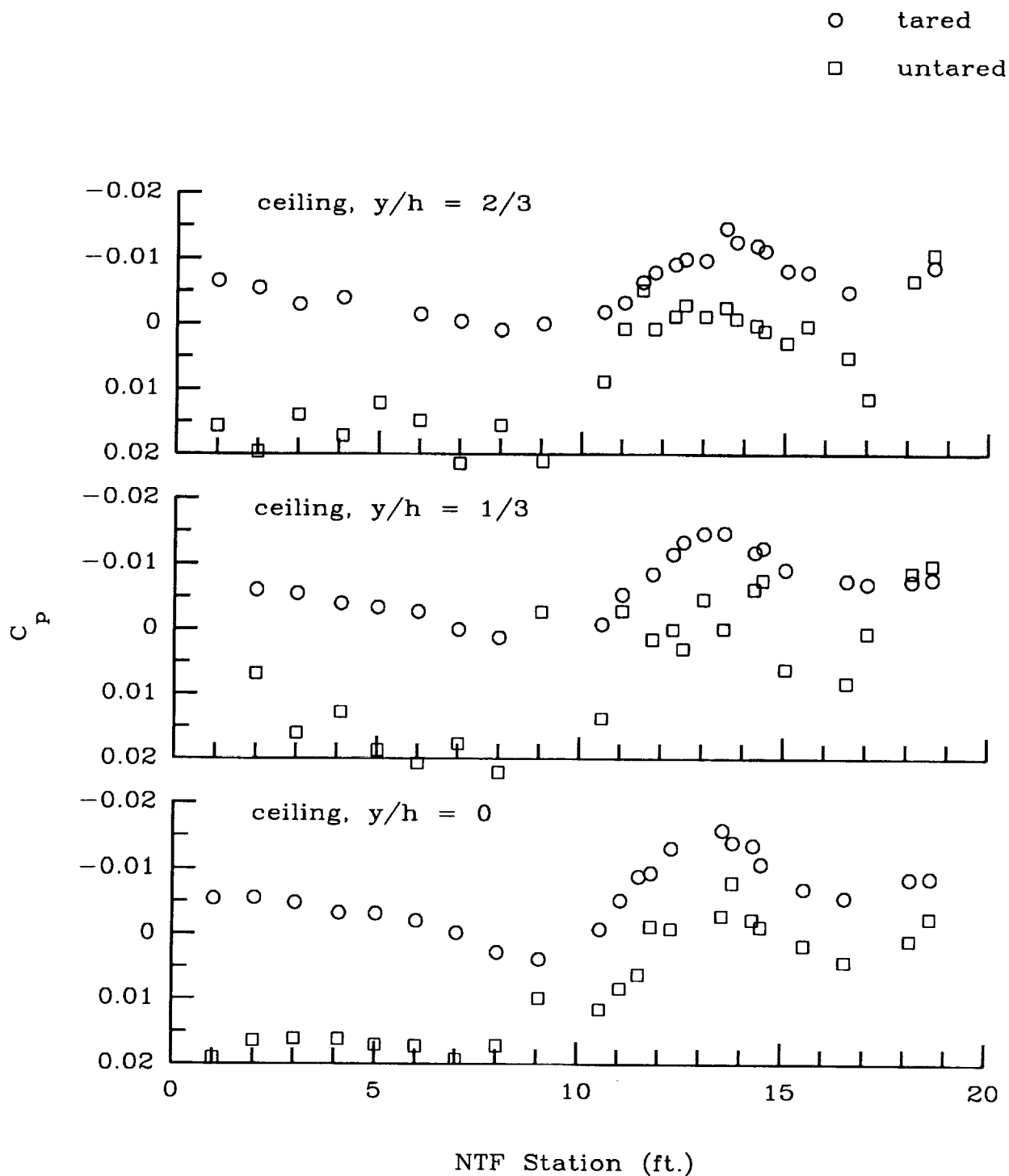


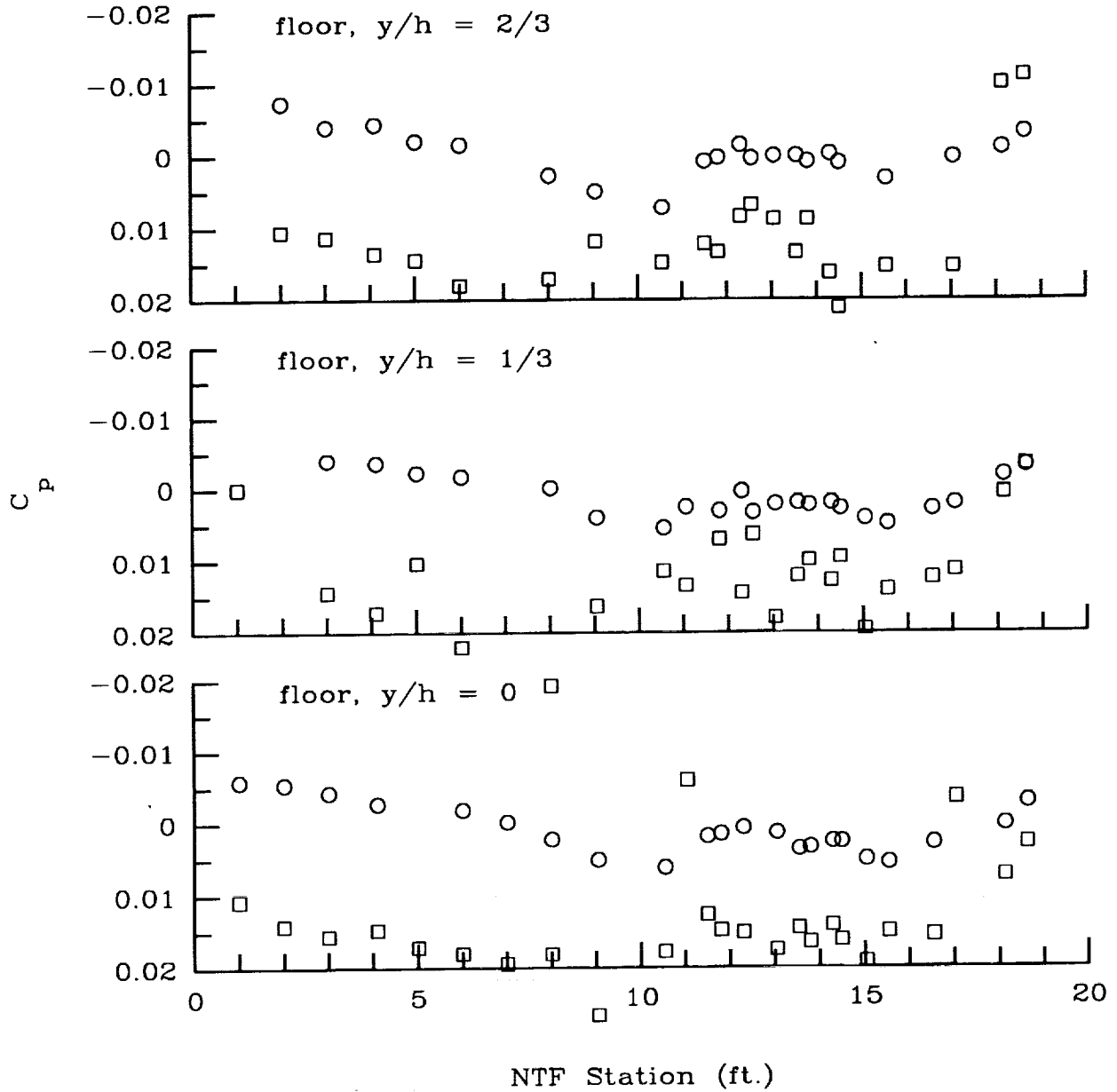
Figure 5. Calculated pressure coefficients on centerline of test section walls with different classical homogeneous outer boundary conditions applied to top and bottom walls (sidewall is always treated as solid). Pathfinder I at  $M = 0.80$  and  $\alpha = 2.70^\circ$ .



(a) Ceiling orifice rows.

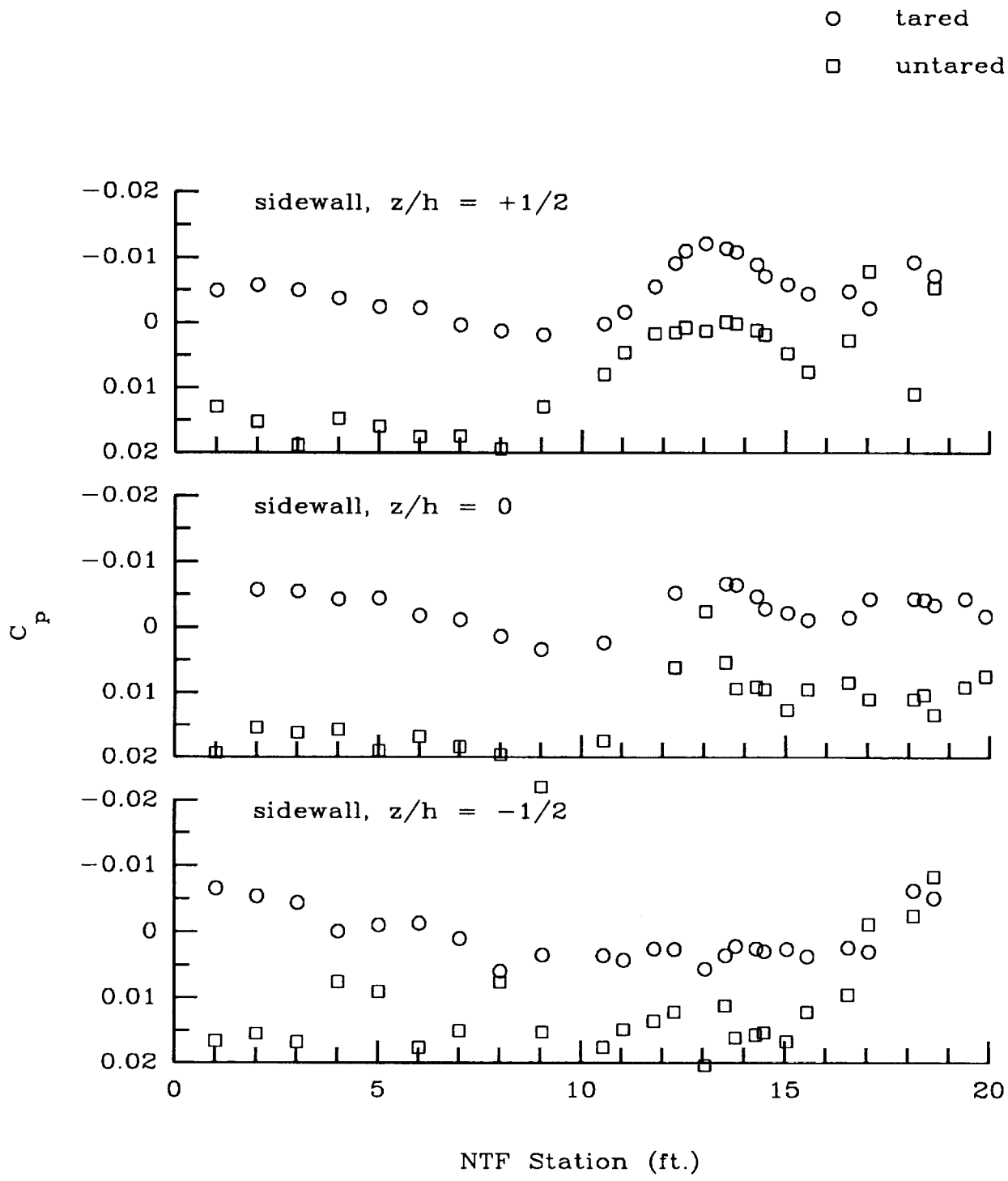
Figure 6. Untared and tared wall pressure coefficient measurements. Pathfinder I at  $M = 0.80$ ,  $C_L = 0.514$ , and  $R = 4.0 \times 10^6$  per foot.

○ tared  
□ untared



(b) Floor orifice rows.

Figure 6. Continued.



(c) Sidewall orifice rows.

Figure 6. Concluded.

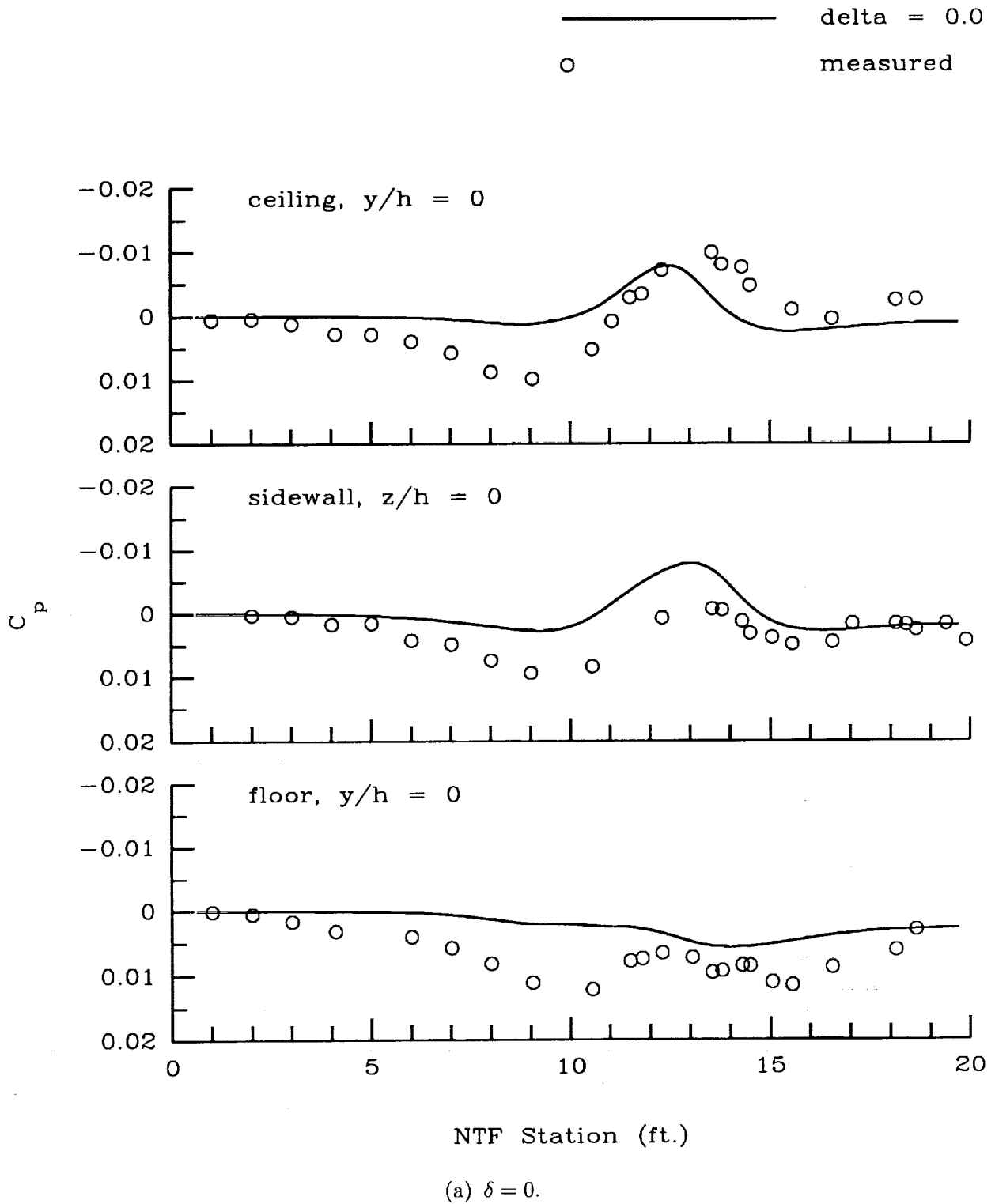
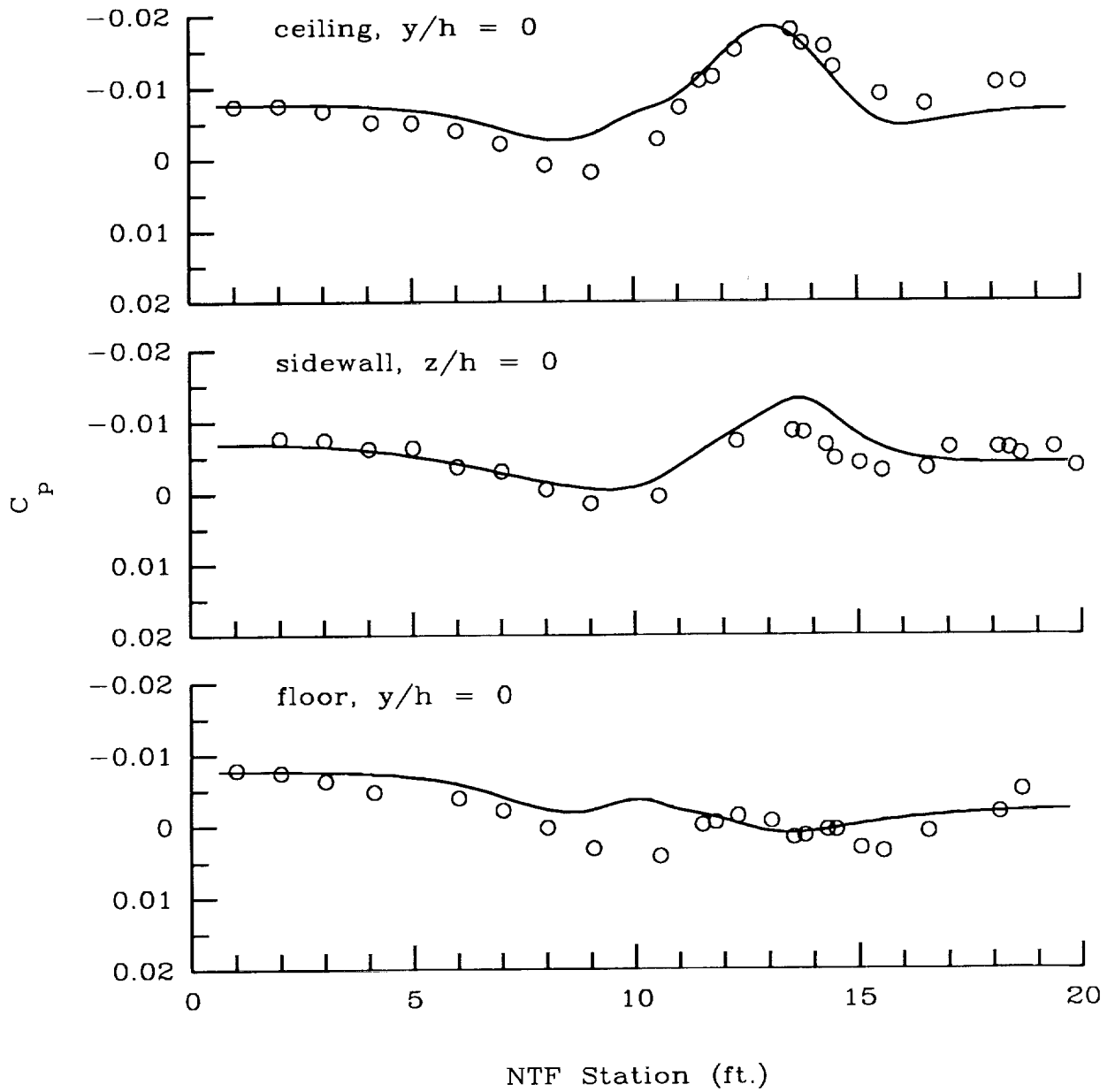


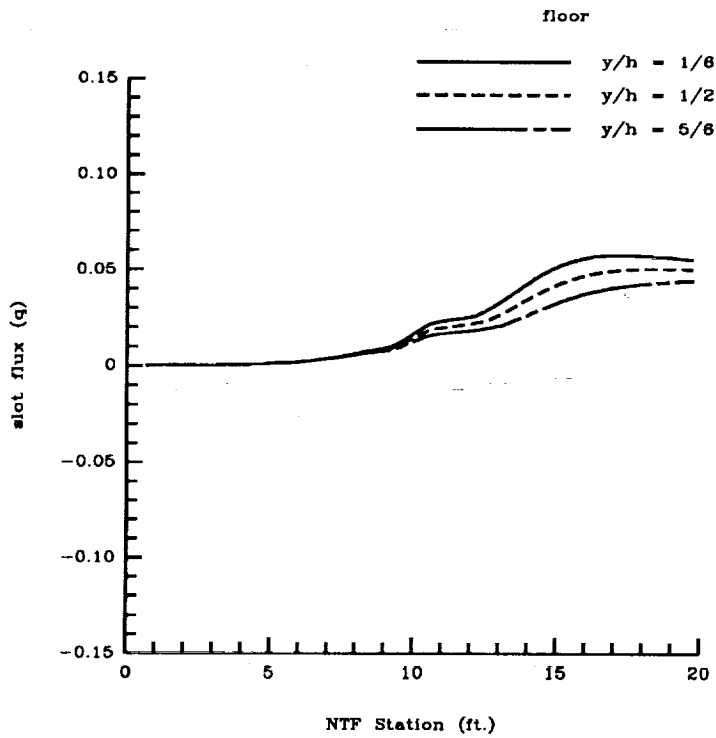
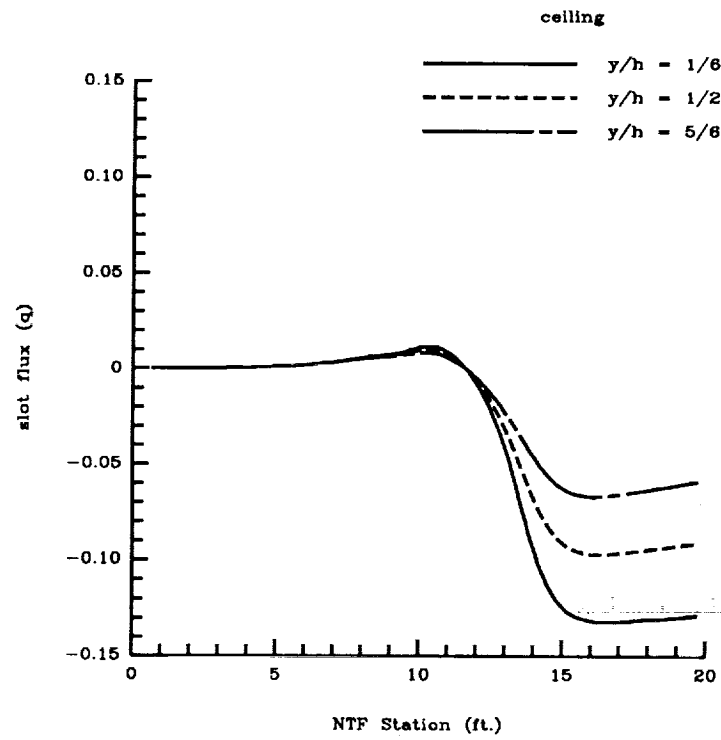
Figure 7. Effect of plenum pressure on wall centerline pressure coefficients with Pathfinder I at  $M = 0.80$  and  $\alpha = 2.70^\circ$ .

\_\_\_\_\_  $\delta = -0.004$   
 ○ measured



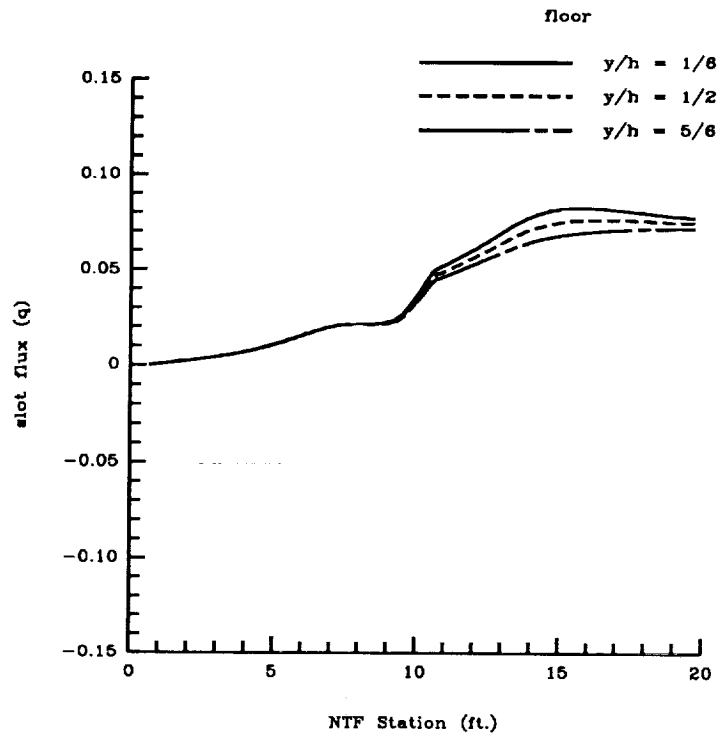
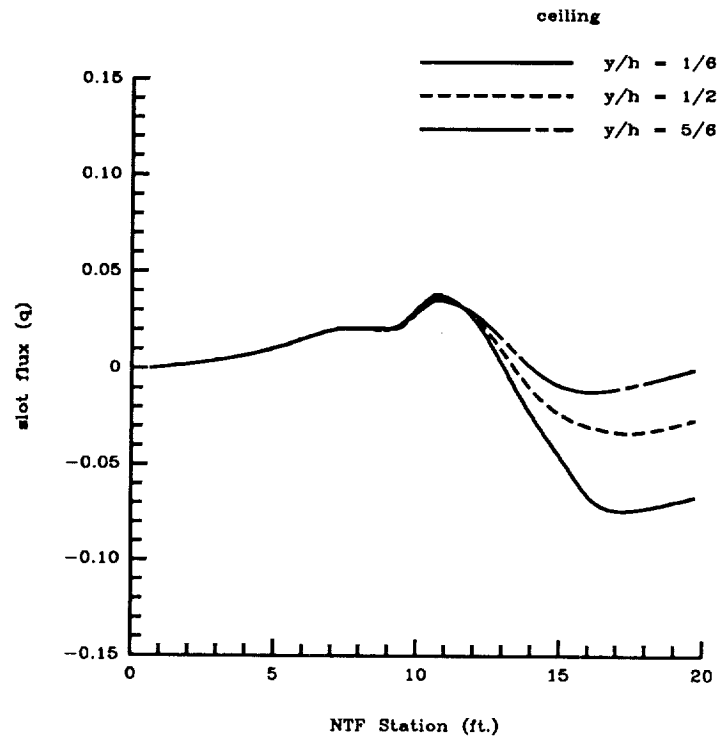
(b)  $\delta = -0.004$ .

Figure 7. Concluded.



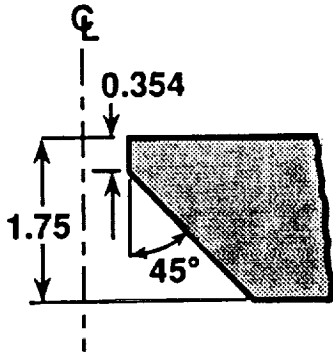
(a)  $\delta = 0$ .

Figure 8. Effect of plenum pressure on slot volume flux with Pathfinder I at  $M = 0.80$  and  $\alpha = 2.70^\circ$ .

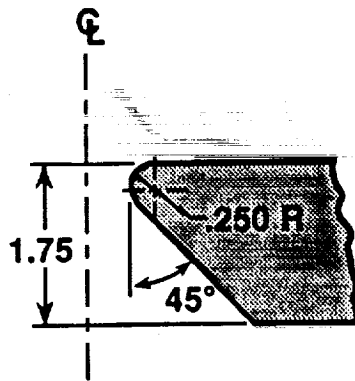


(b)  $\delta = -0.004$ .

Figure 8. Concluded.



upstream of tunnel station 5



downstream of tunnel station 5

Figure 9. Sketch of NTF slot lip shape. All linear dimensions are in inches.

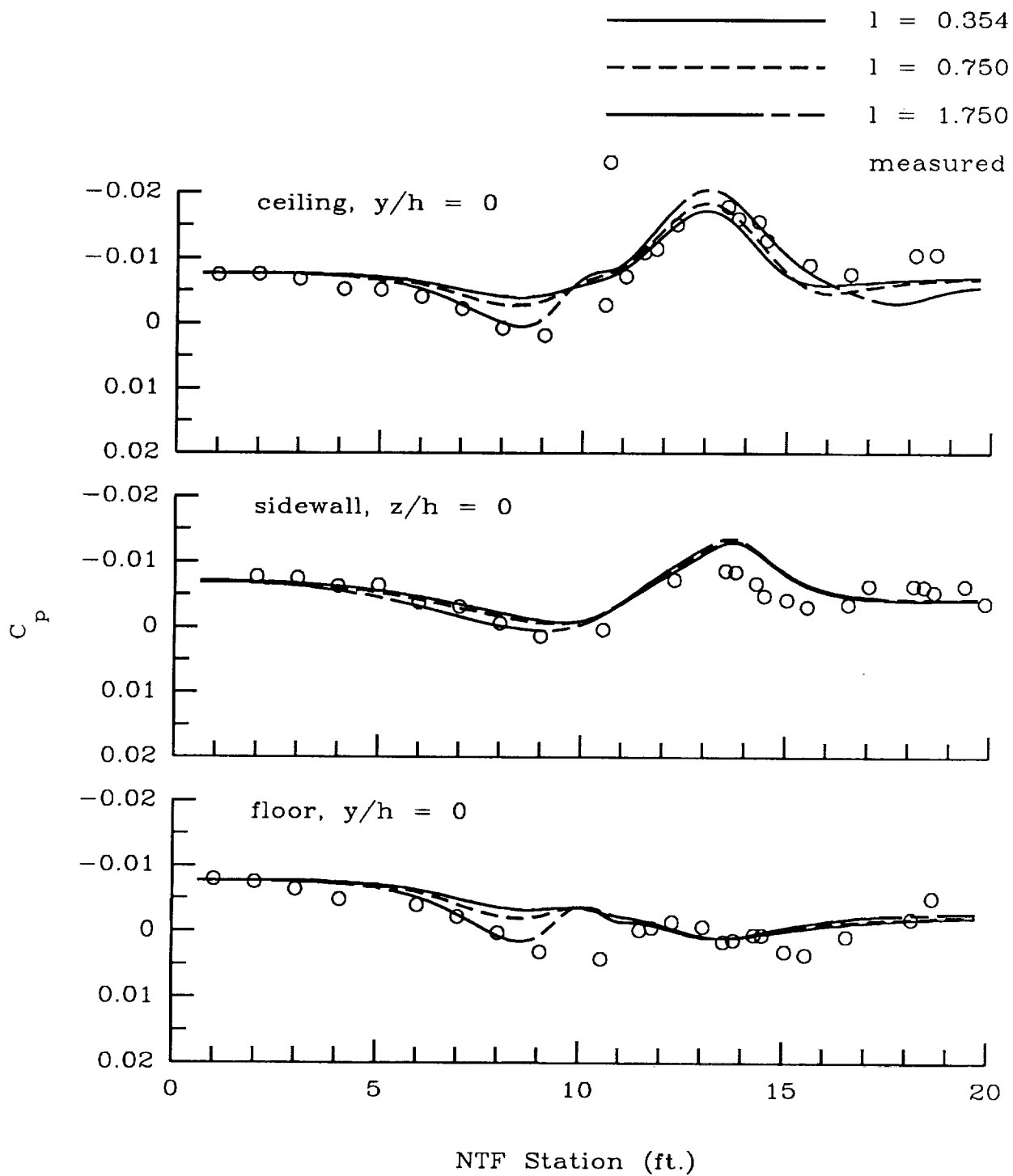
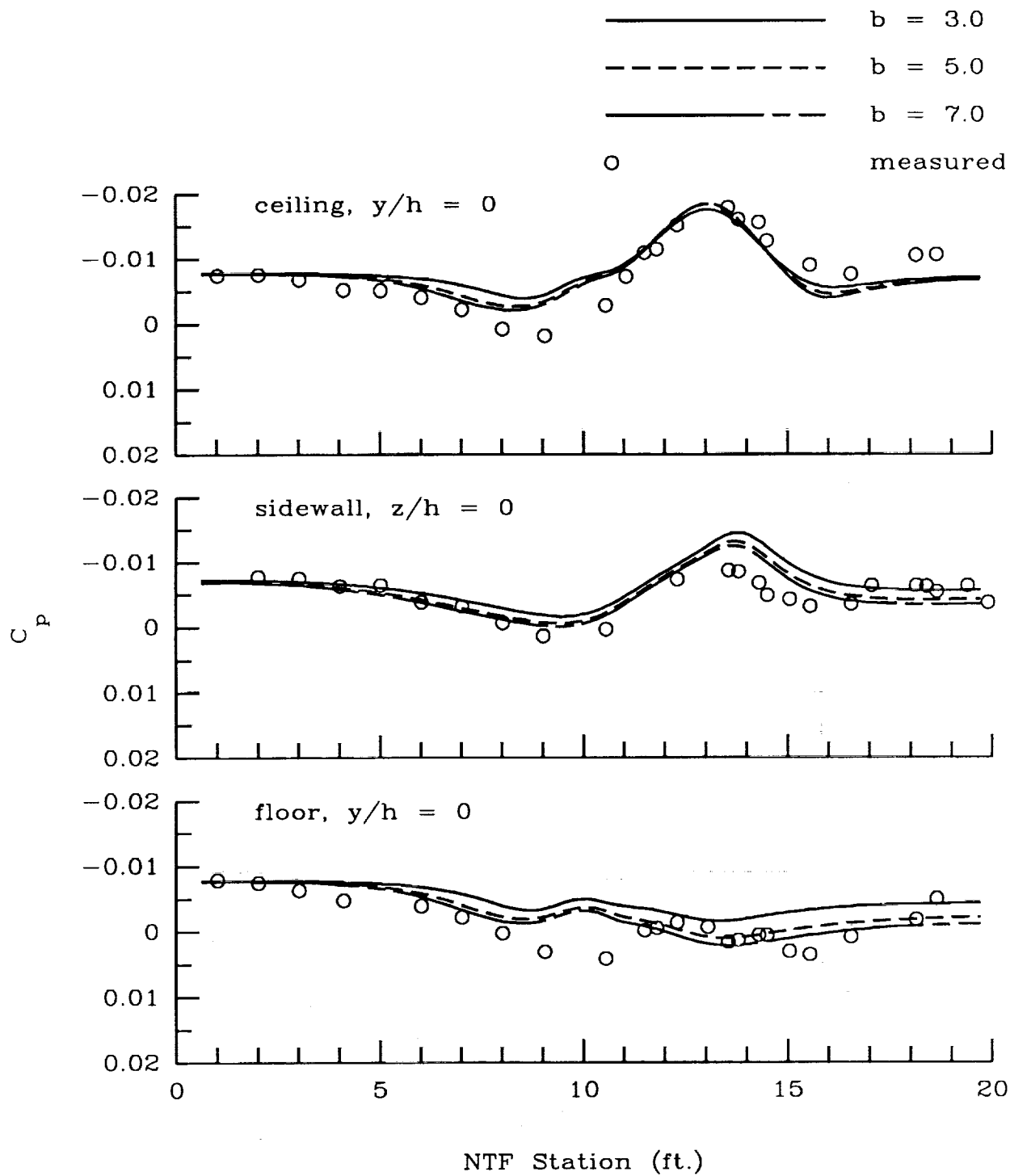
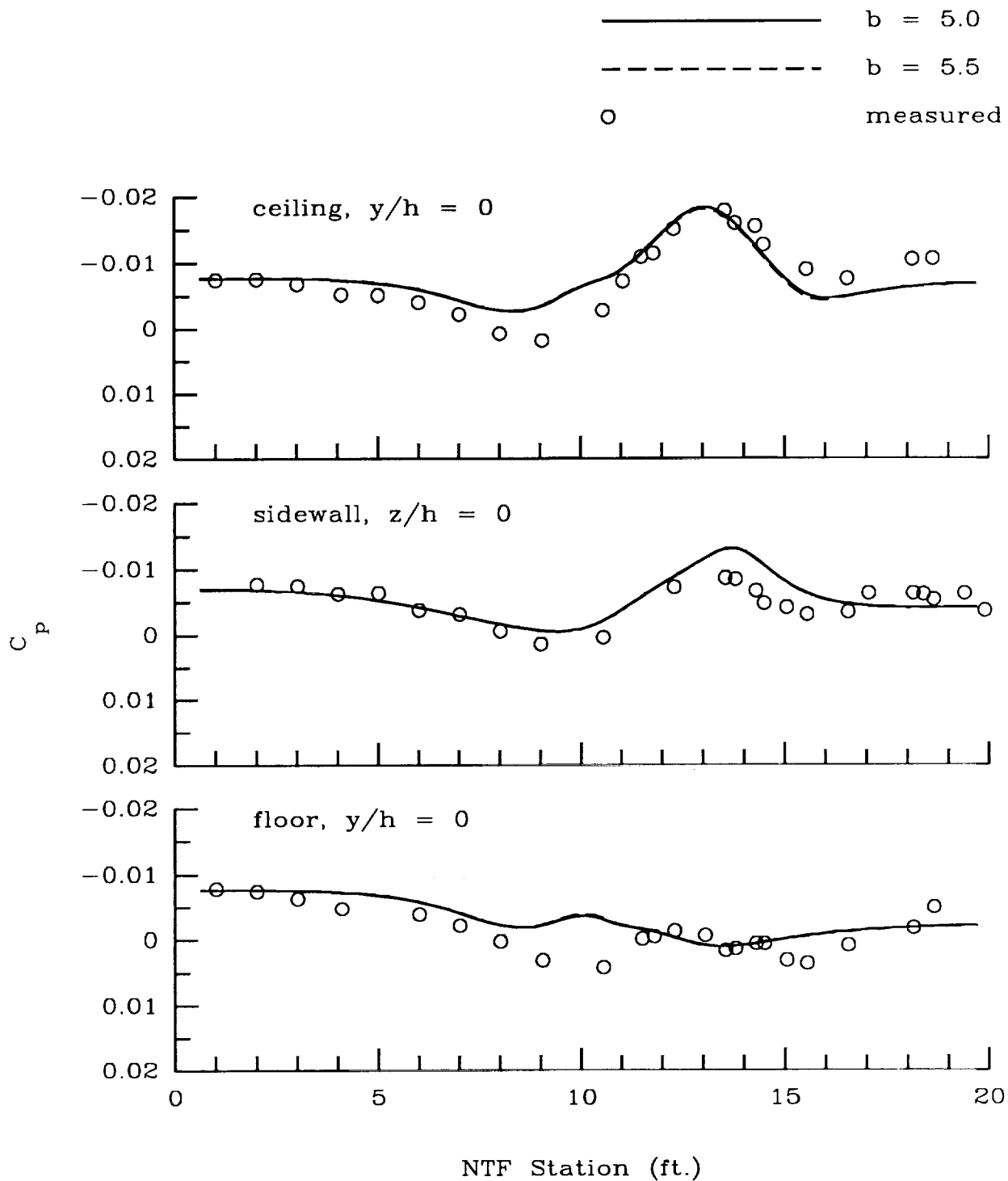


Figure 10. Effect of slot depth on wall centerline pressure coefficients with Pathfinder I at  $M = 0.80$  and  $\alpha = 2.70^\circ$ .



(a)  $b = 3-7$  in.

Figure 11. Effect of slot strip width on wall centerline pressure coefficients with Pathfinder I at  $M = 0.80$  and  $\alpha = 2.70^\circ$ .



(b)  $b \approx 5$  in. (varying strip resolution).

Figure 11. Concluded.

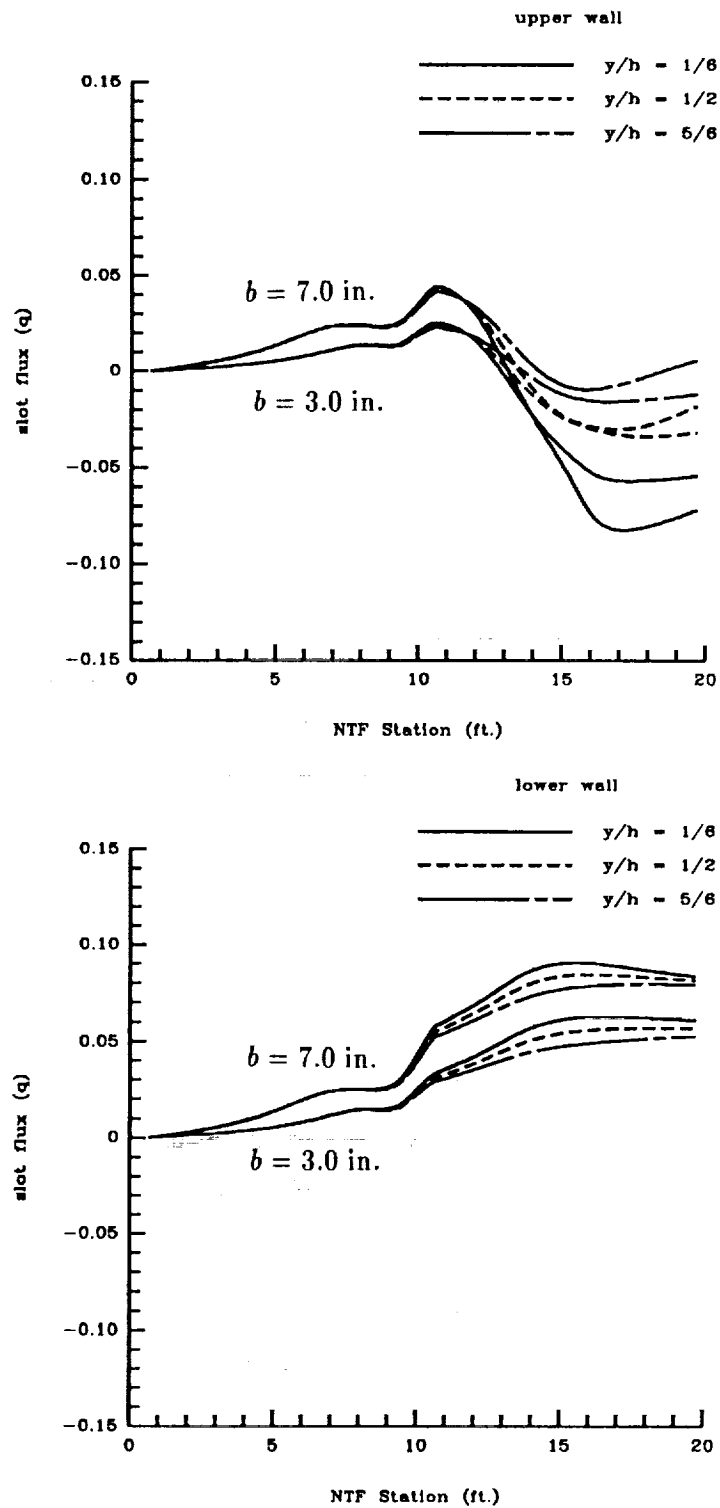


Figure 12. Effect of slot strip width on slot volume flux with Pathfinder I at  $M = 0.80$  and  $\alpha = 2.70^\circ$ .

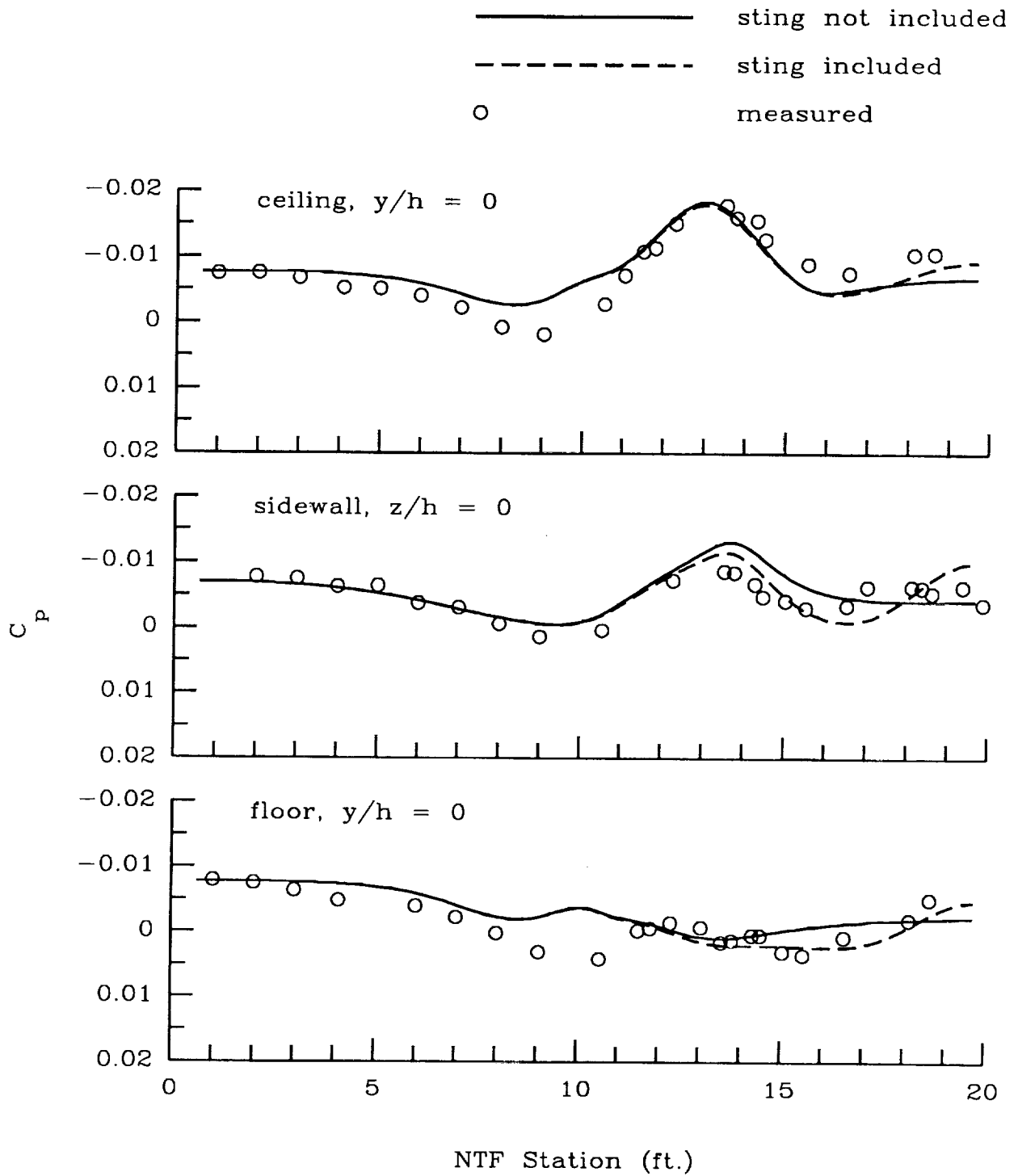


Figure 13. Effect of sting representation on wall centerline pressure coefficients with Pathfinder I at  $M = 0.80$  and  $\alpha = 2.70^\circ$ .

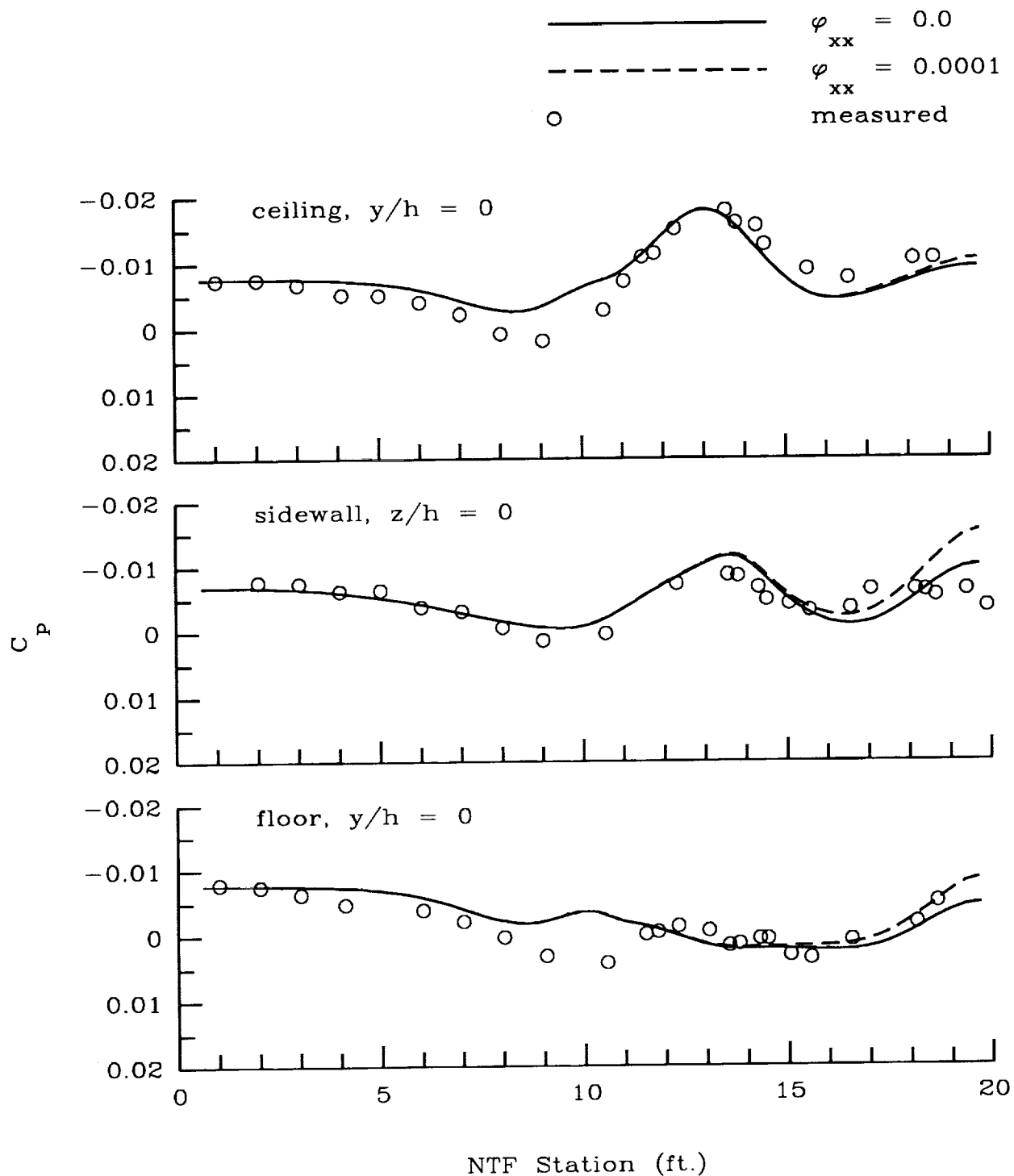


Figure 14. Effect of outflow plane value of  $\phi_{xx}$  on wall centerline pressure coefficients with Pathfinder I at  $M = 0.80$  and  $\alpha = 2.70^\circ$ .

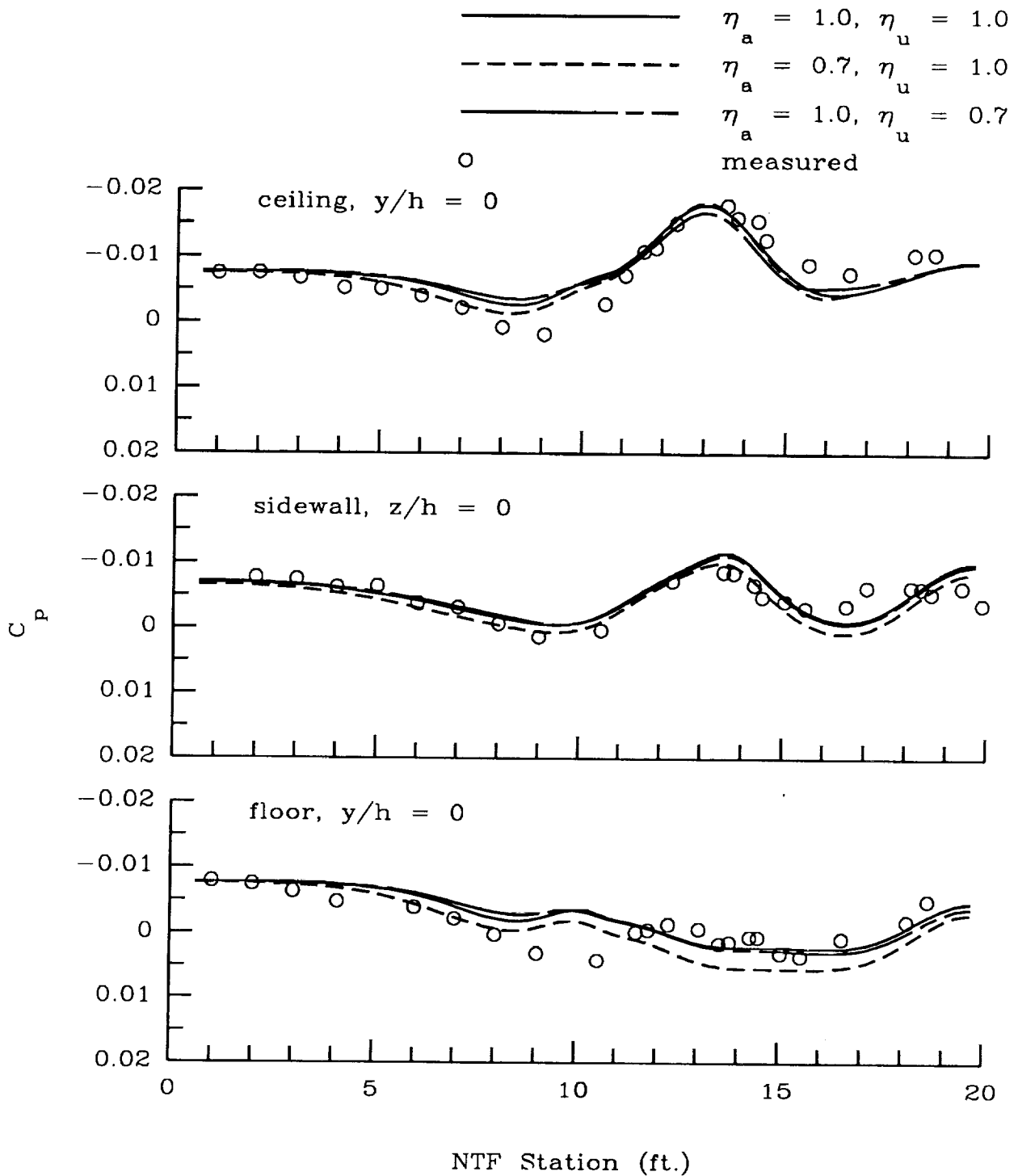
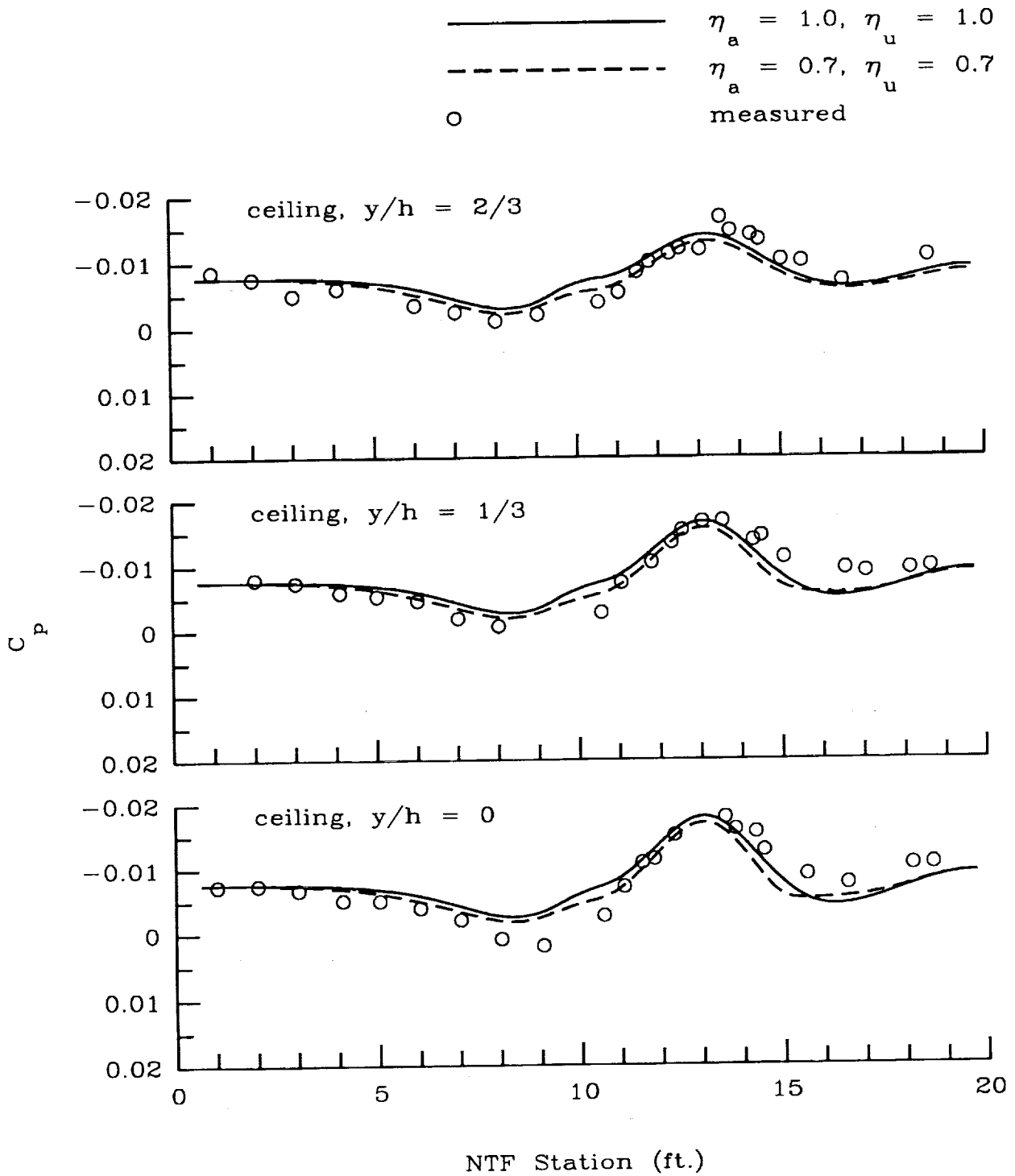
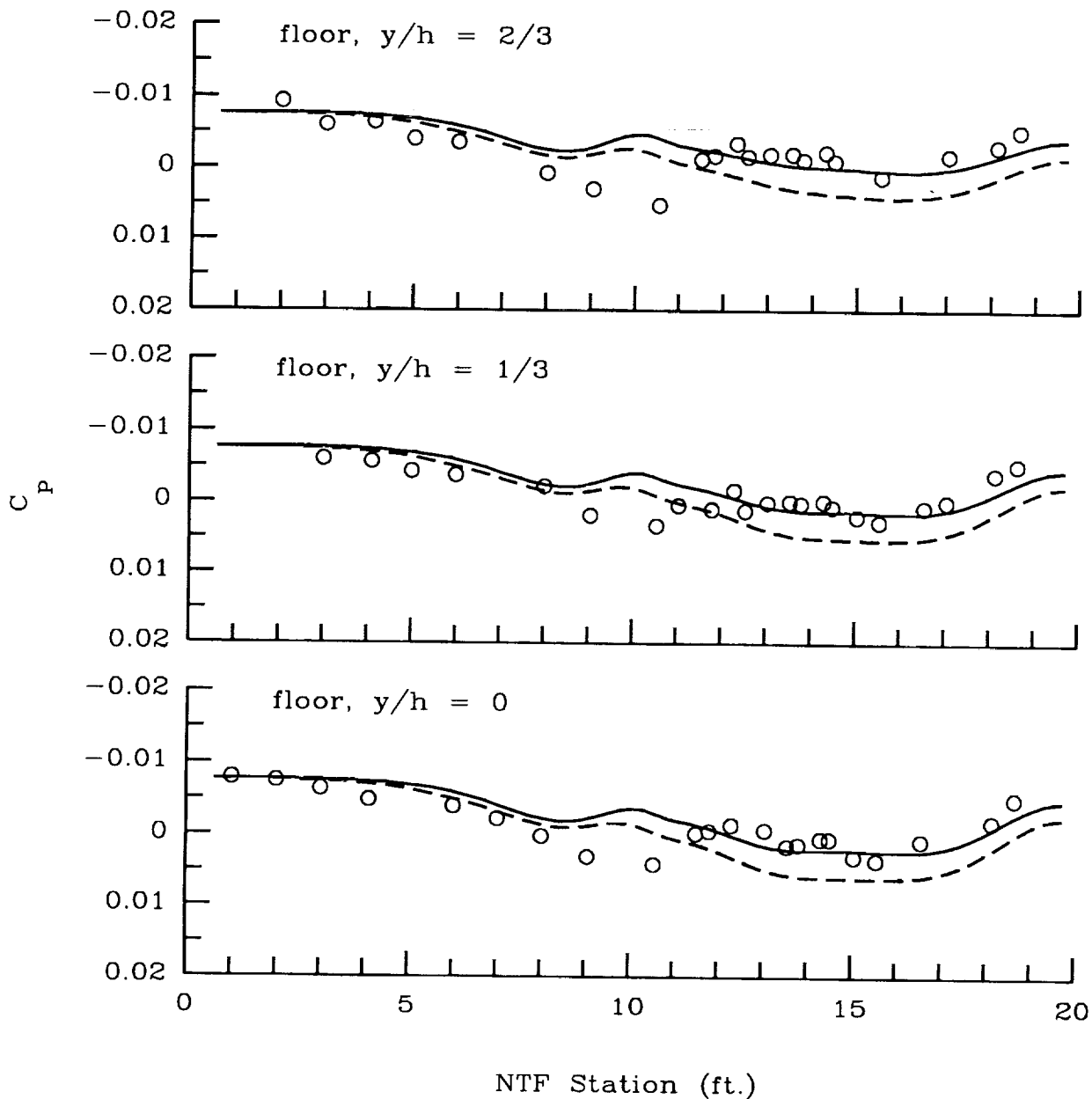
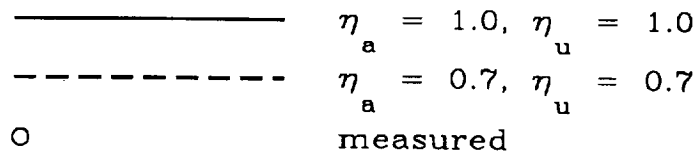


Figure 15. Effect of varying slot viscous reduction parameters individually on wall centerline pressure coefficients with Pathfinder I at  $M = 0.80$  and  $\alpha = 2.70^\circ$ .



(a) Ceiling orifice rows.

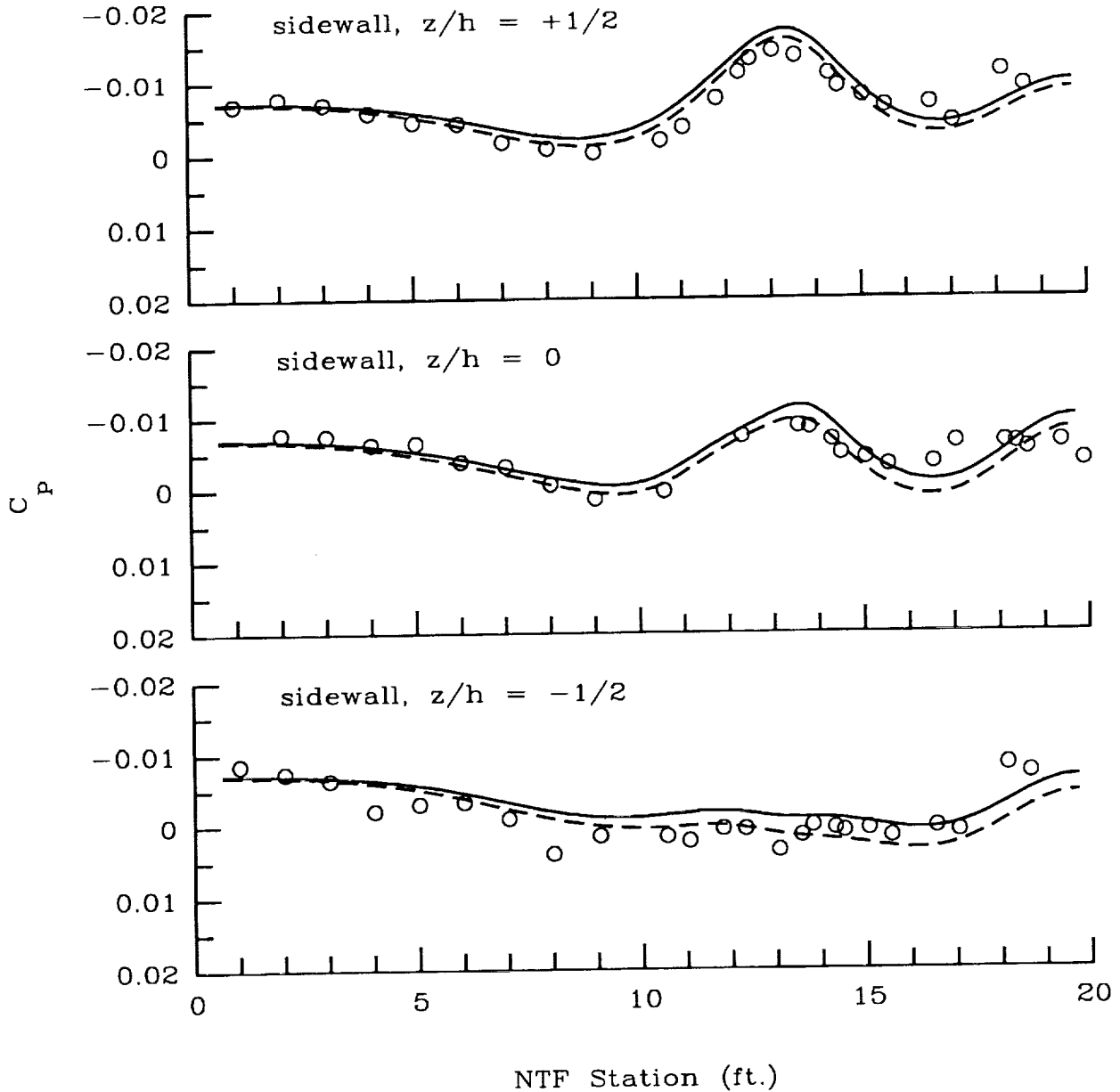
Figure 16. Effect of varying slot viscous reduction parameters simultaneously on wall pressure coefficients with Pathfinder I at  $M = 0.80$  and  $\alpha = 2.70^\circ$ .



(b) Floor orifice rows.

Figure 16. Continued.

—————	$\eta_a = 1.0, \eta_u = 1.0$
- - - - -	$\eta_a = 0.7, \eta_u = 0.7$
o	measured



(c) Sidewall orifice rows.

Figure 16. Concluded.

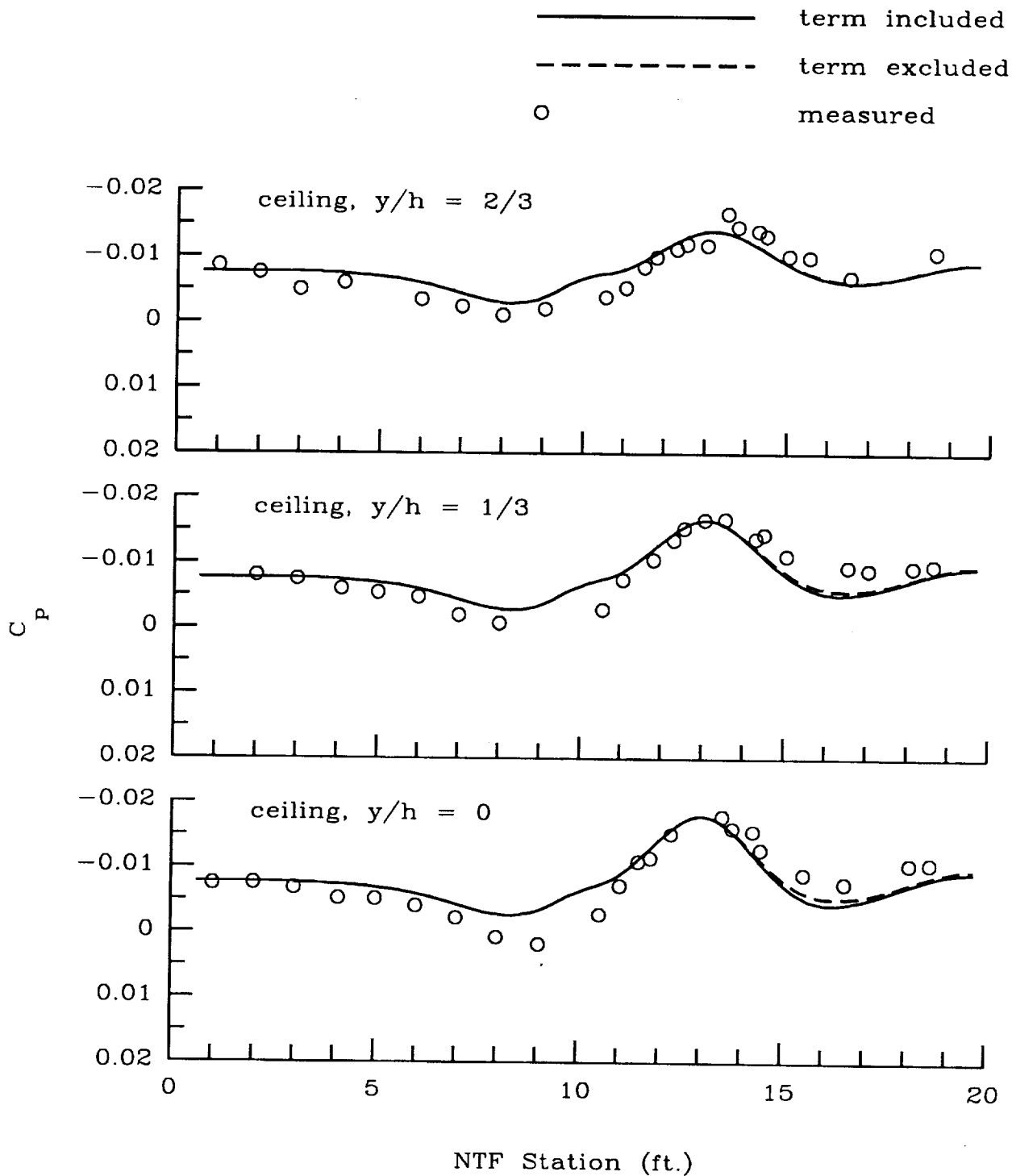


Figure 17. Effect of slot inflow modification on ceiling pressure coefficients with Pathfinder I at  $M = 0.80$  and  $\alpha = 2.70^\circ$ .

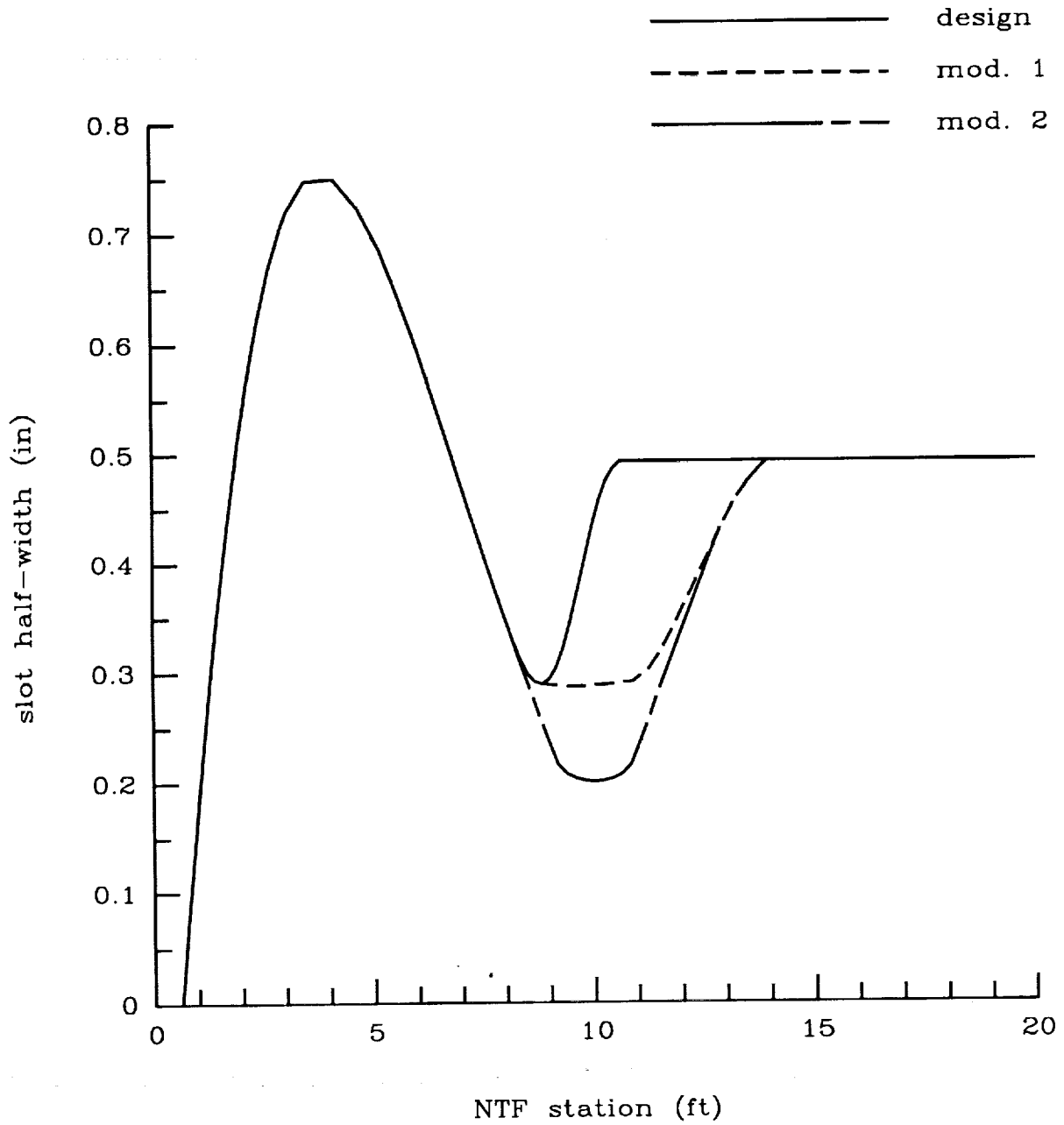


Figure 18. Slot width modifications 1 and 2 compared with actual NTF slot shape.

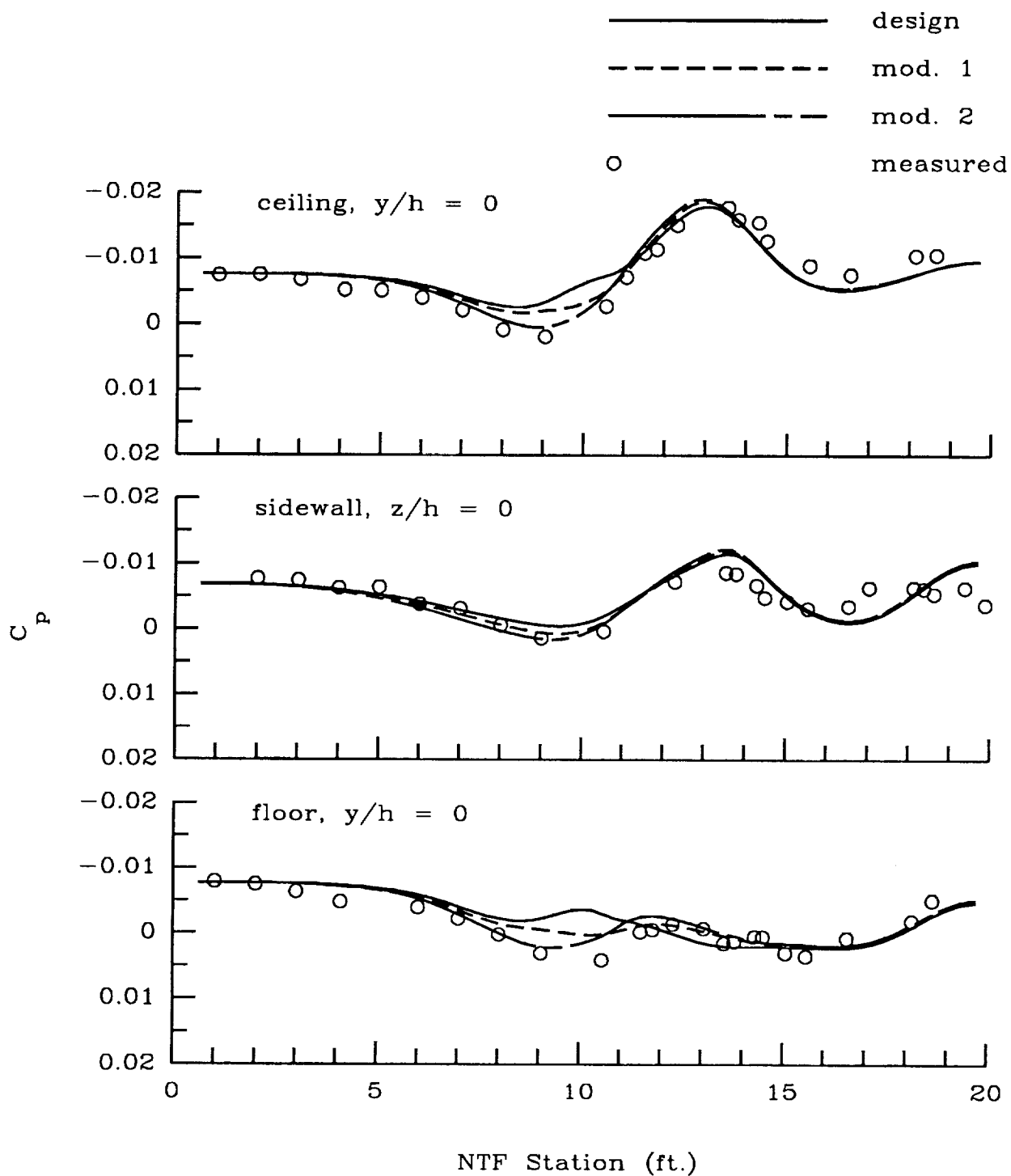


Figure 19. Effect of slot modifications 1 and 2 on wall centerline pressure coefficients with Pathfinder I at  $M = 0.80$  and  $\alpha = 2.70^\circ$ .

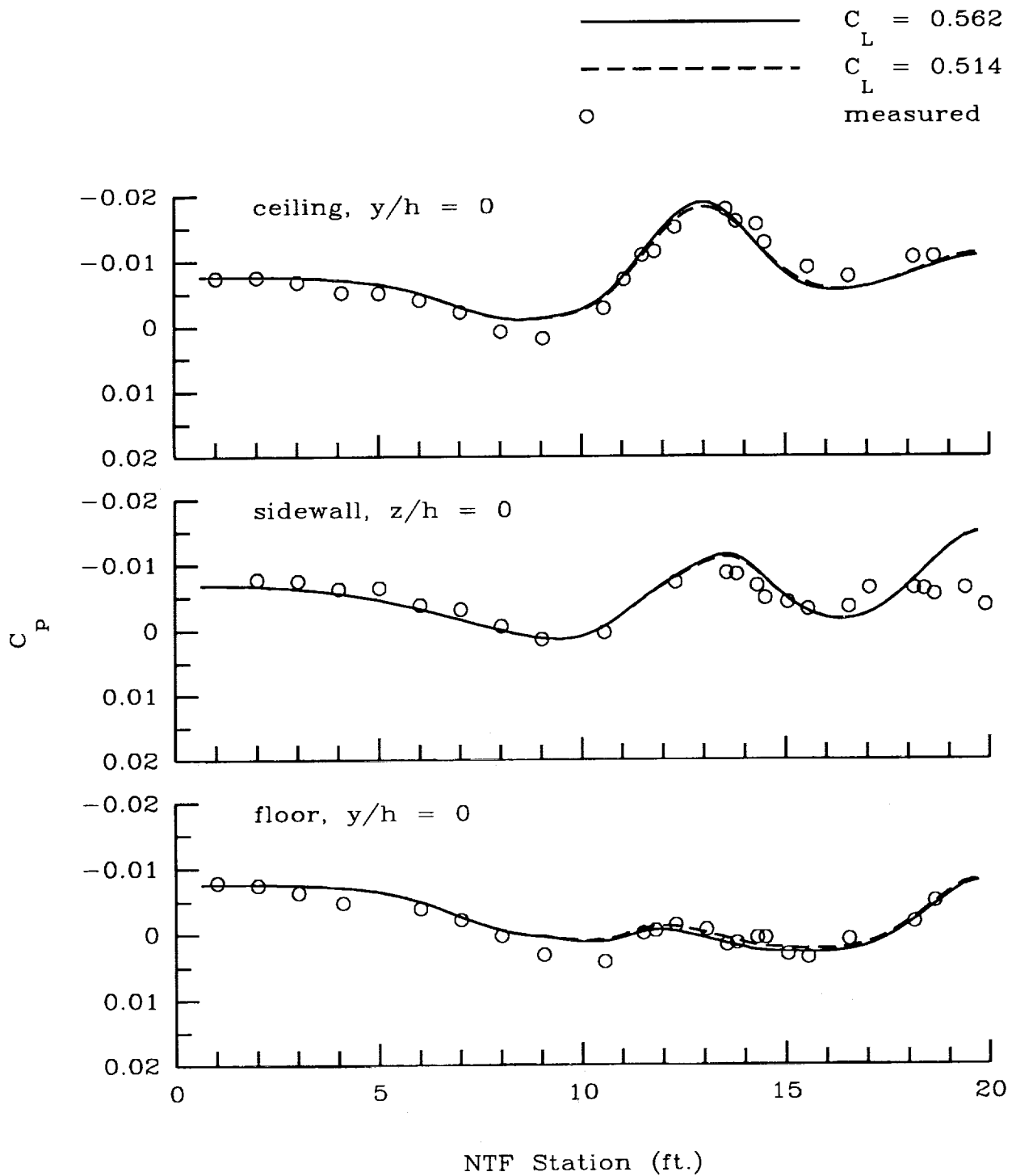


Figure 20. Effect of adjusting angle of attack to match experimental  $C_L$  of 0.514. Wall centerline pressure coefficients with Pathfinder I at  $M = 0.80$ .

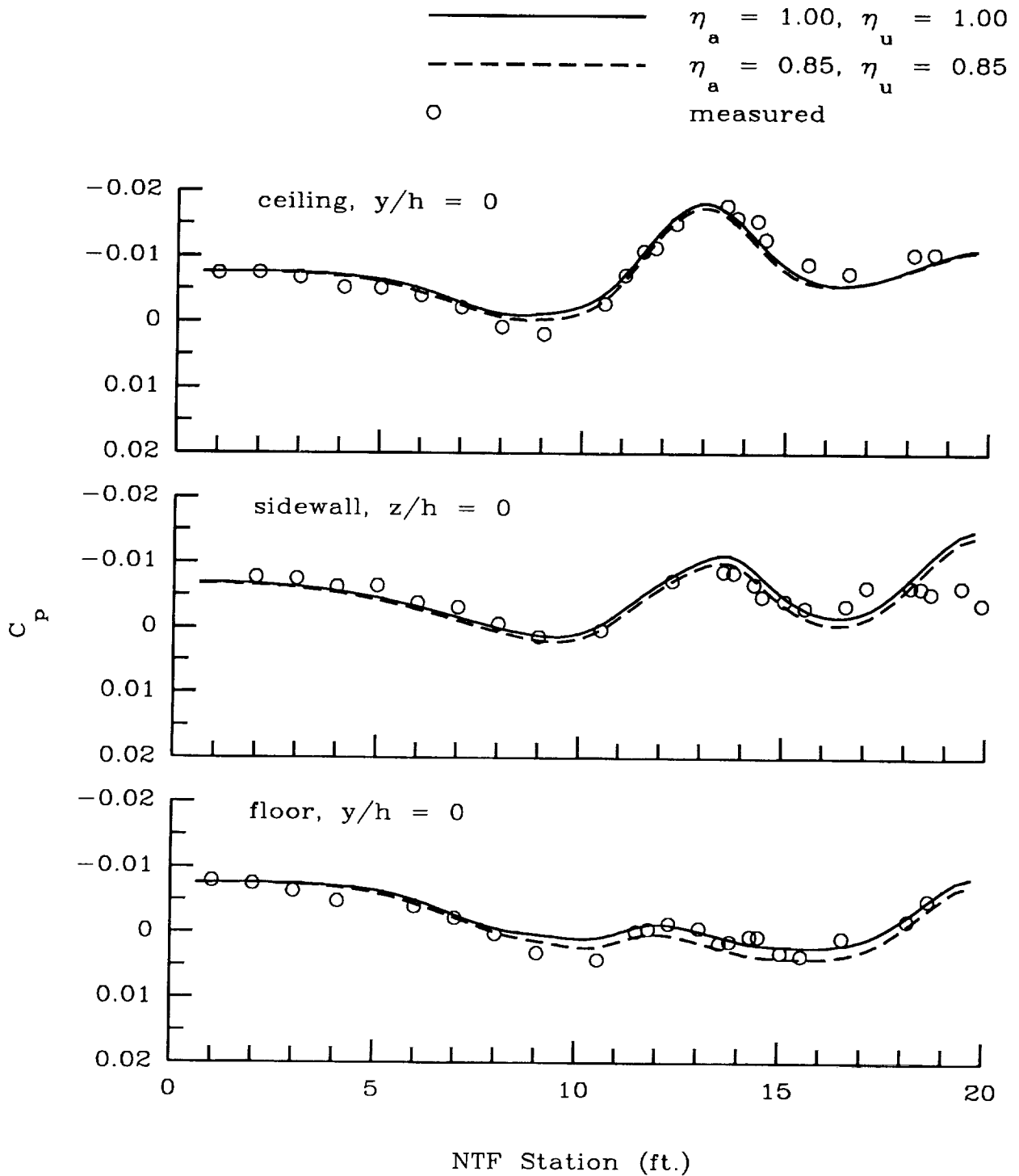
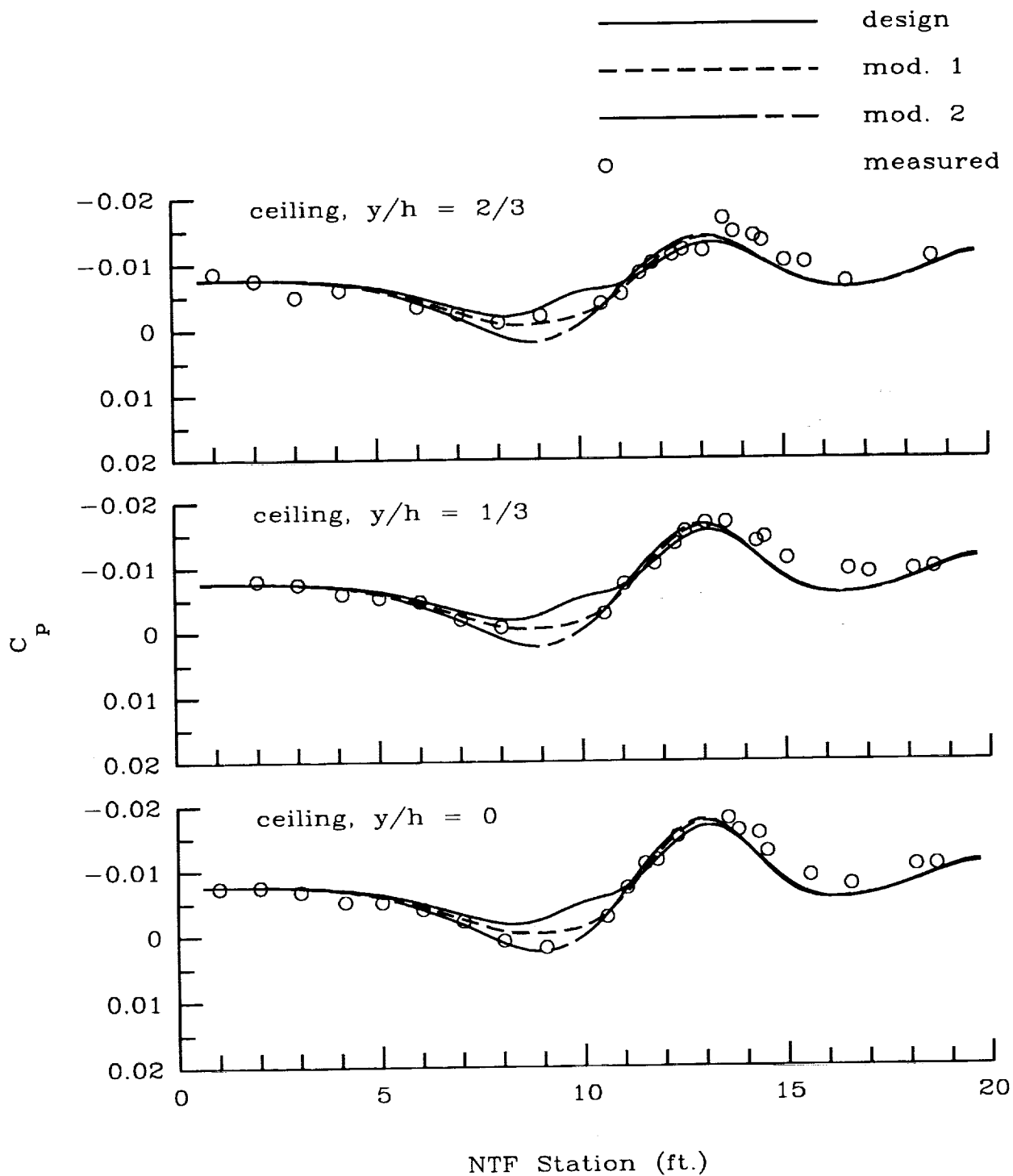
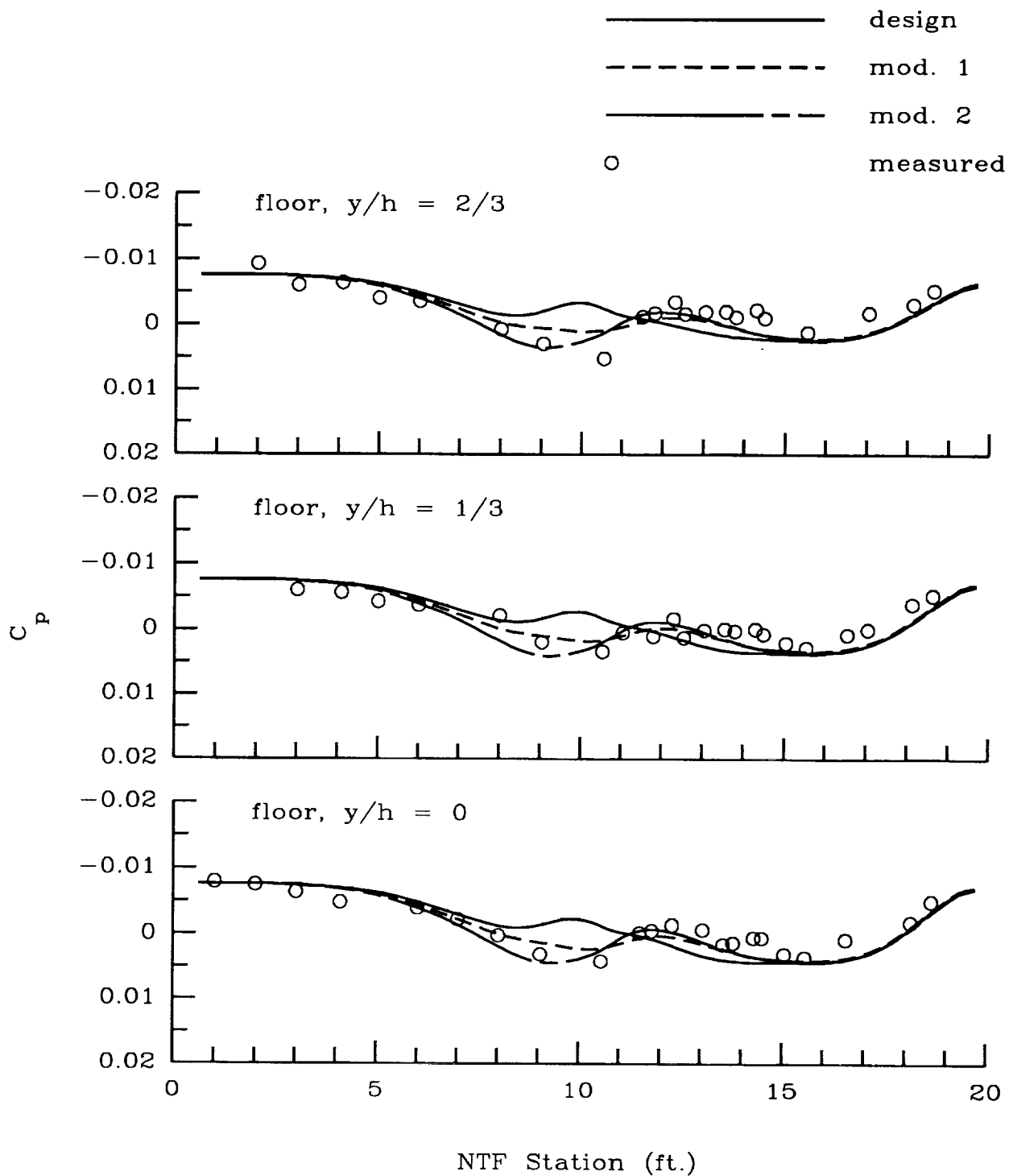


Figure 21. Effect of 15-percent reductions in slot viscous parameters on wall centerline pressure coefficients with Pathfinder I at  $M = 0.80$  and  $\alpha = 2.30^\circ$ .



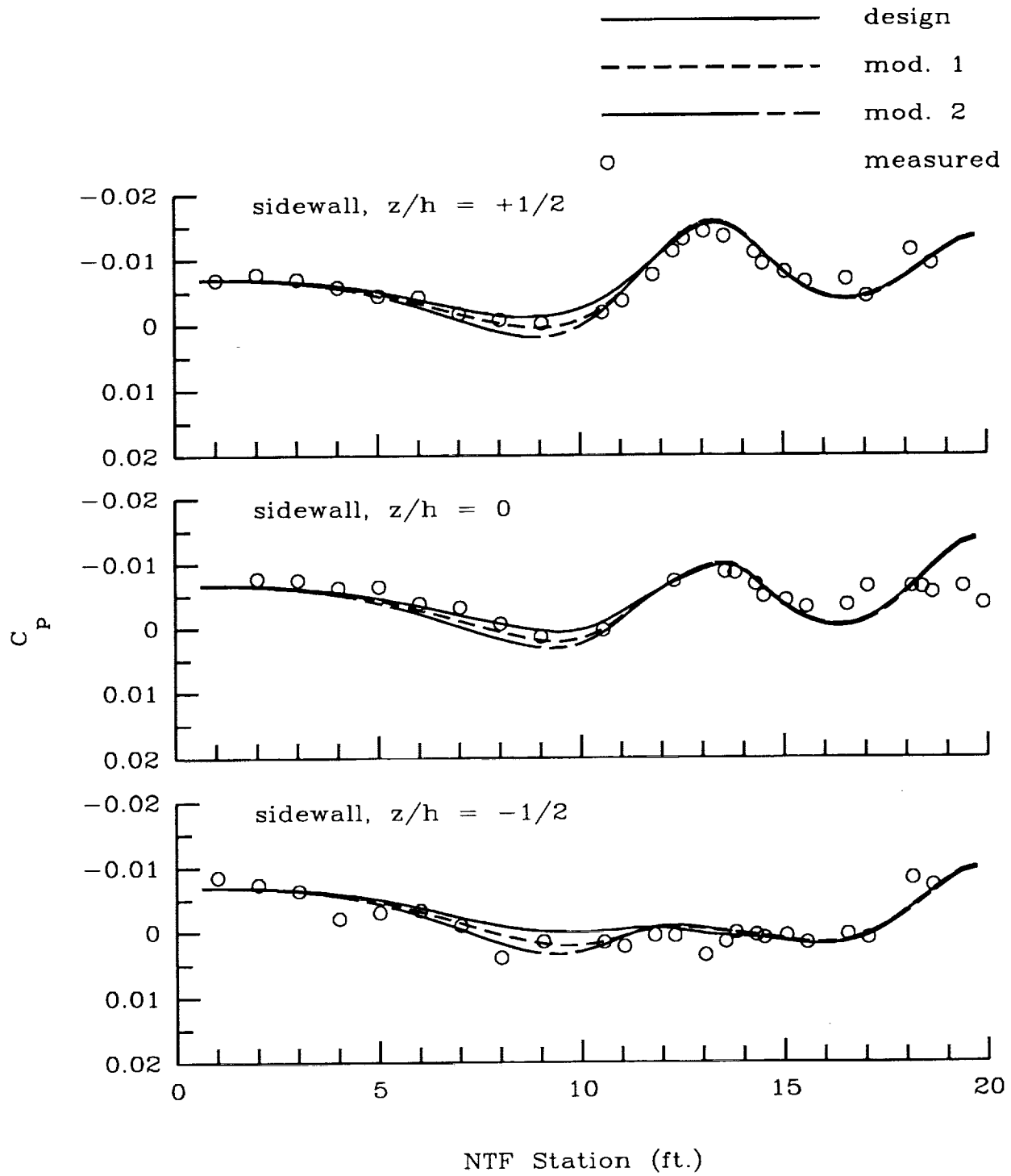
(a) Ceiling orifice rows.

Figure 22. Effect of slot modifications 1 and 2 on wall pressure coefficients with Pathfinder I at  $M = 0.80$  and  $\alpha = 2.30^\circ$



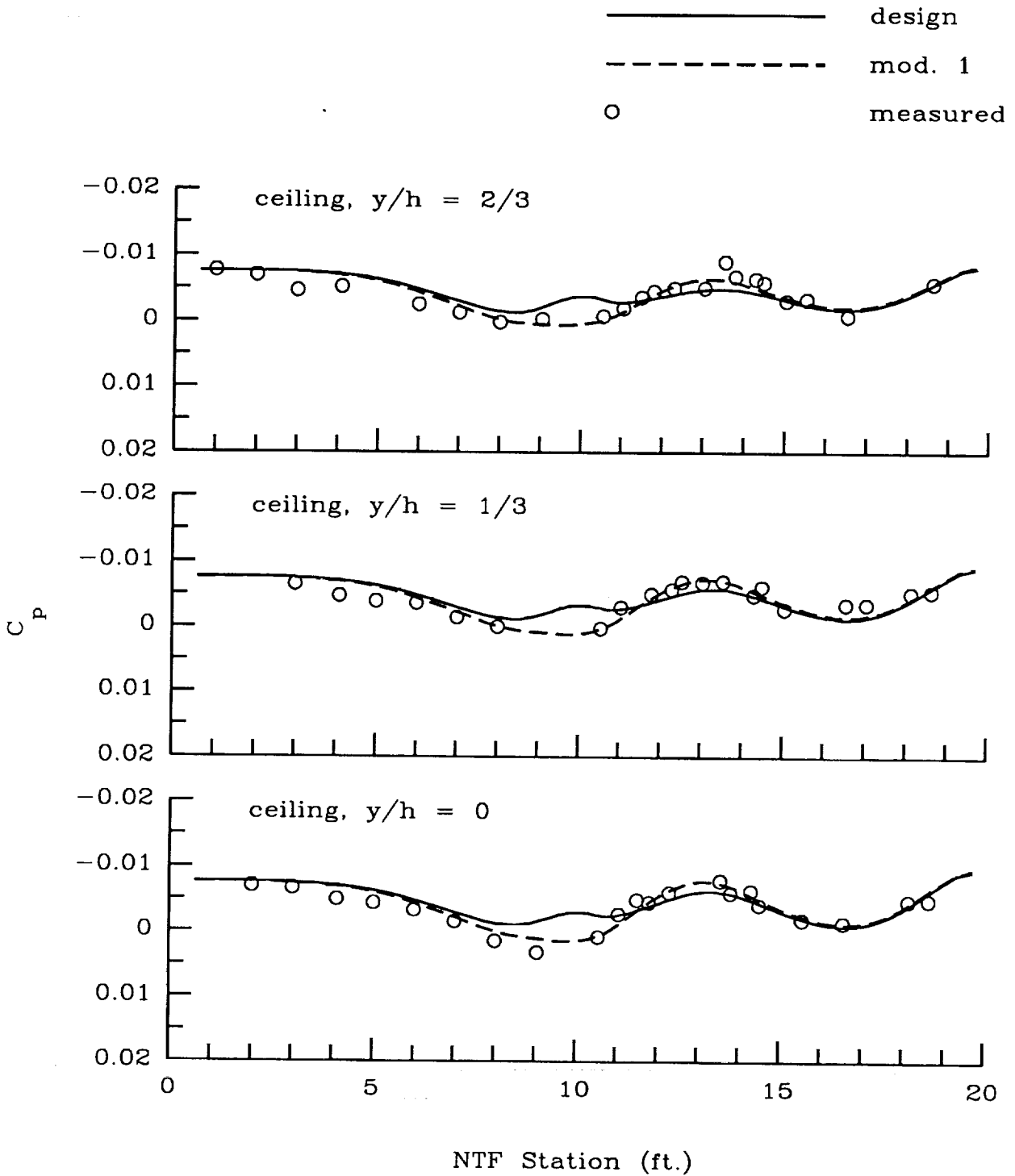
(b) Floor orifice rows.

Figure 22. Continued.



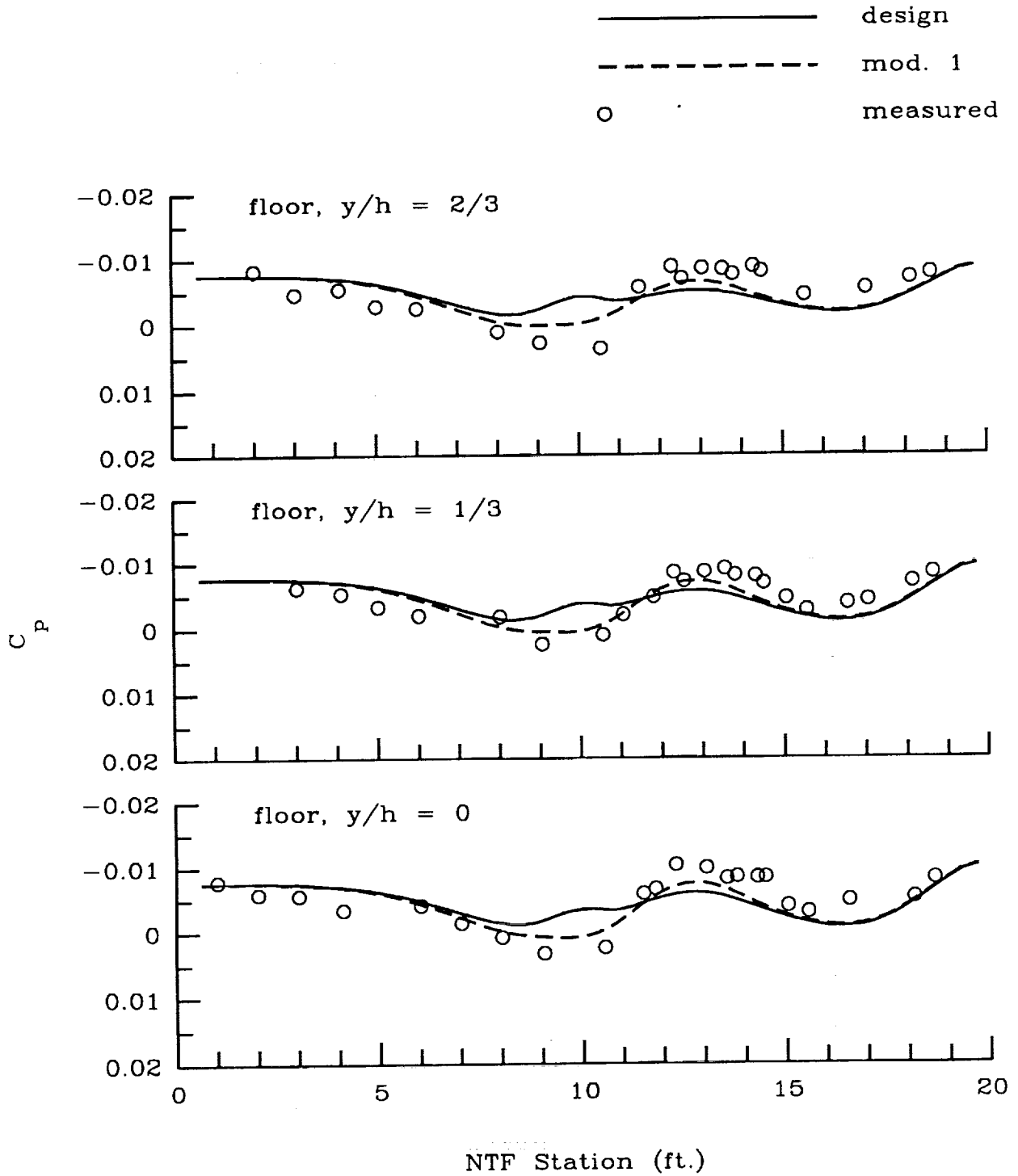
(c) Sidewall orifice rows.

Figure 22. Concluded.



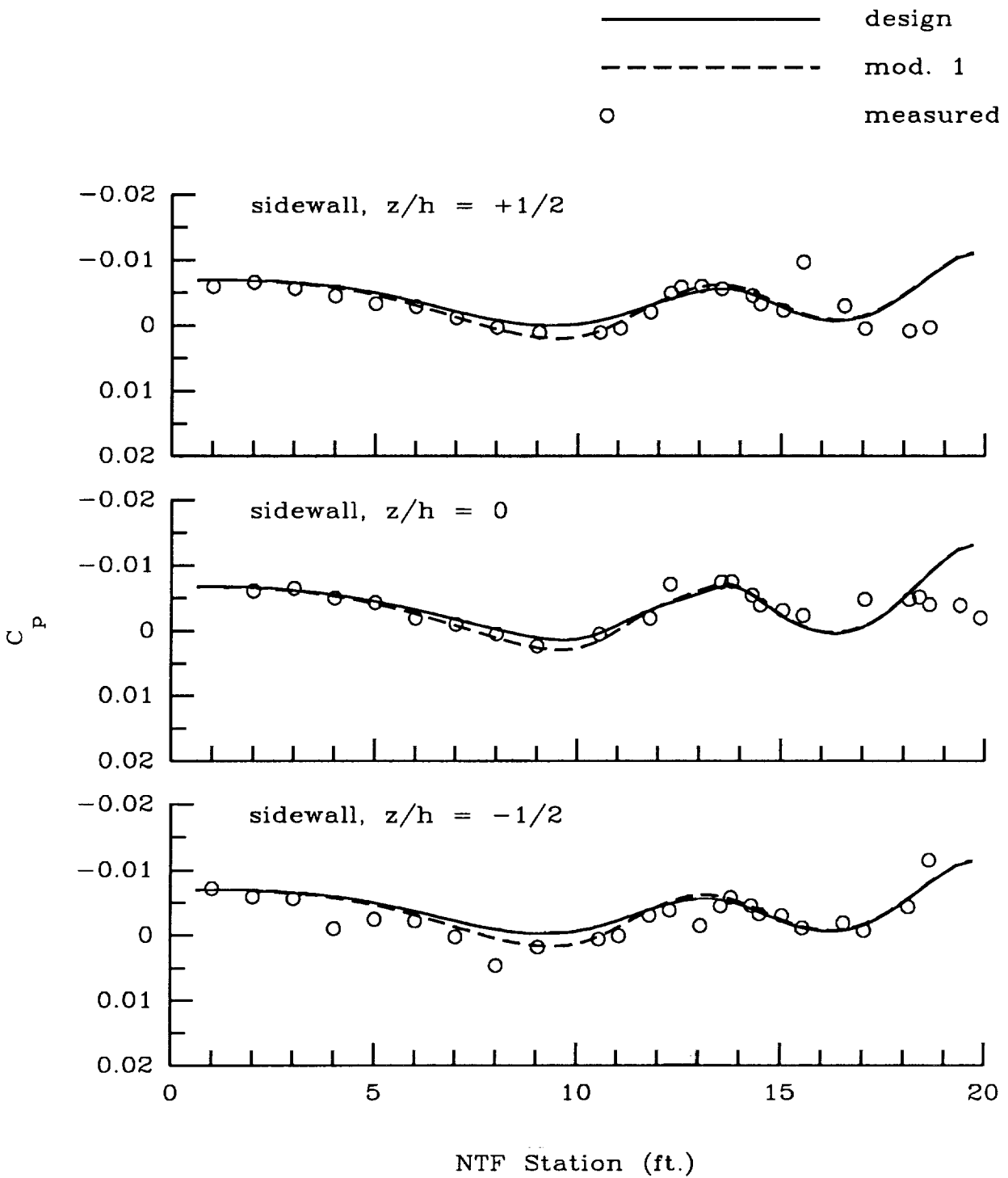
(a) Ceiling orifice rows.

Figure 23. Effect of slot modification 1 on wall pressure coefficients with Pathfinder I at  $M = 0.80$  and  $\alpha = -2^\circ$ .



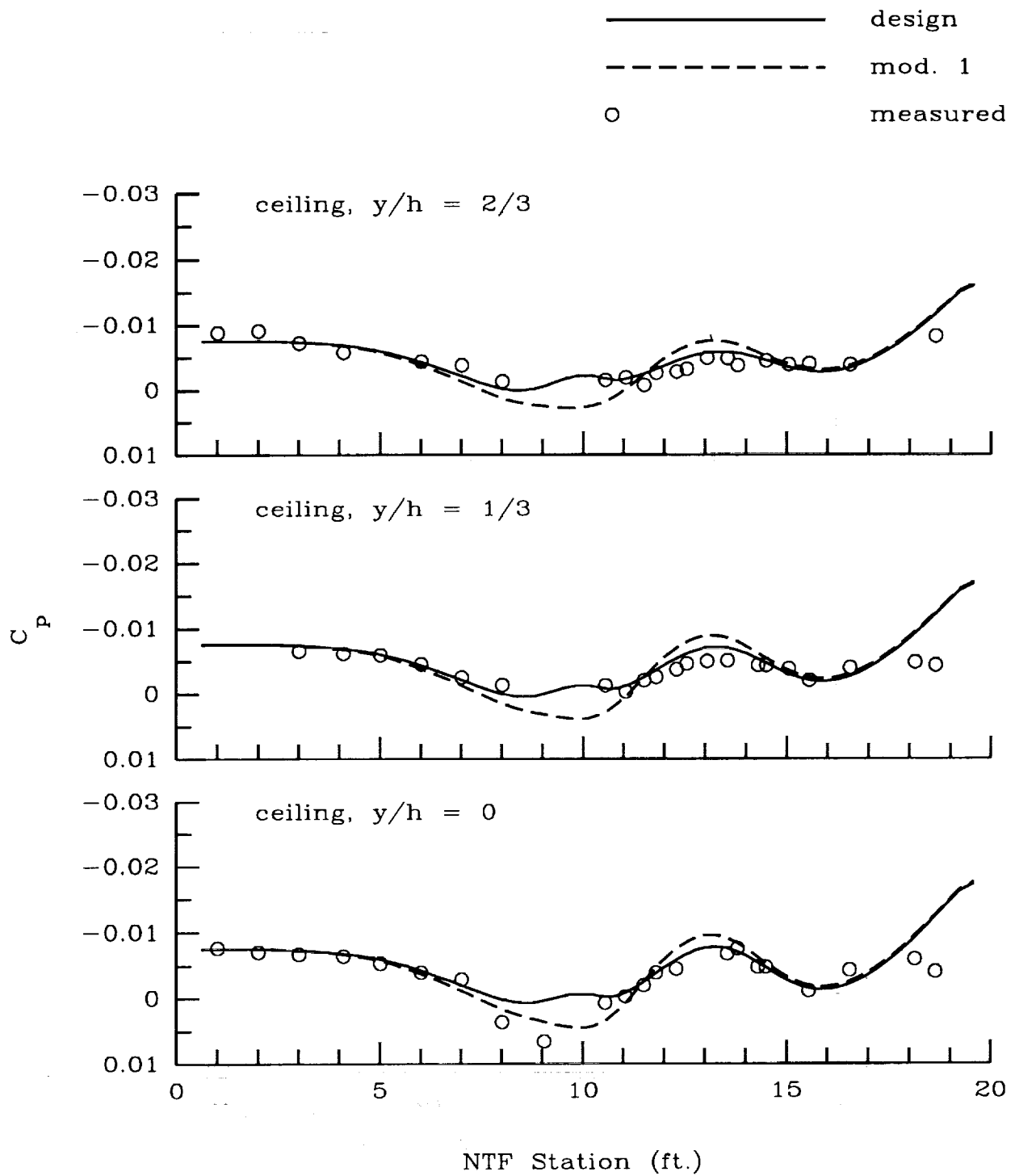
(b) Floor orifice rows.

Figure 23. Continued.



(c) Sidewall orifice rows.

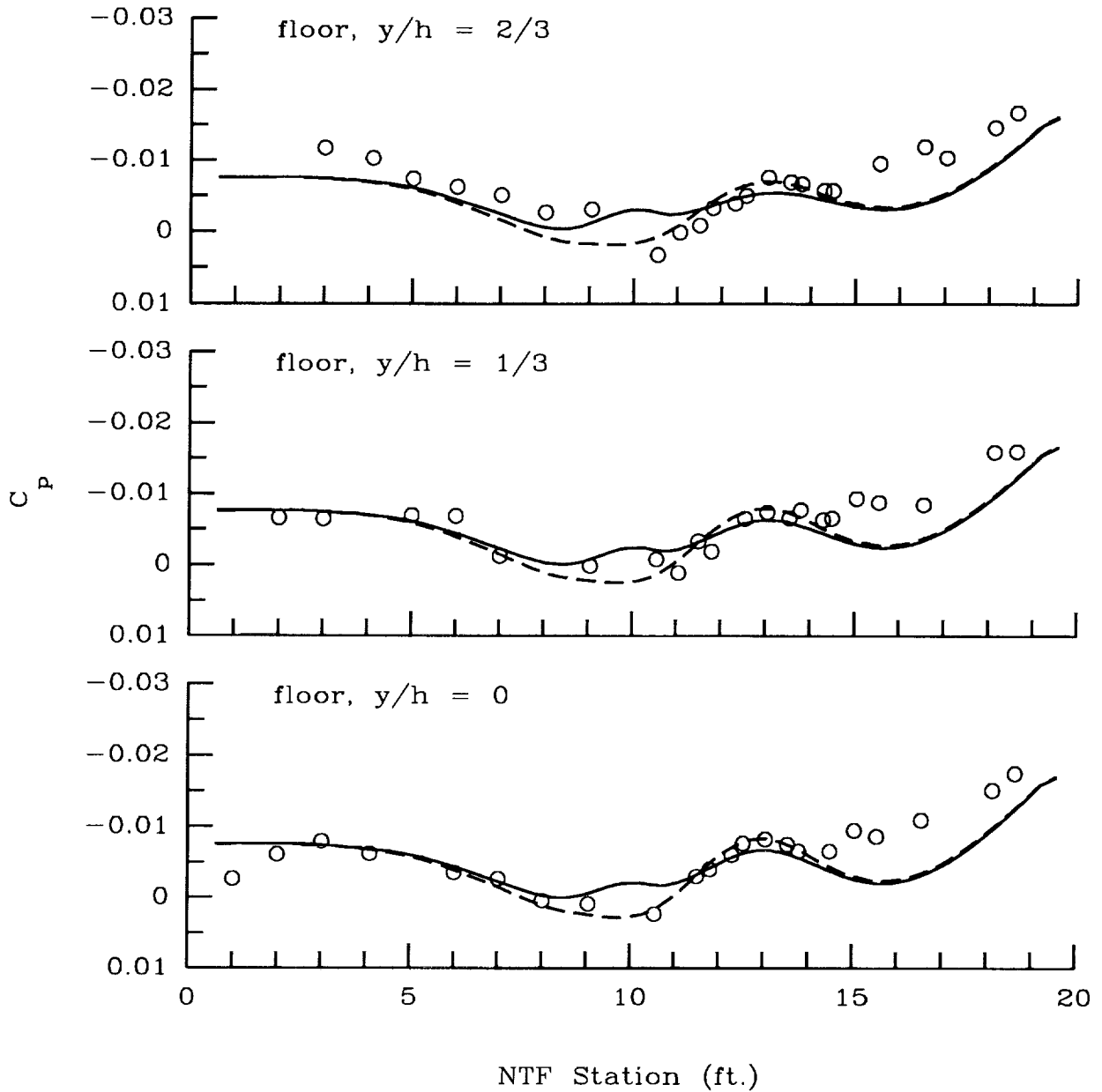
Figure 23. Concluded.



(a) Ceiling orifice rows.

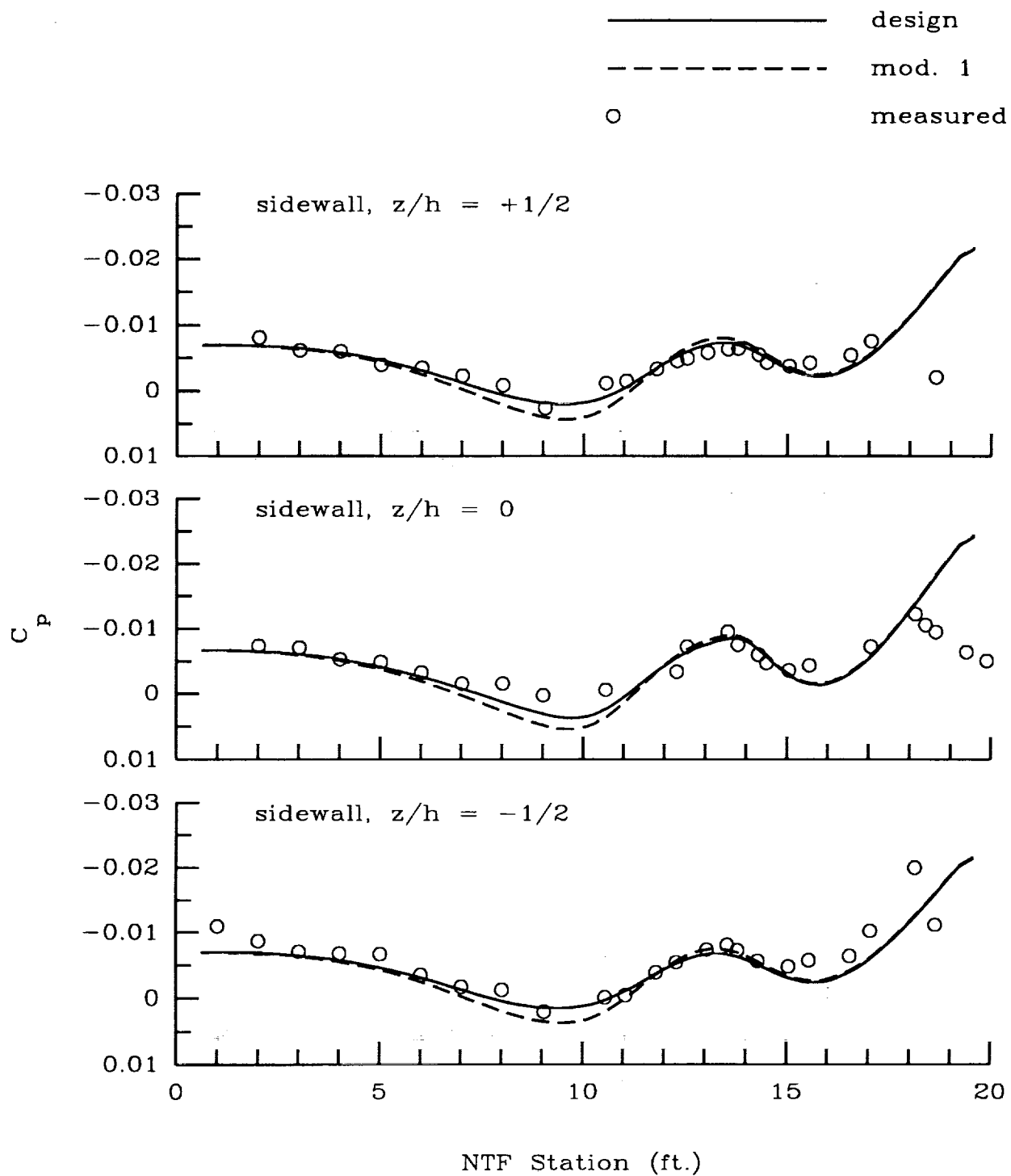
Figure 24. Effect of slot modification 1 on wall pressure coefficients with Boeing 767 at  $M = 0.80$  and  $\alpha = -2.40^\circ$ .

—————	design
- - - - -	mod. 1
○	measured



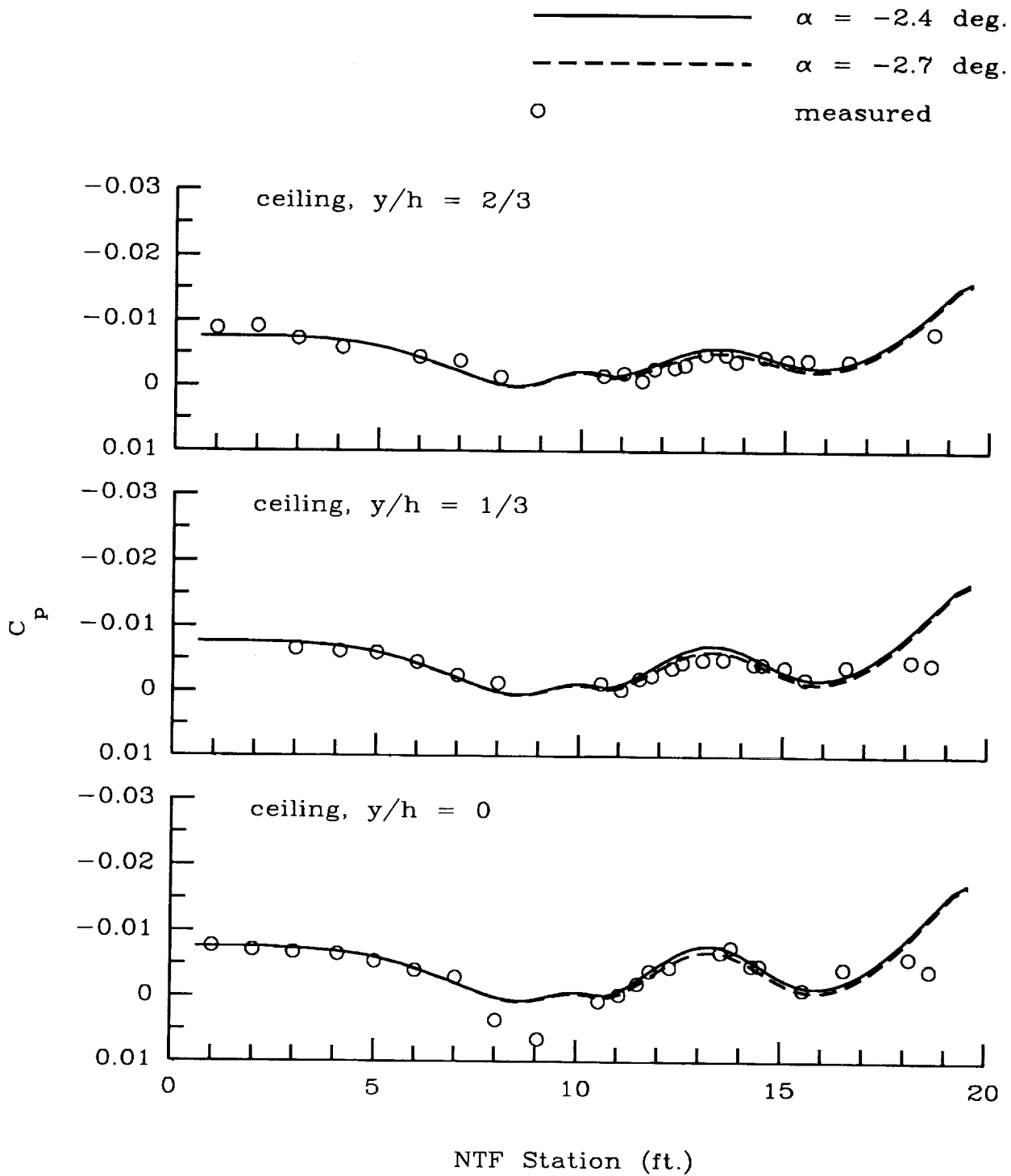
(b) Floor orifice rows.

Figure 24. Continued.



(c) Sidewall orifice rows.

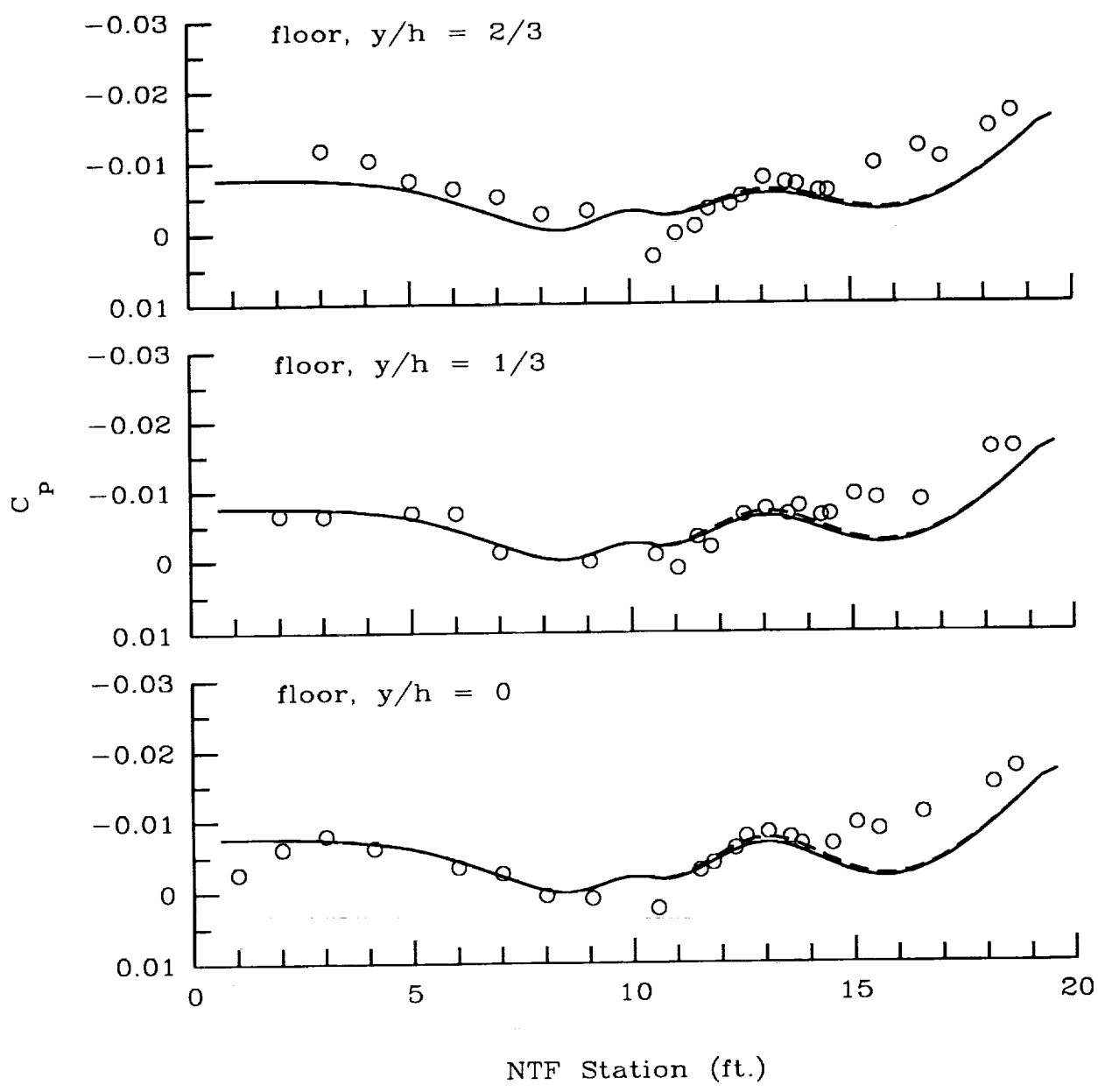
Figure 24. Concluded.



(a) Ceiling orifice rows.

Figure 25. Effect of varying angle of attack near zero lift on wall pressure coefficients for Boeing 767 at  $M = 0.80$ .

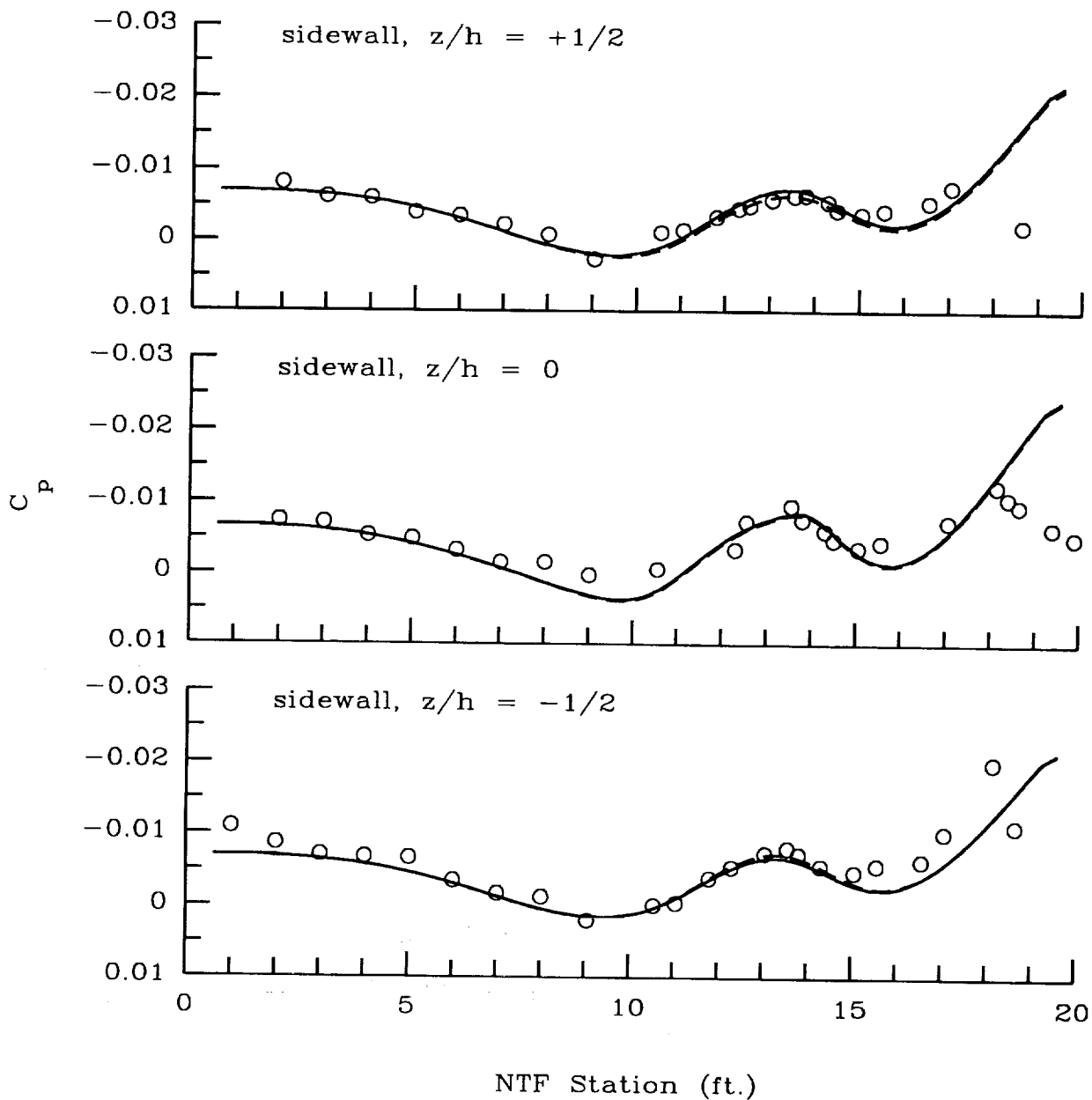
\_\_\_\_\_  $\alpha = -2.4$  deg.  
 - - - - -  $\alpha = -2.7$  deg.  
 ○ measured



(b) Floor orifice rows.

Figure 25. Continued.

—————  $\alpha = -2.4$  deg.  
 - - - - -  $\alpha = -2.7$  deg.  
 ○ measured



(c) Sidewall orifice rows.

Figure 25. Concluded.

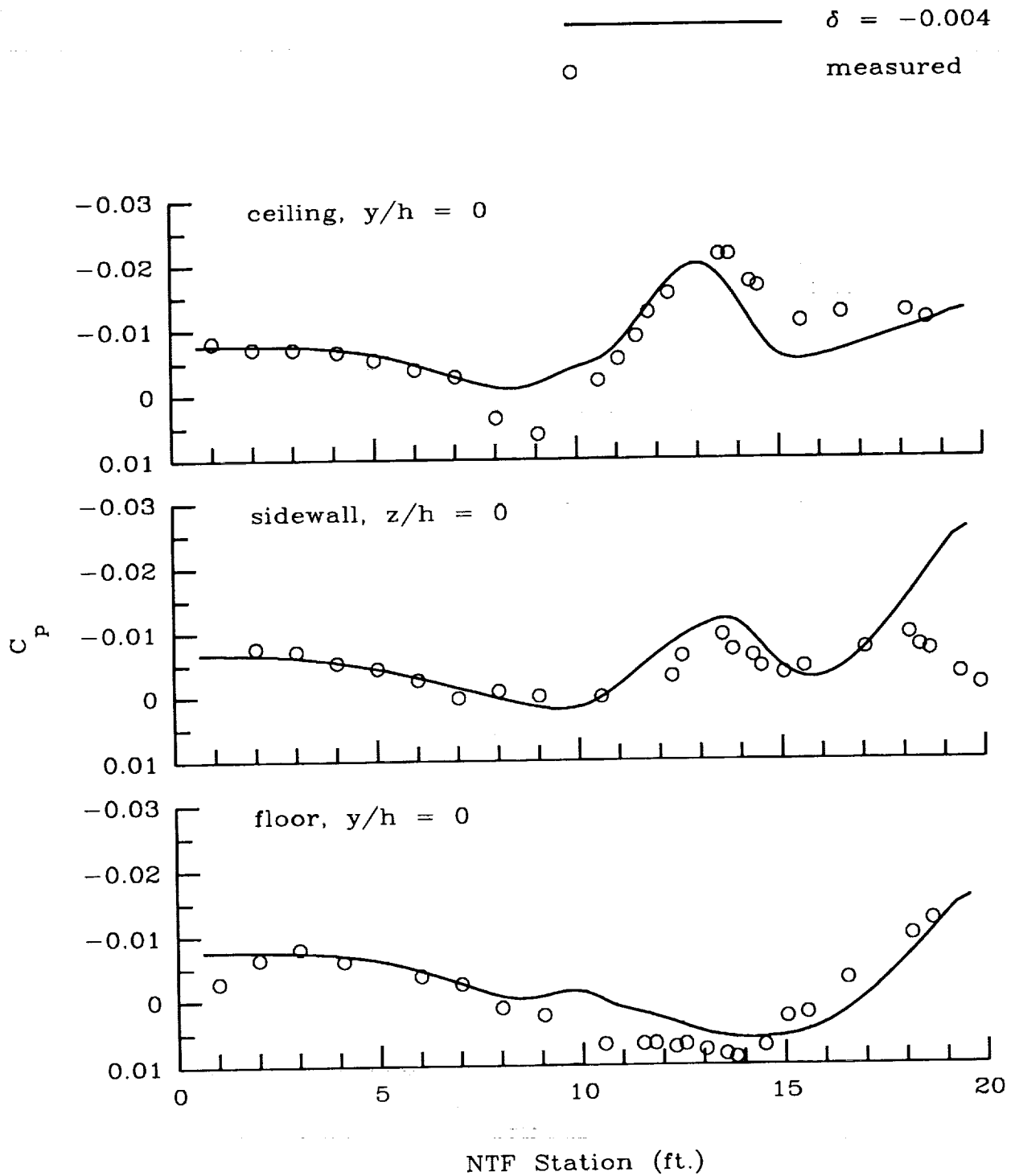
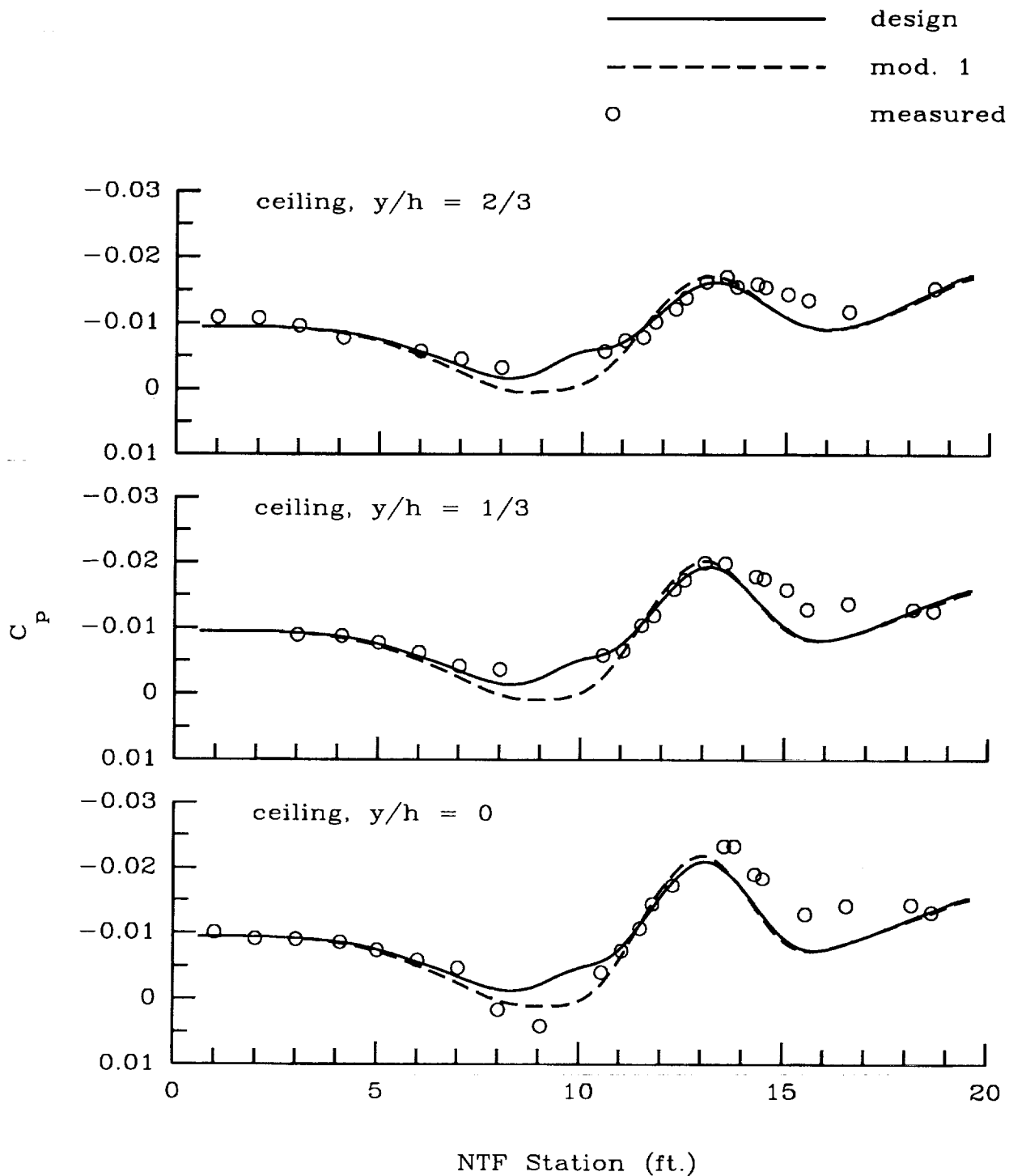


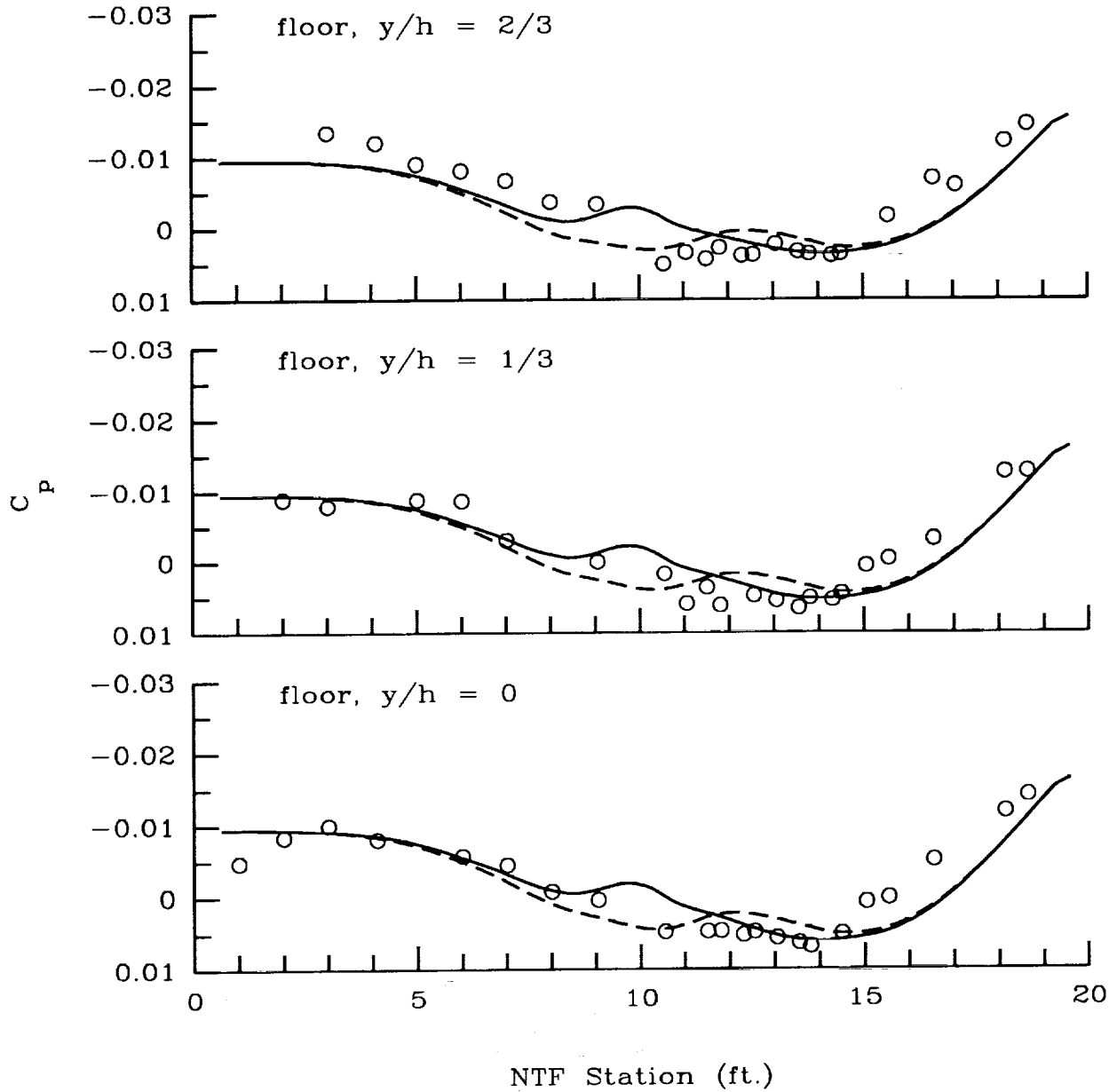
Figure 26. Wall centerline pressure coefficients with Boeing 767 at  $M = 0.80$ ,  $\alpha = 2.15^\circ$ , and  $\delta = -0.004$ .



(a) Ceiling orifice rows.

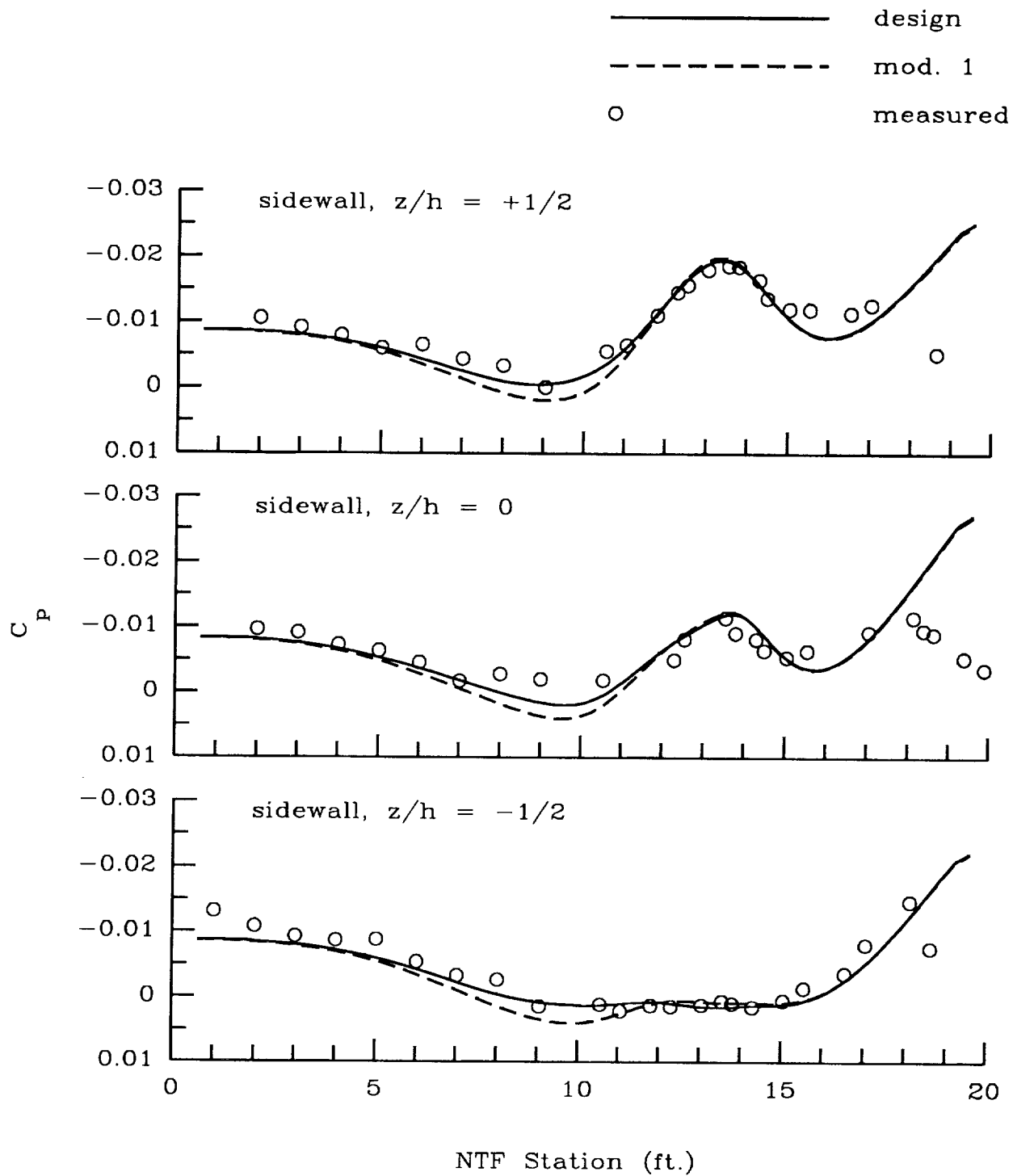
Figure 27. Effect of slot modification 1 on wall pressure coefficients with Boeing 767 at  $M = 0.80$ ,  $\alpha = 2.15^\circ$ , and  $\delta = -0.005$ .

—————	design
- - - - -	mod. 1
○	measured



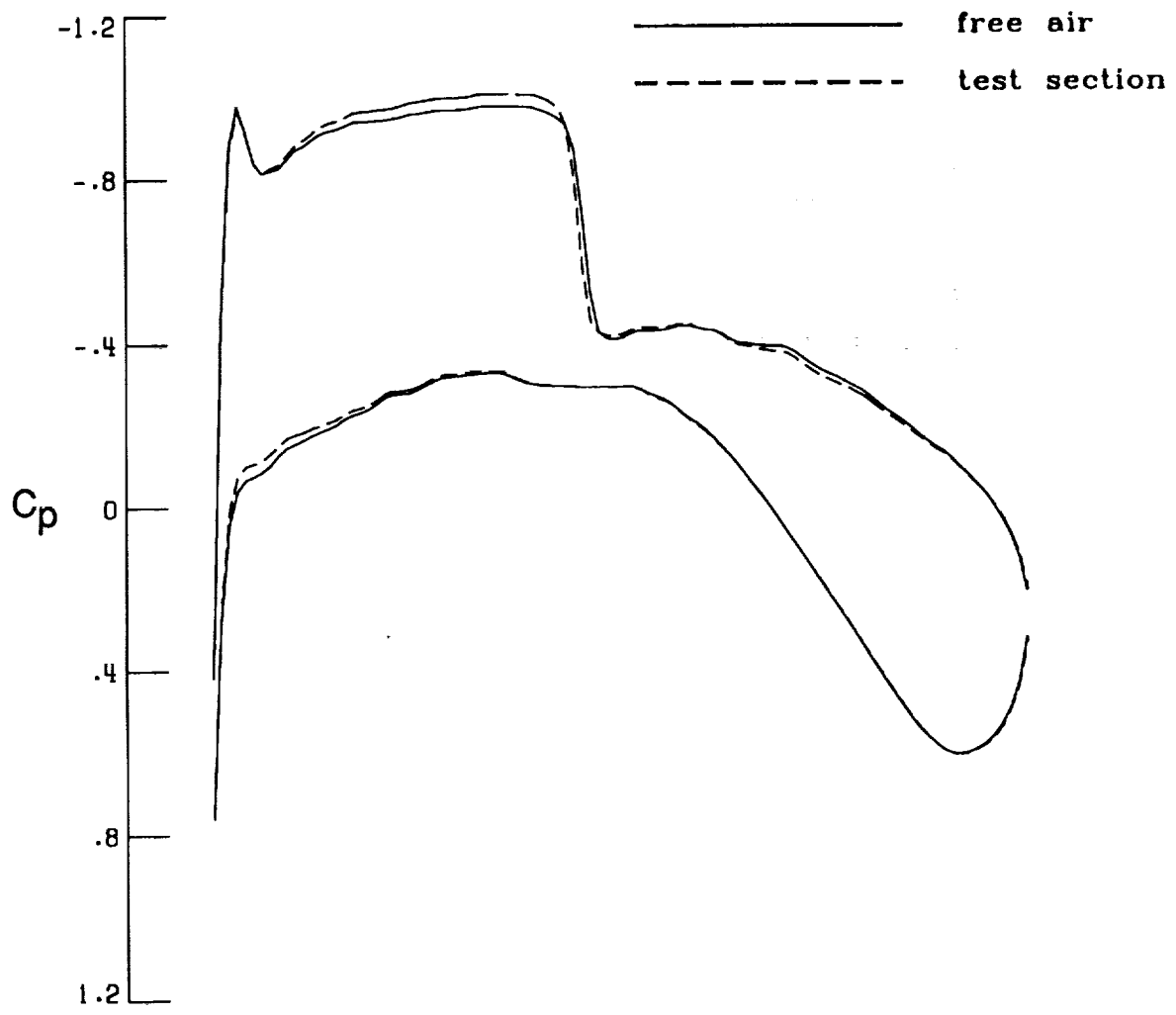
(b) Floor orifice rows.

Figure 27. Continued.



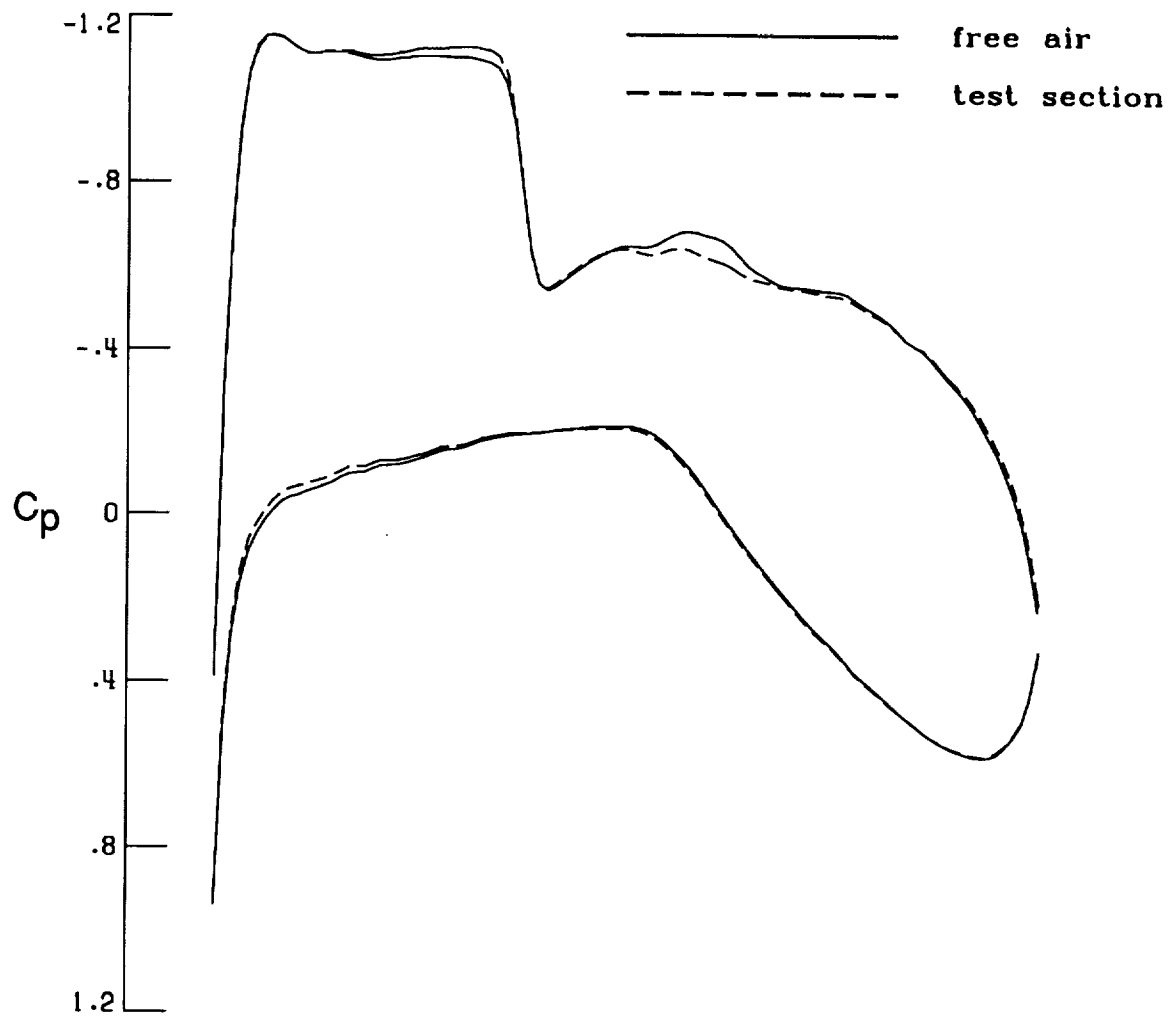
(c) Sidewall orifice rows.

Figure 27. Concluded.



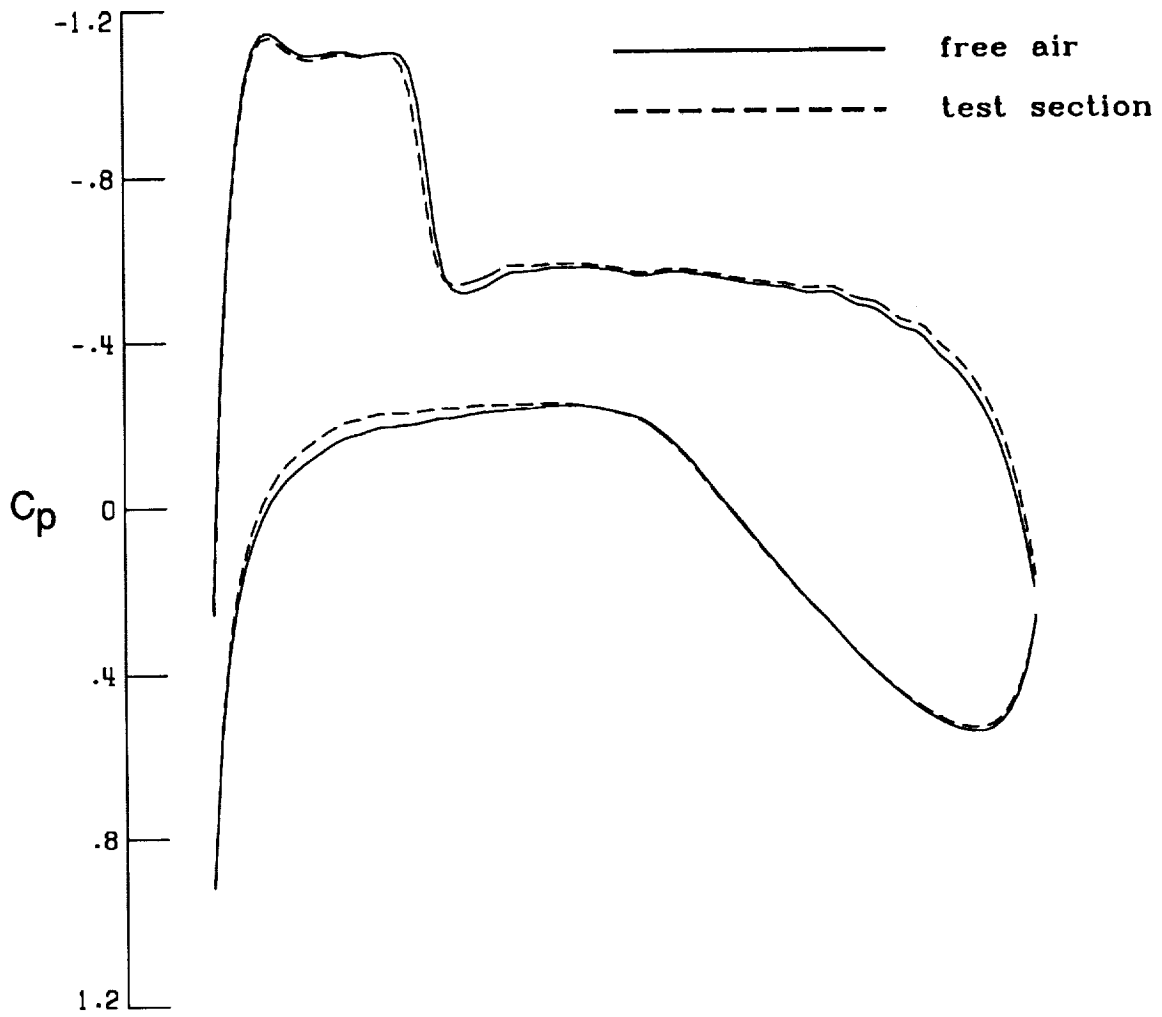
(a) 21-percent semispan.

Figure 28. Calculated wing pressure coefficients for free-air and wind tunnel (with discrete slotted floor and ceiling) calculations. Pathfinder I at  $M = 0.80$  and  $\alpha = 2.70^\circ$ .



(b) 52-percent semispan.

Figure 28. Continued.



(c) 82-percent semispan.

Figure 28. Concluded.

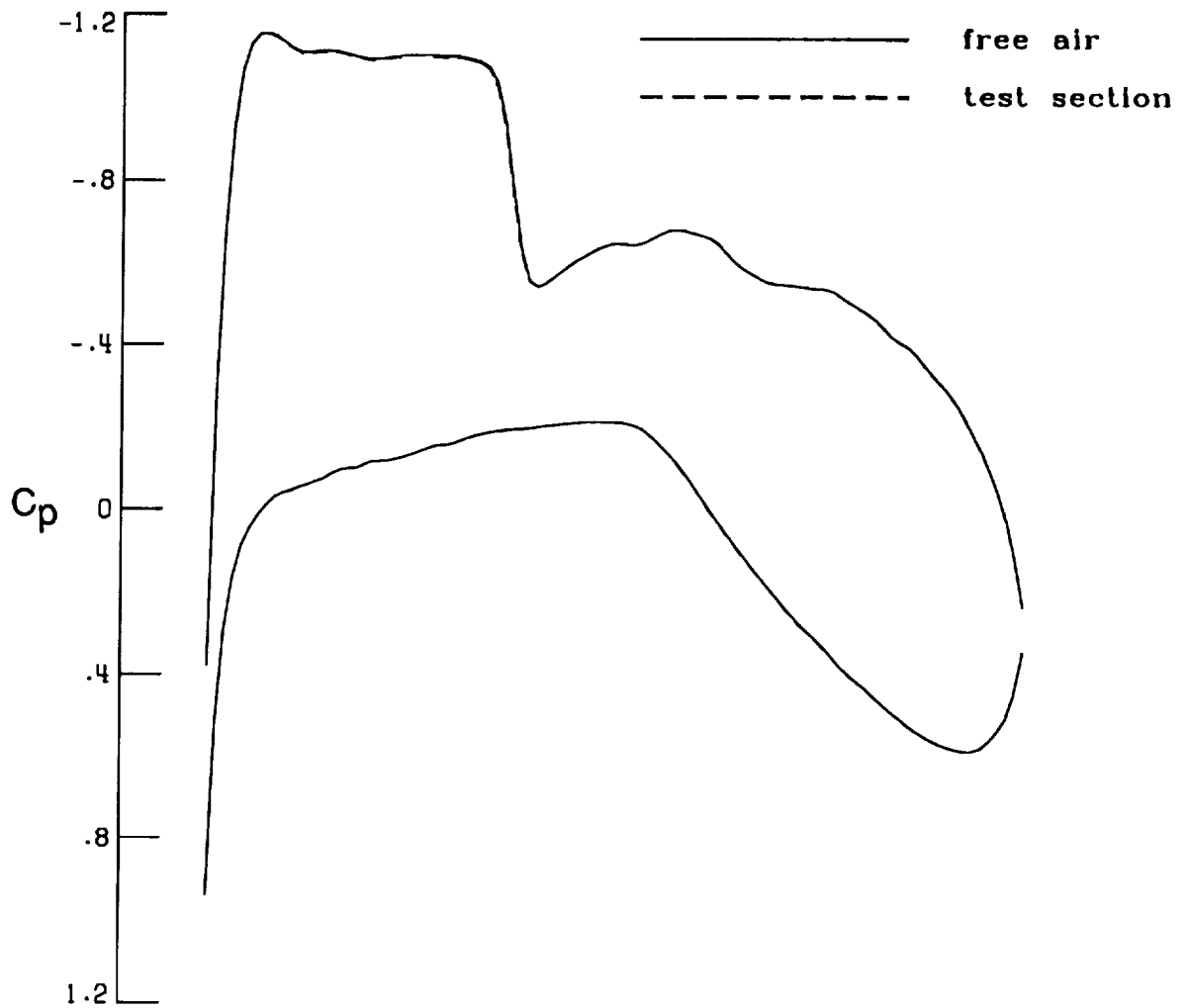


Figure 29. Calculated wing pressure coefficients for free-air and wind tunnel (with homogeneous slotted floor and ceiling) calculations. Pathfinder I at  $M = 0.80$  and  $\alpha = 2.70^\circ$ ; 52-percent semispan.

REPORT DOCUMENTATION PAGE			Form Approved OMB No. 0704-0188	
Public reporting burden for this collection of information is estimated to average 1 hour per response, including the time for reviewing instructions, searching existing data sources, gathering and maintaining the data needed, and completing and reviewing the collection of information. Send comments regarding this burden estimate or any other aspect of this collection of information, including suggestions for reducing this burden, to Washington Headquarters Services, Directorate for Information Operations and Reports, 1215 Jefferson Davis Highway, Suite 1204, Arlington, VA 22202-4302, and to the Office of Management and Budget, Paperwork Reduction Project (0704-0188), Washington, DC 20503.				
1. AGENCY USE ONLY (Leave blank)	2. REPORT DATE September 1993	3. REPORT TYPE AND DATES COVERED Technical Paper		
4. TITLE AND SUBTITLE Wall Interference and Boundary Simulation in a Transonic Wind Tunnel With a Discretely Slotted Test Section		5. FUNDING NUMBERS WU 505-59-54-01		
6. AUTHOR(S) Jassim A. Al-Saadi				
7. PERFORMING ORGANIZATION NAME(S) AND ADDRESS(ES) NASA Langley Research Center Hampton, VA 23681-0001		8. PERFORMING ORGANIZATION REPORT NUMBER L-16973		
9. SPONSORING/MONITORING AGENCY NAME(S) AND ADDRESS(ES) National Aeronautics and Space Administration Washington, DC 20546-0001		10. SPONSORING/MONITORING AGENCY REPORT NUMBER NASA TP-3334		
11. SUPPLEMENTARY NOTES				
12a. DISTRIBUTION/AVAILABILITY STATEMENT  Unclassified-Unlimited  Subject Category 09		12b. DISTRIBUTION CODE		
13. ABSTRACT (Maximum 200 words) A computational simulation of a transonic wind tunnel test section with longitudinally slotted walls is developed and described herein. The nonlinear slot model includes dynamic pressure effects and a plenum pressure constraint, and each slot is treated individually. The solution is performed using a finite-difference method that solves an extended transonic small disturbance equation. The walls serve as the outer boundary conditions in the relaxation technique, and an interaction procedure is used at the slotted walls. Measured boundary pressures are not required to establish the wall conditions but are currently used to assess the accuracy of the simulation. This method can also calculate a free-air solution as well as solutions that employ the classical homogeneous wall conditions. The simulation is used to examine two commercial transport aircraft models at a supercritical Mach number for zero-lift and cruise conditions. Good agreement between measured and calculated wall pressures is obtained for the model geometries and flow conditions examined herein. Some localized disagreement is noted, which is attributed to improper simulation of viscous effects in the slots.				
14. SUBJECT TERMS Slotted walls; Wall interference; Wind tunnel corrections; Transonic wind tunnels		15. NUMBER OF PAGES 74		16. PRICE CODE A04
17. SECURITY CLASSIFICATION OF REPORT Unclassified	18. SECURITY CLASSIFICATION OF THIS PAGE Unclassified	19. SECURITY CLASSIFICATION OF ABSTRACT	20. LIMITATION OF ABSTRACT	